

UVM ScholarWorks

Enhancing grid reliability with coordination and control of distributed energy resources

Item Type	dissertation;article
Authors	Mavalizadeh, Hani
Download date	2026-06-12 08:09:24
Link to Item	https://hdl.handle.net/20.500.14849/3765

ENHANCING GRID RELIABILITY WITH COORDINATION AND CONTROL OF DISTRIBUTED ENERGY RESOURCES

A Dissertation Presented

by

Hani Mavalizadeh

to

The Faculty of the Graduate College

of

The University of Vermont

In Partial Fulfillment of the Requirements
for the Degree of Doctor of Philosophy
Specializing in Electrical Engineering

January, 2024

Defense Date: November 10th, 2023
Dissertation Examination Committee:

Mads Almassalkhi, Ph.D., Advisor

Safwan Wshah, Ph.D., Chairperson

Luis Duffaut Espinosa, Ph.D.

Samuel Chevalier, Ph.D.

Amritanshu Pandey, Ph.D.

Holger Hooek, DPhil, Dean of the Graduate College

ABSTRACT

The growing utilization of renewable energy resources (RES) within power systems has brought about new challenges due to the inherent uncertainty associated with RES, which makes it challenging to accurately forecast available generation. Furthermore, the replacement of synchronous machines with inverter-based RES results in a reduction of power system inertia, complicating the task of maintaining a balance between generation and consumption. In this dissertation, coordinating Distributed Energy Resources (DER) is presented as a viable solution to these challenges.

DERs have the potential to offer different ancillary services such as fast frequency response (FFR) when efficiently coordinated. However, the practical implementation of such services demands both effective local sensing and control at the device level and the ability to precisely estimate and predict the availability of synthetic damping from a fleet in real time. Additionally, the inherent trade-off between a fleet being available for fast frequency response while providing other ancillary services needs to be characterized. This dissertation introduces a fully decentralized, packet-based controller for a diverse range of flexible loads. This controller dynamically prioritizes and interrupts DERs to generate synthetic damping suitable for primary frequency control. Moreover, the packet-based control methodology is demonstrated to accurately assess the real-time availability of synthetic damping. Furthermore, spectral analysis of historical frequency regulation data is employed to establish a probabilistic bound on the expected synthetic damping available for primary frequency control from a fleet and the trade-off of concurrently offering secondary frequency control.

It is noteworthy that coordinating a large number of DERs can potentially result in grid constraint violations. To tackle this challenge, this dissertation employs convex inner approximations (CIA) of the AC power flow to address the optimization problem of quantifying the capacity of a three-phase distribution feeder to accommodate DERs. This capacity is often referred to as hosting capacity (HC). However, in this work, we consider separate limits for positive and negative DER injections at each node, ensuring that injections within these nodal limits adhere to feeder voltage and current constraints. The methodology dissects a three-phase feeder into individual phases and applies CIA-based techniques to each phase. Additionally, new approaches are introduced to modify the per-phase optimization problems to mitigate the inherent conservativeness associated with CIA methods and enhance HC. This includes selectively adjusting the per-phase impedances and proposing an iterative relaxation method for per-phase voltage bounds.

To my mother,
and to the memory of my father
with love

ACKNOWLEDGEMENTS

I wish to express my profound gratitude to my advisor, Prof. Mads Ronne Almasalkhi, for his unwavering support and invaluable guidance throughout my Ph.D. journey. Working under his mentorship has been a truly enriching experience, providing both research insights and project management skills. His constructive feedback has significantly elevated my presentation and communication abilities, preparing me for a promising career in research and development. I am sincerely appreciative of the privilege to learn and grow under his expert guidance.

During my doctoral journey, I also had the honor of collaborating with Prof. Luis Duffaut Espinosa. His deep expertise in the field proved to be invaluable, and his insights played a crucial role in the development of our work.

I would like to extend my gratitude to Prof. Safwan Wshah, Paul Hines, Amritanshu Pandey, and Samuel Chevalier for being part of my dissertation examination committee.

My heartfelt thanks are extended to my colleagues and cherished friends at UVM, including Adil, Nawaf, Ivan, Danial, Mazen, Waheed, Mahraz, Sarnaduti, and Mustafa, for their camaraderie and unwavering support.

Finally, I am deeply indebted to my mother, Mahin Mola, for her unending love and support throughout my academic journey. My gratitude to her knows no bounds, and I will forever cherish her contributions to my success.

TABLE OF CONTENTS

Dedication	ii
Acknowledgements	iii
List of Abbreviations	vi
List of Figures	viii
List of Tables	ix
1 Introduction	1
1.1 Motivation	1
1.2 Literature review	3
1.2.1 DER coordination	3
1.2.2 Virtual battery models	5
1.2.3 Frequency control using DER coordination	7
1.2.4 Grid aware hosting capacity	10
2 Preliminaries	13
2.1 Dynamic swing equations	13
2.2 Power flow equations	15
2.3 Unbalanced distribution power flow	17
2.4 DER coordination	19
2.4.1 Optimization-based DER coordination	19
2.4.2 Packet-based DER coordination	20
2.4.3 Fitness-based method	25
2.5 DER hosting capacity for balanced grids	27
2.5.1 Convex Inner Approximation	28
2.6 Virtual battery model	31
3 DER coordination to provide fast frequency response	37
3.1 Decentralized Frequency Control using Packet-based Energy Coordination	38
3.2 Predicting the aggregate response	45
3.2.1 Timer-based prioritization	45
3.3 Numerical validation with Two-area system	48
3.3.1 Equivalent damping of PEM loads	48
3.4 Extending the method to arbitrary reference signals	51
3.4.1 Modifying the proposed control law	53
3.4.2 Real-time estimation of damping	55
3.5 Characterizing the available synthetic damping	60
3.5.1 Spectral decomposition of AGC data	62

3.5.2	Finding probabilistic lower bound on available damping	66
3.5.3	FFR versus frequency regulation trade-off	74
3.5.4	Tuning of the controller parameters	77
3.6	Practical considerations	78
3.6.1	Actuation delay	80
3.6.2	Frequency measurement resolution	81
3.6.3	Relating the scale of aggregate DER response	82
3.7	conclusion	82
4	Methodology to compare DER coordination schemes	85
4.1	Fitness-based coordination and estimation	87
4.2	Methodology for comparing DER schemes	90
4.3	Simulation results	91
4.3.1	Determining representative 1-hour AGC samples	92
4.3.2	Multi Criteria decision making	92
4.3.3	Simulation case study	94
4.4	Conclusion	98
5	Hosting Capacity in Distribution Systems	100
5.1	Extending CIA to unbalanced feeders	102
5.2	Modifying $\mathbf{P}_{\text{CIA}}^{\phi,-/+}$ for three-phase grid	106
5.2.1	Iterative Mod-Z	116
5.2.2	Mod-Z for unbalanced grids	117
5.3	Iterative voltage bounds to increase HC	122
5.4	Random search method	125
5.5	Numerical results	125
5.6	Conclusion	131
	References	132
	Appendix	141
A.	Derivation of current proxy bounds l^- and l^+	141

LIST OF ABBREVIATIONS

AGC	Automatic generation control
CDF	Cumulative distribution function
CIA	Convex inner approximation
CQoS	Customer quality of service
CPS	Cyber-physical system
DER	Distributed energy resource
DQoS	Device quality of service
EKF	Extended Kalman filter
ESS	Energy storage system
EV	Electric vehicle
EWH	Electric water heater
FFR	Fast frequency response
HC	Hosting capacity
IEEE	Institute of electrical and electronic engineers
ISO	Independent system operator
LMP	Locational marginal price
MAE	Mean absolute error
MTTR	Mean time to request
PEM	Packetized energy management
QoS	Quality of service
RES	Renewable energy resources
RMSE	Root mean squared error
RoCoF	Rate of change of frequency
SoC	State of Charge
TCL	Thermostatically controlled load
VB	Virtual battery
VUF	Voltage unbalance factor

LIST OF FIGURES

3.1	The state of local timers and temperature of ON devices before the disturbance.	40
3.2	Illustrating the proportion of interrupted devices based on any locally measured frequency deviation from nominal, $\Delta f[k] := f[k] - f_0$	42
3.3	Aggregate power, frequency, and average temperature for different values of η_{max} for 400,000 DERs. A 500 MW drop in total generation occurs at $t = 5$ seconds.	44
3.4	Block diagram of primary frequency control of a two-area power system	49
3.5	Estimation of frequency response for different values of η_{max}	52
3.6	Block diagram of the proposed derivative-proportional control law. $g_1(\cdot)$ and $g_2(\cdot)$ are defined in (3.8)	53
3.7	Frequency response of 200,000 TCLs for different values of K_D	57
3.8	(<i>Top</i>) A single frequency event with $\Delta f_{nadir} = 0.07\text{Hz}$ yields a large load reduction in the aggregate DER fleet as a function of the frequency deviation, packet timer distribution, and designed control law. (<i>Bottom</i>) Comparing the actual damping with the real-time estimate of synthetic damping for 10 different frequency events.	58
3.9	Illustrative example for computation of P_{min}	67
3.10	Probability of violating the bounds	71
3.11	The actual vs estimate damping lower bound for 200,000 TCLs	72
3.12	The actual vs estimate damping lower bound for 200,000 batteries	73
3.13	The impact of ancillary service prices on the total normalized revenue, $O[MW/Hz]$. The red line indicates β^{thr} above which larger AGC magnitudes, increase revenue.	76
3.14	Unused timer and minimum damping for different values of K_D	79
3.15	The frequency response for different actuation delays for a population of 200,000 DERs. The disturbance occurs at $t=2$ s.	80
3.16	The frequency response for different frequency measurement resolutions for a population of 200,000 TCLs.	81
3.17	Frequency response, with/without droop control at bus 39 and with/without DER coordination.	83
4.1	Feedback control system for different coordination schemes.	89
4.2	Comparing the mean performance of coordination schemes.	98
4.3	Comparing the worst performance of coordination schemes.	99

5.1	Illustrating the effects of Method 2ii on three-phase voltage and current profiles following the addition of nodal injections $p_a^+ + p_b^+ + p_c^+$. The dashed red line indicates the ANSI voltage limits of $[0.95, 1.05]$ pu.	104
5.2	Comparison of N_v between different methods across 100 scenarios.	107
5.3	Comparison of M_v (pu) between different methods across 100 scenarios.	107
5.4	Comparison of S_v (pu) between different methods across 100 scenarios.	108
5.5	Comparison of W_M (pu) between different methods across 100 scenarios.	108
5.6	Comparison of $VUF(\%)$ between different methods across 100 scenarios.	110
5.7	Comparison between three-phase and single-phase voltages for the modified IEEE 37-node system. The dashed red lines indicate the voltage limits.	112
5.8	Three-phase voltages after modifying the impedance matrix based on Theorem 4 for the IEEE 37-node system. The dashed red lines indicate the voltage limits.	113
5.9	Comparison between three-phase and single-phase voltages for the modified 534-node feeder. The dashed red lines indicate the voltage limits.	114
5.10	Three-phase voltages after modifying the impedance matrix based on Theorem 4 for the 534-node feeder. The dashed red lines indicate the voltage limits.	115
5.11	ZUF (%) versus α for different scenarios in the IEEE 37 bus system.	119
5.12	HC versus α in the IEEE 37 bus system. Blue, red and yellow curves show the HC for phases a, b, and c, respectively.	120
5.13	ϵ versus α in the IEEE 37 bus system.	121
5.14	M_v versus ZUF in the IEEE 37 bus system.	121
5.15	N_v versus ZUF in the IEEE 37 bus system.	122
5.16	Flowchart of the proposed iterative voltage bound approach.	123
5.17	Voltage bounds upon termination of the iterative method.	127
5.18	Comparing the hosting capacity from the iterative approach to that of Method 2ii and Mod-Z.	128
5.19	Voltage profiles for a 534-node feeder are depicted in the figures below for $\mathbf{P}_{CIA}^{\phi,-}$. In these figures, blue, red, and yellow correspond to phases a, b, and c, respectively.	129
5.20	Voltage profiles for a 534-node feeder are depicted in the figures below for $\mathbf{P}_{CIA}^{\phi,+}$. In these figures, blue, red, and yellow correspond to phases a, b, and c, respectively.	130

LIST OF TABLES

3.1	Characteristics of frequency response for different η_{max}	43
3.2	Simulation Parameters	50
3.3	Accuracy of online estimation of Damping	51
3.4	Simulation Parameters	79
4.1	Comparing the performance of DER coordination schemes in terms of average and worst values of $X_{j,i}$ across $i = 1, \dots, N_s$	97
5.1	Performance of the proposed methods for Three Scenarios	109
5.2	The impact of modifying the impedance matrix on HC and voltage violations for the modified IEEE 37-node system.	116
5.3	Comparing the different methods across two networks.	128

CHAPTER 1

INTRODUCTION

1.1 MOTIVATION

To keep the stability of a power system, the generation and consumption in the power system must be kept close to each other in real time. The penetration of inverter-based renewable energy resources (RES) such as wind and rooftop solar is increasing rapidly due to environmental concerns. The increased use of RES has made keeping the balance between generation and consumption more difficult. This is due to the inherent uncertainty associated with RES, making it difficult to predict the amount of available generation in real-time. To address this issue, in this work the coordination of distributed energy resources (DERs) such as electric water heaters (EWHs) or batteries is proposed.

The ability of a fleet of DERs to provide ancillary services, depends on the average fleet's energy level. While the state of charge (SoC) of individual DERs (e.g., EWHs's water temperature) can be easily measured, determining the SoC of a controlled virtual battery aggregation is a technically challenging task due to the fleet's

heterogeneous nature, characterized by nonlinear, stochastic, differential equations with time-varying parameters. To effectively coordinate and characterize a large and heterogeneous fleet of DERs, a common abstraction is denoted as a virtual battery (VB).

Numerous DER coordination schemes are introduced in technical literature each year. These schemes exhibit variations in terms of controllability, observability, information exchange rate between the coordinator and individual DERs, and the computational burden involved. Consequently, there arises a necessity for a systematic comparison of these methods, considering the conflicting criteria, to evaluate their performance. In light of this, the dissertation proposes a systematic methodology for the evaluation of any DER coordination scheme.

DER coordination schemes have demonstrated their capability to deliver frequency regulation services within power systems. Nevertheless, to offer fast frequency response, DERs must react to frequency disturbances within a timeframe of a few hundred milliseconds. Given this requirement, the dissertation introduces a fully decentralized local controller. This controller relies on frequency deviation and the rate of change of frequency (RoCoF) to determine the frequency response. The decentralized approach is imperative, as real-time communication with a coordinator at a large scale is often impractical.

It is worth noting that even though the designed controller operates in a fully decentralized manner, where all decisions are made at the device level, it remains crucial for the coordinator to have the ability to estimate the response, specifically the synthetic damping, provided by a given fleet. This capability is essential for the coordinator to participate in potential primary frequency control markets effec-

tively. To address this requirement, this work presents a methodology that allows the coordinator to estimate the real-time availability of synthetic damping for a list of credible frequency events within any packet-based coordination scheme. Furthermore, the study utilizes spectral analysis of historical frequency regulation data to establish a probabilistic bound on the expected synthetic damping available for primary frequency control from a fleet, all while considering the trade-off of simultaneously providing secondary frequency control services.

Finally, coordinating a large number of DERs can potentially lead to grid constraint violations. Therefore, it is important to take steps to ensure that the DER coordination schemes used, do not lead to grid constraint violations such as under/over voltage or transformer overload. To do this, in this work an upper and lower bound on the hosting capacity (HC) of each node of a three-phase unbalanced distribution system is obtained using a convex inner approximation (CIA) of power flow equations. Since the CIA is inherently conservative, two methods are presented to adjust the conservativeness of CIA approximation.

1.2 LITERATURE REVIEW

1.2.1 DER COORDINATION

Public opinion and policies concerning efforts to mitigate climate change are driving increased penetration of renewable generation. Integrating renewable energy sources into the electric grid while maintaining reliability is a fundamental power engineering challenge that will require large-scale deployment of grid-side and demand-side

flexibility. New advances in sensor technology together with low-cost edge computing and connectivity enable DER coordinators to regulate DERs remotely to respond to the needs of the grid and leverage market opportunities while satisfying customer usage [1]. This makes demand-side management a viable option for ancillary services, such as frequency regulation [2] or fast frequency response [3]. As a result, much research has been focused on studying the potential uses of DER coordination in modern power system operations in recent years.

For the DER coordination schemes to be valuable for system operations, they should be capable of coordinating thousands of kW-scale, flexible electric loads such as electric vehicles (EVs), batteries, and thermostatically controlled loads (TCLs) [4]. At this scale, the roles of computation, communication, and data management requirements are critical. In addition, most of the DER coordination schemes require that some data is shared between consumers and a coordinator. This raises data privacy [5], as well as, cyber-security concerns [6]. In fact, if consumers are not convinced that their information is safe and secure, the participation rate will drop, rendering the whole scheme unviable [7, 8]. Thus, DER coordination architecture requires careful analysis and design.

DER coordination schemes can generally be categorized into direct/top-down and indirect/bottom-up architectures. In direct control schemes, a central coordinator has full access to and control over all DER information and actuation. While direct control potentially leads to good performance, the large computation and communication burden raises concerns about scalability. In indirect control schemes, the decisions are made at each DER based on local measurements, which reduces communication and computation overhead but raises concerns about tracking performance

Another key factor in DER coordination architectures is the underlying data availability and communication requirements [9]. Indirect schemes can be further classified based on the level of information shared between consumer and coordinator: *i*) mediated coordination: coordinator collects DER information, *ii*) bilateral coordination: DERs communicate with each other, and *iii*) implicit coordination: individual DER information is not shared [9]. While higher levels of information sharing improve the performance of the coordination scheme, it can lead to privacy and security issues.

With the requirements of data management and concerns over data privacy in DER coordination schemes, the conceptual idea of virtual batteries has been introduced in the literature to simplify predicting the aggregate behavior of a fleet of DERs. Next subsection provides a brief description of virtual battery.

1.2.2 VIRTUAL BATTERY MODELS

With the increasing integration of DERs into energy systems, examining the DER fleet’s capacity to track a reference signal, is becoming crucial. This capacity is depends on the state of charge or SoC of the aggregated DERs. When contextualized within this framework, the aggregation of DERs may be conceptualized as a “virtual battery.”

Resources such as TCLs also represent a source of stored (thermal) energy that is flexible (i.e., it can defer energy consumption/supply without impacting the quality of service (QoS) for end-users). [10] proposes a method to quantify the aggregate flexibility for a fleet of TCLs. When aggregated and coordinated, thousands of TCLs can function as a single battery-like resource or grid asset, known as a virtual battery (VB) model [11]. Such a VB model can be a useful abstraction of a (large) collection

of DERs for the purpose of effectively dispatching DERs *en masse*. A VB model typically includes a scalar state-of-charge (SoC) measured in megawatt-hours (MWh), as well as upper and lower power bounds measured in megawatts (MW) and energy capacity bounds measured in MWh. The SoC represents the average DER energy level of the DER fleet, the power bounds inform the maximum and minimum deviation in power consumption (from some established baseline or an admissible operating range) that can be consumed or provided by the devices, while the capacity bounds provide limits for the SoC. To effectively design coordination and control schemes using the VB model, it is necessary that the VB parameters are accurately estimated or identified.

Different studies have explored the identification of VB models for DERs. For example, in [12], the charge rate limits and capacity parameters are identified for a collection of TCLs, whereas in [11], a detailed model of the load and its control system is used to generate a VB model for a residential heating, ventilation, and air conditioning (HVAC) system. The role of ambient conditions on the aggregate response of TCLs is studied in [13]. Further research has formulated explicit virtual battery models for TCLs, coupling power response with the fleet’s SoC [14] in a low-order, dynamic model. In [15], the VB parameters such as self-dissipation rate, and energy capacity are obtained via simulation using a first-order VB model by repeatedly solving an optimal control problem that minimizes the power tracking error for the aggregate. However, a challenge with these methods is that they assume the availability of full end-use device-specific parameters, which are often unknown in practice.

An alternative to model-based approaches for VB model identification, e.g., [16],

is data-driven methods using, for example, machine learning or, specifically, deep learning [17]. Deep learning involves training a neural network using operational data from DERs to obtain the VB model. Recent works have explored identifying VB parameters using deep learning. For example, in [18], a transfer learning-based stacked autoencoder is used to calculate the virtual battery state of a given ensemble of flexible TCLs from available end-use measurements. In [19], a variational autoencoder-based deep learning algorithm is proposed to identify the probability distribution of the parameters of a stochastic VB model, such as self-dissipation rate, and power and energy capacities. The limitation with these works is that they assume that the coordinator has direct controllability and full observability of all devices' state information, which is not practical in real-time implementations. Therefore, the aforementioned identification methods are difficult to adapt to practice without incurring high communication overhead, as they need real-time data streaming from all devices to the coordinator. In the next subsection, the coordination of a DER fleet, i.e., virtual battery, to provide frequency control is explained.

1.2.3 FREQUENCY CONTROL USING DER COORDINATION

The penetration of RES is increasing rapidly as a part of the global effort to reduce greenhouse gas emissions. However, increased RES use leads to more variability in electricity generation due to RES' intrinsic uncertainty. In addition, replacing conventional synchronous generators with inverter-based renewable generation reduces the inertia, i.e., the power system's ability to oppose changes in frequency [20].

A significant deviation from nominal frequency can lead to an outage of generation units which subsequently causes further frequency deviation and, in severe cases, can result in a total system blackout. A recent example was the Texas blackout in 2021, which led to approximately 155 billion dollars in loss [21]. Therefore corrective actions are crucial, to control the power system frequency. Frequency control mechanisms include primary, secondary, and tertiary frequency control. Primary frequency control also called fast frequency response is largely automatic and instantaneous and occurs over the first few seconds following a grid disturbance event. The secondary frequency control brings the frequency back to the nominal value by adjusting the output of generating units within a few minutes after a frequency event. Tertiary frequency control restores the power reserve of the generators used for the secondary frequency control [22]. In this paper, the focus is on primary control since secondary and tertiary control do not significantly influence the transient frequency dynamics.

DERs are widely considered an effective and scalable way to provide primary frequency control [23,24]. DER coordination can be used to provide synthetic damping, which is defined as the percentage change in the total DER consumption in response to frequency change [20], as well as inertia, improving the stability of the power system. Coordinating DERs to provide primary frequency control has been studied for many years [25–28]. One of the first works on frequency responsive loads was presented in 1980 called frequency adaptive power and energy re-scheduler (FAPER) [25]. In this method, the dynamic state of TCLs is used to prioritize them for frequency response. For example, devices with high temperatures will be prioritized to be turned off during an under-frequency event. In addition, the bounds on temperature are frequency-dependent meaning that for higher frequency deviations, more devices par-

ticipate in the frequency response. Probabilistic FAPER was introduced in [26] by injecting random delays in devices switching on/off, which helped address synchronization concerns with FAPER, i.e., avoided large groups of DERs attaining nearly the same temperature and, thus, responding nearly identically and causing large power swings.

Different types of DERs can be coordinated for primary frequency control. TCLs (e.g., EWHs and refrigerators) can be turned off for short periods without a considerable effect on the temperature, which provides some flexibility used for a rapid change in load. Also, TCLs form a large portion of the power system load [27], and therefore, coordinating them provides considerable capacity for the power system operator. Another significant advantage of using TCLs is that they are highly responsive, making them an appropriate option for primary frequency control where fast response is required. In [29], smart EWHs are used to compensate for the uncertainty in wind and solar energy, peak shifting, and frequency response. A dynamic model is presented in [28] for different types of TCLs that adapt and improve a direct load control (DLC) scheme for primary frequency regulation in hybrid isolated microgrids. Frequent on/off switching of TCLs increases wear-and-tear and should be minimized during TCL coordination schemes as discussed in [30].

Different control architectures have been proposed for DER coordination, which differs in the level of communication requirements, quality of service (QoS), number of cycling, and level of grid awareness. In [31], a novel method is proposed that relies on transient phase offset to achieve a fast response to primary frequency control. The method enables the power system operators to use resources closer to the frequency deviation source. Such a technique also ensures that the stability of the sys-

tem is preserved. In [32], a fully decentralized leaky integral controller for frequency restoration is presented. The use of decentralized control led to the elimination of communication delays and failures (e.g., lost messages) associated with centralized control schemes. Instead, [32] uses communication between local loads, which decreases the communication structure costs significantly. Other methodologies employ adaptive controllers that adapt to online measurements. One example of such techniques was introduced in [33], where an adaptive control framework is built based on the time-space distribution characteristics of the frequency in the power system. Also, the frequency response control is transformed from decentralized feedback control to centralized feed-forward control. Moreover, adaptive controllers have been shown to reduce problems with actuation delay. Finally, hierarchical optimization-based DER coordination schemes were developed in [34] with the advantage that AC network constraints can be considered. This is the so-called *grid-aware coordination* which will be discussed in the next subsection.

1.2.4 GRID AWARE HOSTING CAPACITY

As the deployment of DERs in power grids continues to accelerate, their utilization in a number of ancillary services is increasing [35]. In this context, DERs can be managed by aggregators, which dispatch them in response to market signals, often without taking into account the limitations of the grid. This lack of consideration can potentially lead to violations of critical grid constraints, including voltage and transformer limits. Therefore, there is an urgent need for what is referred to as *Grid-aware DER coordination*, which involves effectively accounting for AC network constraints during the coordination of DERs [34].

Various methods have been proposed in the technical literature for grid-aware DER coordination. One common approach is to restrict the amount of power that each customer can export to the grid [36]. However, this method can be overly conservative, and with the rapid increase in the number of DERs connected to the grid, these fixed limits can become outdated and require frequent updates [37].

In direct control schemes, it is assumed that the grid operator has access to all DER data and can directly control DERs [38, 39]. While direct control methods can theoretically provide optimal solutions, they often rely on strong assumptions related to observability and controllability. In practice, DER aggregators do not have access to grid data, and grid operators do not have full control over DERs.

Alternatively, [40] proposes an approach where the grid operator adjusts locational marginal prices (LMPs) based on grid conditions to incentivize the aggregator to adapt the DER aggregate load accordingly. However, this paper assumes a balanced distribution system, which may not hold in real-world applications. In [41], two mechanisms are presented to allow the grid operator to override DER aggregator dispatch decisions to ensure grid constraints are not violated. One limitation is that in certain electric markets, the grid operator may not have the authority to block aggregator control decisions.

Another approach is for the grid operator to establish limits on the amount of injection from each node to preserve grid constraints. This approach requires minimal information exchange between the grid operator and aggregator. In [37], the concept of *operating envelopes* is introduced, where the grid operator uses linear or model-free methods to issue time-varying export/import limits to aggregators. A CIA is presented in [42] for maximizing voltage margins, which is generalized in [43] to com-

pute feeder hosting capacity of balanced or single-phase distribution feeders. In [44], a sequential algorithm is presented that constructs a convex restriction around an initial feasible point, subsequently refining it to obtain an improved feasible solution. This work is extended further in [45], where the approach is enhanced to account for robustness against uncertainty in power injections. In [46], a model-free approach is introduced, leveraging historical meter data and neural networks to eliminate the need for solving the non-convex AC OPF problem in unbalanced distribution feeders. It demands access to substantial volumes of meter data, which may not always be readily available. Additionally, it's important to note that model-free methods can exhibit sensitivity to the quality and distribution of data. In [47] a bottom-up approach is presented where DERs submit power injection requests based on their local controllers to the grid operator. The grid operator can deny injection requests if a three-phase power flow analysis indicates a risk of grid constraint violation. An optimization model for assessing the HC of DERs, taking into consideration the anticipated network conditions during demand response scheduling and adapting to the real-time network state is developed in [48].

CHAPTER 2

PRELIMINARIES

In this section, a concise overview of this dissertation's main concepts and models is provided. It introduces the network model and power flow equations. Then, damping and inertia are defined. This is followed by a description of DERs and their role in providing synthetic damping and inertia. The dynamic model of individual DERs and the corresponding aggregate model, termed the 'Virtual Battery,' are presented then. Various DER coordination schemes are subsequently discussed. Finally, grid-aware DER coordination is described to incorporate network conditions.

2.1 DYNAMIC SWING EQUATIONS

Let $G = (\mathcal{V}, \mathcal{E})$ be a graph representing the topology of a transmission network, where $\mathcal{V} := \{1, \dots, N_n\}$, is the set of N_n nodes and $\mathcal{E} \subseteq \mathcal{V} \times \mathcal{V}$ is the set of branches, such that if i and j are connected, then $(i, j) \in \mathcal{E}$. The frequency dynamics of the network

are governed by the swing equations [49]:

$$\Delta \dot{\theta}_j = \Delta \omega_j, \quad (2.1a)$$

$$M_j \Delta \dot{\omega}_j = \Delta P_j^G - \Delta P_j^L - \Delta P_j^{\text{DER}} - D_j \Delta \omega_j + \sum_{i:(i,j) \in \mathcal{E}}^N \Delta P_{ij}, \quad (2.1b)$$

where θ_j and ω_j are the voltage angle and angular velocity at bus j , respectively, and ΔP_j^G , ΔP_j^L , and ΔP_j^{DER} are deviations generation, uncontrollable load, and controlled DER from nominal at bus j [MW], respectively. P_{ij} denotes the power flow between areas i and j [MW]. M_j and D_j , are inertia [MW. sec²] and damping [MW/Hz], respectively, and are defined as follows:

Definition 1 (Inertia). *Inertia is the power system's ability to oppose sudden changes in system frequency due to its rotational kinetic energy.*

Definition 2 (Damping). *percentage change in the total DER consumption in response to frequency change. It measures the ability of the system to dampen oscillatory energy after a disturbance.*

The j^{th} generator's turbine dynamics is modeled in (2.2),

$$\tau_j \Delta \dot{P}_j^G = -\Delta P_j^G - \frac{\Delta \omega_j}{R_j}, \quad (2.2)$$

where R_j is the generator's governor droop coefficient [Hz/MW] and τ_j is the turbine time constant [sec]. Synchronous generator droop controllers usually have a deadband of 36 mHz [50]. The load flow equations are provided next.

2.2 POWER FLOW EQUATIONS

The AC power flow equations, also known as the load flow equations, are used to find the power flow in the power system. For node i the equations are,

$$P_i = |V_i| \sum_{j=1}^N |V_j| (G_{ij} \cos(\theta_{ij}) + B_{ij} \sin(\theta_{ij})) \quad (2.3)$$

$$Q_i = |V_i| \sum_{j=1}^N |V_j| (G_{ij} \sin(\theta_{ij}) - B_{ij} \cos(\theta_{ij})) \quad (2.4)$$

where:

- P_i and Q_i are the active and reactive power injections at node i , respectively.
- $|V_i|$ is the voltage magnitude at node i .
- θ_{ij} is the voltage angle difference between nodes i and j , i.e., $\theta_{ij} = \theta_i - \theta_j$.
- G_{ij} and B_{ij} are the conductance and susceptance, respectively, of the element connecting nodes i and j . These values come from the admittance matrix of the network, where $Y_{ij} = G_{ij} + jB_{ij}$.
- N is the number of nodes in the system.

Note that (2.3) and (2.4) are nonlinear due to their sinusoidal, bi-linear and quadratic terms. The DC power flow approximation simplifies the nonlinear AC power flow equations. To derive the DC power flow equations from the AC power flow equations, the following assumptions are made:

- The voltage magnitude $|V_i|$ at each node is approximately equal to 1 per unit.

- The phase angle differences θ_{ij} between nodes are small, so that $\sin(\theta_{ij}) \approx \theta_{ij}$ and $\cos(\theta_{ij}) \approx 1$.
- The resistive losses (associated with G_{ij}) are negligible compared to the reactive components, so the conductance G_{ij} is approximated as zero.

Using these assumptions, the AC power flow equations simplify to the following DC power flow equations:

$$P_i \approx \sum_{j=1}^N B_{ij} \theta_{ij} \quad (2.5)$$

Here, the reactive power balance equation is not used, as the DC approximation only considers active power. The DC power flow equations provide a linear relationship between the power injections and the phase angles, which simplifies analysis and computations when voltage and reactive power are not studied.

Although the DC power flow is beneficial for transmission system analyses due to its simplicity and linearity, it can not be used for distribution systems for the following reasons,

- **Voltage Magnitude Variations:** In distribution systems, the voltage per unit magnitude can vary significantly from the substation to the end of the feeder. Therefore, the assumption that $|V_i| \approx 1$ pu does not hold.
- **High R/X Ratios:** The DC approximation assumes negligible line resistance. However, distribution lines often have high resistance to reactance (R/X) ratios, making resistive losses significant. Ignoring them can lead to inaccurate results.

- **Voltage-Dependent Loads:** Loads in distribution systems can be highly voltage-dependent which can not be captured by the DC model.
- **Unbalanced Nature:** Most distribution systems are unbalanced due to single-phase loads. However, the DC power flow model uses positive-sequence model, which is essentially a balanced three-phase approach that is unsuitable for unbalanced operating conditions.

In the next section, the unbalanced distribution power flow is described.

2.3 UNBALANCED DISTRIBUTION POWER FLOW

Consider a three-phase, radial graph G , wherein each node represents three phases: a , b , c . Similarly, each branch represents a three-phase line section with a corresponding 3×3 impedance matrix, which is expressed as,

$$z_{ij}^{3\phi} := \begin{bmatrix} z_{ij}^a & z_{ij}^{ab} & z_{ij}^{ac} \\ z_{ij}^{ba} & z_{ij}^b & z_{ij}^{bc} \\ z_{ij}^{ca} & z_{ij}^{cb} & z_{ij}^c \end{bmatrix} \forall (i, j) \in \mathcal{E}. \quad (2.6)$$

Voltage at 3-phase node i is denoted $V_i^{3\phi} = [V_i^a, V_i^b, V_i^c]^\top$ and current in branch $(i, j) \in \mathcal{E}$ is $I_{ij}^{3\phi} = [I_{ij}^a, I_{ij}^b, I_{ij}^c]^\top$. The line voltage drop and currents are related by

$$\Delta V_{ij}^{3\phi} := V_i^{3\phi} - V_j^{3\phi} = z_{ij}^{3\phi} I_{ij}^{3\phi} \Rightarrow \Delta V^{3\phi} = Z^{3\phi} I^{3\phi}, \quad (2.7)$$

where, $I^{3\phi} = [I_{ij}^{3\phi}]_{(i,j) \in \mathcal{E}} \in \mathbb{C}^{3(N-1)}$ represents the complex three-phase currents, $V^{3\phi} =$

$[V_i^{3\phi}]_{i \in \mathcal{V}} \in \mathbb{C}^{3N}$ corresponds to the three-phase voltages, $Z^{3\phi} \in \mathbb{C}^{3(N-1) \times 3(N-1)}$ is the complex three-phase impedance matrix. One of the most common methods to solve the unbalanced power flow is Backward/Forward sweep, which can be summarized as follows,

The backward/forward sweep method for radial distribution networks is described as:

1. Initialization:

- Set initial voltage values for all nodes.
- Calculate load currents based on initial voltage values.

2. Backward Sweep:

- Starting from end nodes, propagate currents upstream.

3. Forward Sweep:

- Update node voltages based on branch impedances and calculated currents.

4. Convergence Check:

- If maximum difference in voltage between iterations is below a threshold, the method has converged. Otherwise, return to the Backward Sweep.

DER coordination is described next, as a viable solution to provide synthetic damping and inertia in the power system. The term *synthetic* pertains to the introduction of additional damping and inertia through a controller, as opposed to the conventional damping and inertia, which arise as a natural response in synchronous machines to changes in frequency.

2.4 DER COORDINATION

P_j^{DER} in (2.1b) can be controlled in order to provide different ancillary services. To do so, DERs need to follow a reference signal. This work employs three distinct DER coordination methods: Packet-based, Fitness-based, and Optimization-based coordination. A brief description of each is provided in the following sections.

2.4.1 OPTIMIZATION-BASED DER COORDINATION

A naive approach to achieve the coordinator's objectives is to, at each time step, schedule the on/off state of TCLs using optimization-based methods:

$$\min_{s_n[k]} w_1 \epsilon + w_2 \sum_{n=1}^N (z_n[k+1] - z_n^{\text{set}})^2 \quad (2.8a)$$

$$\text{s. t. } z_n^{\min} \leq z_n[k] \leq z_n^{\max} \quad \forall n \quad (2.8b)$$

$$|P_{\text{ref}}[k] - \sum_{n=1}^N s_n[k] P_n^{\text{rate}}| \leq \epsilon \quad (2.8c)$$

$$s_n[k] \in \{0, 1\} \quad (2.8d)$$

where $z_n[k]$ is the DER's dynamic state, P_{ref} is the reference signal, $s_n[k]$ is the operating state, and P_n^{rate} is the power rating of DER n . ϵ is chosen smaller than P_n^{rate} . The method assumes full knowledge of the fleet's dynamic state. This means that for every time step, all of the devices must send their temperature data to the coordinator. This results in a large communication overhead, which challenges implementation at scale. In addition, the cycling of devices is not captured in the formulation, which can potentially result in the DER's wear and tear and reduction

in the device's operating life.

Packet-based DER coordination is introduced next.

2.4.2 PACKET-BASED DER COORDINATION

Packet-based DER coordination is enabled by a cyber-physical system that coordinates incoming and asynchronous discrete grid-access requests for energy from individual DERs [2, 51–53]. The DER's asynchronous requests are central to packet-based coordination and are explained next.

Definition 3. (*Energy packet*) *An energy packet is a fixed-duration and fixed-power epoch of energy consumed (or delivered) by a DER.*

In packet-based schemes, each DER requests an energy packet based on its need for energy (NFE). The requests are given by the following cumulative distribution function:

$$P_{\text{req}}^{\text{ch}}(z_n[k]) := 1 - e^{-\mu(z_n[k])\Delta t}, \quad (2.9)$$

where $\mu(z_n[k]) > 0$ is a rate parameter dependent on the local SoC and is defined as,

$$\mu(z_n[k]) = \begin{cases} 0, & \text{if } z_n[k] \geq \bar{z}_n \\ m_R \left(\frac{\bar{z}_n - z_n[k]}{z_n[k] - \underline{z}_n} \right) \cdot \left(\frac{z_n^{\text{set}} - \underline{z}_n}{\bar{z}_n - z_n^{\text{set}}} \right), & \text{if } z_n[k] \in (z_n, \bar{z}_n) \\ \infty, & \text{if } z_n[k] \leq \underline{z}_n \end{cases}, \quad (2.10)$$

where $m_R > 0$ [Hz] is a design parameter that defines the mean time-to-request

(MTTR) for $z_n[k] = z_n^{\text{set}}$. A similar expression follows for $\mu(z_n[k])$ and $P_{\text{req}}^{\text{dis}}(z_n[k])$ in the case of *discharging* packets.

DERs considered in this manuscript represent residential water heaters, EV chargers, and/or residential batteries, whose energy (e.g., temperature and SoC) dynamics are much slower than the frequency response. This means that during the primary frequency control period, the specific model of the DERs is not significant, as long as their power consumption is adjustable. For example, if an air conditioner (A/C) measures a room temperature in the summer above some desired set-point, then the room temperature is too high and the device's NFE increases. This leads to more frequent requests for energy packets to cool down the room. Similarly, if the A/C measures a low room temperature, the NFE decreases and the device will not request an energy packet often, if at all. The energy packet requests then arrive from devices asynchronously and each request is either accepted or rejected by the coordinator based on aggregate demand and a market or grid reference signal. When a request for an energy packet is accepted, an internal timer for the switched device is triggered and the DER charges or discharges until the timer's absolute value equals the packet length (or epoch length). When the n^{th} DER has its charging request accepted at time k , then $C_n[k+1] = C_n[k+2] = \dots C_n[k+n_p] = 1$. On the other hand, if a discharging request packet is accepted at time k , $C_n[k+1] = C_n[k+2] = \dots C_n[k+n_p] = -1$. Otherwise, $C_n[k+1] = 0$. C_n is 1 when the device is charging, -1 when the device

discharges, and 0 when the device is OFF. The local timer for DER n is described as

$$t_n[k+1] = \begin{cases} t_n[k] + \Delta t, & \text{if } C_n[k] = 1 \\ t_n[k] - \Delta t, & \text{if } C_n[k] = -1 \\ 0 & \text{otherwise} \end{cases}, \quad (2.11)$$

where Δt is the sampling time, the number of bins is $n_p := \lfloor \delta / \Delta t_B \rfloor$ and Δt_B is the timer bin width. The packet duration (epoch) is denoted δ and typically is set between 60 to 600 seconds. Without loss of generality, one can choose $\Delta t = \Delta t_B$.

Even though the coordinator does not have access to the individual DERs' internal timers, it knows how many requests were accepted at each time step in addition to packet height P_n^{rate} for each request, which permits the coordinator to construct an accurate estimate of the DER fleet's aggregate timer. In general, the coordinator needs to consider four different timers using (2.11); *i*) Charge-only timer which includes devices that only can be charged, such as TCLs and ACs; *ii*) Discharge-only timer which includes devices that can only be discharged, such as solar panels and stand-alone gen-sets; *iii*) Charging bi-directional devices, such as energy storage systems (ESS); *iv*) discharging bi-directional devices. In this dissertation, the focus is on DER fleets of TCLs and ESSs, therefore, its three corresponding timers are (*i, iii, iv*). Since all accepted DERs start their packet at the first bin, the linear timer dynamics is defined by

$$\begin{aligned} x_{\text{tcl}}^{\text{ch}}[k+1] &= Mx_{\text{tcl}}^{\text{ch}}[k] + Bq_{\text{tcl}}^{\text{ch}}[k], \\ x_{\text{ess}}^{\text{ch}}[k+1] &= Mx_{\text{ess}}^{\text{ch}}[k] + Bq_{\text{ess}}^{\text{ch}}[k], \\ x_{\text{ess}}^{\text{dis}}[k+1] &= Mx_{\text{ess}}^{\text{dis}}[k] + Bq_{\text{ess}}^{\text{dis}}[k], \end{aligned} \quad (2.12)$$

where $x_{\text{tcl}}^{\text{ch}}, x_{\text{ess}}^{\text{ch}}, x_{\text{ess}}^{\text{dis}} \in \mathbb{R}^{n_p}$ are binned distributions of power for charge-only TCLs, bidirectional charging ESS, and bidirectional discharging ESS, respectively, while $q_{\text{tcl}}^{\text{ch}}[k], q_{\text{ess}}^{\text{ch}}[k], q_{\text{ess}}^{\text{dis}}[k] \in \mathbb{R}$ are the total power of accepted charging TCL, charging ESS, and discharging ESS requests during time step k , respectively. That is, $q_{\text{tcl}}^{\text{ch}}[k] = \sum_{n \in I[k]} P_n^{\text{rate}}$, where $I[k]$ is the set of DERs with accepted requests at time k . The timer dynamics are defined by $M \in \mathbb{R}^{n_p \times n_p}$, which is a lower triangular matrix with 1's on the lower off-diagonal and zero elsewhere, while $B := [1, 0, \dots, 0]^T \in \mathbb{R}^{n_p}$. Thus, when a request is accepted, the accepted DER enters the first bin, and at each time step it propagates through the timer. The number of devices completing their packets at time-step $k + 1$ is equal to the number of devices in the last bin of the timer distribution. During a frequency event, the distribution can be considered constant because the timer states evolve slower than the grid frequency. That is, if a frequency event occurs at k , states $x_{\text{tcl}}^{\text{ch}}[k], x_{\text{ess}}^{\text{ch}}[k], x_{\text{ess}}^{\text{dis}}[k]$ can be assumed constant since frequency response is a fast event (i.e., $< 10\text{s}$).

It is clear that the timer states are a function of past coordinator packet acceptance rates. During the frequency event, packets actively participate in the frequency response based on their internal timer states. Therefore, the concept of packet participation is presented next by extending the packet interruption defined in [54].

Definition 4. (*Packet participation*) *The packet's participation is the forced change of DER n 's local state $C_n[k]$ before the end of its epoch length (i.e., $t_n < \delta$) due to a frequency deviation event.*

To explain the role of packet participation, first, consider the power draw for a general DER n . Its power consumption at time step k is $P_n[k] \in [\underline{P}_n, \overline{P}_n]$, where $\underline{P}_n = 0$ for TCLs and $= -P_n^{\text{cap}} < 0$ for (discharging) ESS and $\overline{P}_n = P_n^{\text{cap}} > 0$

when ON (TCL) or charging (ESS). P_n^{cap} is the power rating of DER n . DER n is then participating in FFR, if, for example, during an under-frequency event, DER n changes its consumption from \overline{P}_n to \underline{P}_n . It is important to note that the formulation generalizes to the case when the DER reduces its power to a value larger than \underline{P}_n , as long as the coordinator is aware of the DER's available power change. If there is no ESS with $\underline{P}_n < 0$, packet participation refers to packet interruption as defined in [54] for TCLs only. The coordinator continuously monitors three distinct timers in real time. These timers encompass the binned power values of charging TCLs, charging bi-directional DERs, and discharging DERs, as illustrated in (2.12). By adding the values across the timer bins, the total power within each timer is obtained. To determine the total consumption of the entire fleet at time k , the total discharging power is subtracted from the total charging power as shown below,

$$P^{\text{DER}}[k] := \mathbf{1}_{n_p}^\top (x_{\text{tcl}}^{\text{ch}}[k] + x_{\text{ess}}^{\text{ch}}[k] + x_{\text{ess}}^{\text{dis}}[k]). \quad (2.13)$$

Based on measured grid frequency, the flexible (net) demand, P^{DER} , can then be actively modified via packet participation by selectively interrupting and/or “toggling” packets (e.g., charging at $P_n[k] = P_n^{\text{cap}} > 0$ toggles to discharging at $P_n[k] = -P_n^{\text{cap}} < 0$). The selection of which packets participate during any given frequency event will be based on a fully decentralized DER control law.

Remark. *Note that in some packet-based coordination schemes, devices can be interrupted before the completion of their packet to maintain quality of service, i.e. turned off in case of excessive temperature or turned ON in case of low temperature (also*

called *opt-out*) as discussed in [51]. In (2.12) the number of *opt-outs* is assumed negligible, which is reasonable when the DER fleet operates near nominal demand. The coordinator can further ensure that this assumption is valid by constraining operations to only track power reference signals close to its fleet’s nominal power. That is, tracking a signal with a relatively large amplitude can cause the devices to deviate from the set point, which in turn leads to more *opt-outs* and interruptions.

Next, we present a different indirect method called the fitness-based method, which, keeps a list of device priorities (i.e., ranked by their fitness to turn on and off) and then selects the fittest devices to actuate to minimize tracking error.

2.4.3 FITNESS-BASED METHOD

In the fitness-based method, each DER calculates fitness values based on its local dynamic state, $z_n[k]$, its operating state, $s_n[k]$, and its availability of response (e.g., is device locked, opted out, or otherwise unavailable) [55]. The coordinator then receives fitness values from DERs and sorts the devices based on their fitness values. This simplifies the coordinator’s process of actively determining which devices to turn on/off as the power reference signal changes.

Thus, this method depends on device computing and the coordinator ranking a set of fitness values. There are different ways to compute fitness values based on available (local) device information: $z_n[k]$, $s_n[k]$, including time since the last on/off transition.

DER fitness values

The fitness values for device n can be defined based only on the dynamic state:

$$F_n^{\text{ON}}[k] = 1 - \exp\left(-\frac{z_n^{\text{max}} - z_n[k]}{z_n[k] - z_n^{\text{min}} + \epsilon}\right) \in [0, 1] \quad (2.14a)$$

$$F_n^{\text{OFF}}[k] = 1 - F_n^{\text{ON}} \in [0, 1]. \quad (2.14b)$$

where ϵ is added for numerical stability. For example, for EWHs, if a device's temperature is low, then it has a high fitness value for turning ON (F_n^{ON}) and a low fitness value for turning OFF (F_n^{OFF}). This prioritizes EWHs with lower temperatures (high fitness) to be selected for turning on if the reference signal increases. Similar to Packaged energy management (PEM), an internal opt-out mechanism is incorporated in the scheme to ensure that the temperature comfort range ($z_n^{\text{min}}, z_n^{\text{max}}$) is not violated. In addition, when a device cycles, it may be locked on/off for a certain duration before it can cycle again. This locked device behavior reduces cycling (i.e., improves device quality of service (DQoS)) but also limits the availability of DERs.

Thus, to capture the availability and prioritize DQoS, a device can augment its fitness value with a DQoS term in the fitness function, as shown below:

$$F_n^{\text{ON}}[k] = \left(1 - \exp\left(-\frac{z_n^{\text{max}} - z_n[k]}{z_n[k] - z_n^{\text{min}}}\right)\right) \left(1 - \exp(-\tau_n^{\text{off}}[k])\right) \quad (2.15a)$$

$$F_n^{\text{OFF}}[k] = \exp\left(-\frac{z_n^{\text{max}}[k] - z_n[k]}{z_n[k] - z_n^{\text{min}}}\right) \left(1 - \exp(-\tau_n^{\text{on}}[k])\right) \quad (2.15b)$$

where $\tau_n^{\text{off/on}}$ is the time elapsed (in hours) since the last off/on transition. The DER will then send the coordinator its fitness values based on either (2.14) or (2.15), which is used in actively coordinating the DER fleet and described next.

None of the abovementioned schemes consider the impact of DER coordination on grid constraints. It should be noted that DER coordination if done on a large scale, can potentially lead to grid constraint violations. In the next section, a method is described that enables us to take into account grid constraints in DER coordination schemes.

2.5 DER HOSTING CAPACITY FOR BALANCED GRIDS

In this section, the objective is to determine the maximum and minimum DER power that can be added to a balanced distribution system without violating the grid's voltage and current constraints. The limits on the DER power are called HC in this dissertation. The CIA-based approach detailed in [42, 43] employs a CIA of the set of feasible admissible injections.

An optimization problem is used to determine the HC at each node of a distribution feeder based on the second order Taylor approximation of the *DistFlow* [56]. The total feeder HC is the sum across all nodes. Next, we discuss the single-phase equivalent load flow, i.e., *DistFlow*, and the convex HC formulation.

Consider a radial (single-phase) distribution feeder as a tree graph $G = (\mathcal{V}, \mathcal{E})$ with N nodes $\mathcal{V} := \{1, \dots, N\}$ and $N - 1$ branches $\mathcal{E} \subseteq \mathcal{V} \times \mathcal{V}$, such that if nodes i and j are connected, then $(i, j) \in \mathcal{E}$. At each node $i \in \mathcal{V}$, *DistFlow* considers the square of the voltage phasor magnitude, i.e., $V_i := |v_i|^2$ and complex power injections are denoted $s_i = p_i + \mathbf{j}q_i$. Node 0 is assumed to be the substation (slack) node with a fixed voltage V_0 . Through each branch with impedance $z_{ij} = r_{ij} + \mathbf{j}x_{ij}$, we consider the

square of the current phasor, i.e., $l_{ij} := |I_{ij}|^2$ and the active and reactive power flows, P_{ij} and Q_{ij} . Thus, from the *DistFlow* formulation and applying [57], the relationships between voltages and branch power flows and nodal injections and line currents can be defined as

$$V = V_0 \mathbf{1}_N + M_p p + M_q q - Hl \quad (2.16a)$$

$$P = Cp - D_R l \quad (2.16b)$$

$$Q = Cq - D_X l, \quad (2.16c)$$

where appropriately-sized matrices M_p , M_q , H , C , D_R , D_X are detailed in [42, 43] and serve to map injections and currents to corresponding voltages and branch power flows across the network. Besides the linear equations in (2.16), the *DistFlow* also relates voltages and power flows to currents via non-convex

$$l_{ij}(P, Q, V) = (P_{ij}^2 + Q_{ij}^2)/V_i. \quad (2.17)$$

The non-linear (2.17) makes the *DistFlow* formulation non-convex within an optimal power flow (OPF) setting. Thus, we are interested in utilizing a CIA of the *DistFlow* formulation. A brief description of CIA is provided below,

2.5.1 CONVEX INNER APPROXIMATION

The CIA effectively bounds the nonlinear l_{ij} with a convex envelope: $l^-(P, Q, V) \leq l_{ij}(P, Q, V) \leq l^+(P, Q, V)$, which enables the creation of two sets of variables: upper (+) and lower proxies (-), e.g., $V^- \leq V \leq V^+$. As long as the lower proxies satisfy

lower limits and upper proxies satisfy upper limits, e.g., $\underline{V} \leq V^-$ and $V^+ \leq \bar{V}$, then we are guaranteed that the physical variable satisfies, e.g., $\underline{V} \leq V \leq \bar{V}$. This guarantee means that we can replace the physical variables altogether and replace them with their convex proxies.

Consider for example a feeder with inductive branches, i.e., $x_{ij} > 0$, $\forall(i, j) \in \mathcal{E}$ [42]. Then, we can replace the non-convex formulation in (2.16) and (2.17) with their convex proxies:

$$V^+ = V_0 \mathbf{1}_N + M_p p + M_q q - Hl^- \quad (2.18a)$$

$$V^- = V_0 \mathbf{1}_N + M_p p + M_q q - Hl^+ \quad (2.18b)$$

$$P^+ = Cp - D_R l^- \quad (2.18c)$$

$$P^- = Cp - D_R l^+ \quad (2.18d)$$

$$Q^+ = Cq - D_X l^- \quad (2.18e)$$

$$Q^- = Cq - D_X l^+. \quad (2.18f)$$

$$l^+ \geq f_{\text{quad}}(P^+, P^-, Q^+, Q^-, V^+, V^-) \quad (2.18g)$$

$$l^- := f_{\text{aff}}(P^+, P^-, Q^+, Q^-, V^+, V^-), \quad (2.18h)$$

where l^- is affine in the proxy variables while l^+ is a convex relaxation of a quadratic function of the proxy variables. Please see Appendix A for derivations of f_{aff} and f_{quad} and [42, 43] for full details. Finally, the feeder HC is then the maximum sum of nodal injections, $p_i^+ := p_i^*$, that drives the feeder to its capacity (e.g., voltage, current, or power flow limits are active). The convex formulation that achieves this objective

is

$$\mathbf{P}_{\text{CIA}}^{\phi,+} : \quad p^+ := \arg \max_{p_i} \sum_{i=1}^N w_i p_i \quad (2.19a)$$

$$\text{subject to (2.18)} \quad (2.19b)$$

$$\underline{l} \leq l^- \quad l^+ \leq \bar{l} \quad (2.19c)$$

$$\underline{V} \leq V^- \quad V^+ \leq \bar{V} \quad (2.19d)$$

$$p_i^2 + q_i^2 \leq \bar{s}_i^2, \quad \forall i \in \mathcal{V}, \quad (2.19e)$$

where w_i are design parameters that differentiate nodal capacities. Note that inequality (2.21e) is optional and captures limits on active injections based on apparent power limits at each node (e.g., from inverter, transformer, or power factor limits). Other constraints on $P^{+/-}, Q^{+/-}$ may also be added. The HC for DER injections (e.g., solar PV) is defined as

$$\overline{\text{HC}} := \sum_i^N p_i^+ = \mathbf{1}_N^\top p^+ > 0. \quad (2.20)$$

Similarly, we can define the HC relative to consumption (e.g., electric vehicle HC) as $\underline{\text{HC}} := \sum_i^N p_i^- = \mathbf{1}_N^\top p^- < 0$, where p^- is the solution that minimizes the nodal (net)

injections, i.e., solve corresponding $\mathbf{P}_{\text{CIA}}^{\phi,-}$ problem, as follows:

$$\mathbf{P}_{\text{CIA}}^{\phi,-} : \quad p^- := \arg \max_{p_i} \sum_{i=1}^N -w_i p_i \quad (2.21a)$$

$$\text{subject to (2.18)} \quad (2.21b)$$

$$\underline{l} \leq l^- \quad l^+ \leq \bar{l} \quad (2.21c)$$

$$\underline{V} \leq V^- \quad V^+ \leq \bar{V} \quad (2.21d)$$

$$p_i^2 + q_i^2 \leq \bar{s}_i^2, \quad \forall i \in \mathcal{V}, \quad (2.21e)$$

Thus, $\underline{\text{HC}} \leq 0 \leq \overline{\text{HC}}$.

However, since $\mathbf{P}_{\text{CIA}}^{\phi,+}$ and $\mathbf{P}_{\text{CIA}}^{\phi,-}$ employ a CIA of *DistFlow*, the HC estimates are valid only for balanced, radial distribution feeders. We are now interested in how to adapt this CIA-based method to a realistic unbalanced distribution feeder, which means that we need to consider the effects of mutual phase impedance and load unbalances. This will be addressed in chapter 5. In the next subsection, the virtual battery model is explained.

2.6 VIRTUAL BATTERY MODEL

ΔP_j^{DER} can be controlled through DER coordination, to provide different ancillary services. To do so, DERs need to follow a reference signal. The DER fleet's ability to track a reference signal highly depends on the state of charge (SoC) of the fleet which is defined as follows,

Definition 5 (State of charge of virtual Battery). *The SoC of a virtual battery represents the aggregated energy status of the DERs within the virtual battery, relative*

to their collective maximum capacity.

The physics-based modeling and estimation approach introduced in [58,59] is summarized next. These papers accurately estimate $\tilde{E}_{\text{avg}}[k]$ under specific fleet conditions (i.e., *homogeneous* device and control parameters). Using only the aggregate power consumption of the fleet, the incoming charging and discharging packet requests, and the total number of devices consuming/injecting power and opting out – all received and tracked by the coordinator. From this estimate, the authors use a physics-based predictive model of a fleet of homogeneous DERs into a so-called PEM *virtual battery* or *PEM-VB*. The PEM-VB is characterized by four salient dynamics states:

- Average energy, $E_{\text{avg}}[k]$.
- Total number of charging DERs, $N_{\text{on}}^{\text{ch}}[k]$.
- Total number of discharging DERs, $N_{\text{on}}^{\text{dis}}[k]$.
- Total number of Opt-outs, $N_{\text{opt}}[k]$.

These states are coupled through the incoming packet requests. For example, the higher $E_{\text{avg}}[k]$ is, the higher the fleet’s devices SoCs, which leads to a lower aggregate request rate (e.g., as EWHs heat up, they need less energy and how a lower probability of requesting a packet). Consequently, a lower request rate limits the fleet’s ability to ramp up its aggregate power.

Two types of DERs are used in this work, EWHs and batteries. In PEM, a DER with a local state-of-charge (SoC) $z_n[k]$ (e.g., temperature for an EWH or state of charge for a battery), is designed to operate within a deadband $[\underline{z}_n, \bar{z}_n]$ to maintain a certain level of consumer comfort. The dynamic state for EWH n is given by the

following equation:

$$z_n[k+1] = z_n[k] + \Delta t \left(\frac{\eta_n P_n^{\text{rate}}}{c_p \rho L_n} \phi_n[k] - \frac{z_n[k] - T_a[k]}{\tau_n} - \frac{Q_n[k]}{c_p \rho L_n} \right) \quad (2.22)$$

where $c_p = 4.186$ [kJ/kg-°C] is the specific heat constant for water, τ_n is the standing loss time constant to ambient temperature, ρ is the water density close to 50°C , L_n is the tank capacity in [Liters], η_n is the efficiency, P_n^{rate} is the power rating in [kW], and $\phi_n[k]$ is a binary variable determining if device n is on or off. T_a is the ambient temperature in [°C], Δt is the discretization time-step in [s], and $Q_n[k]$ is the heat loss from the tank due to water usage. The dynamic model of batteries is summarized by the following equation:

$$z_n[k+1] = z_n[k] + \Delta t (-\eta_n^{\text{st}} z_n[k] + \phi_n[k] P_n^{\text{rate}} \eta_n) \quad (2.23)$$

where $\phi_n[k]$ is +1 if the device is discharging, and is -1 if device n is charging at time k . If the device is in standby mode, $\phi_n[k] = 0$. The efficiencies for standing losses and charging are η_n^{st} and η_n , respectively.

Each DER measures its local SoC, $z_n[k]$. If the SoC is outside the deadband, $z_n[k] \notin [\underline{z}_n, \bar{z}_n]$, the DER automatically and temporarily opts out of PEM to guarantee QoS and reverts to a conventional control mode until the SoC is returned within limits after which it returns to PEM operation. If the SoC is within the deadband, $z \in [\underline{z}_n, \bar{z}_n]$, the DER probabilistically requests the PEM coordinator to either consume power from the grid (charging) or inject power into the grid (discharging) for a pre-specified epoch. The epoch corresponding to the energy packet is called packet length and denoted as δ_p . The requests are given by the following cumulative distribution

function:

$$P_{\text{req}}^{\text{ch}}(z_n[k]) := 1 - e^{-\mu(z_n[k])\Delta t}, \quad (2.24)$$

where $\mu(z_n[k]) > 0$ is a rate parameter dependent on the local SoC and is defined as,

$$\mu(z_n[k]) = \begin{cases} 0, & \text{if } z_n[k] \geq \bar{z}_n \\ m_R \left(\frac{\bar{z}_n - z_n[k]}{z_n[k] - \underline{z}_n} \right) \cdot \left(\frac{z_n^{\text{set}} - \underline{z}_n}{\bar{z}_n - z_n^{\text{set}}} \right), & \text{if } z_n[k] \in (\underline{z}_n, \bar{z}_n) \\ \infty, & \text{if } z_n[k] \leq \underline{z}_n \end{cases}, \quad (2.25)$$

where $m_R > 0$ [Hz] is a design parameter that defines the mean time-to-request (MTTR) for $z_n[k] = z_n^{\text{set}}$. A similar expression follows for $\mu(z_n[k])$ and $P_{\text{req}}^{\text{dis}}(z_n[k])$ in the case of *discharging* packets.

Under homogeneous fleet parameter assumptions, one can consider the fleet's average power via (2.22) and, by assuming a constant average hot water consumption, μ_Q , get the following expression for estimating the average temperature for an EWH fleet, $\tilde{E}_{\text{avg}}[k]$:

$$\tilde{E}_{\text{avg}}[k+1] = \left(1 - \frac{\Delta t}{\tau}\right) \tilde{E}_{\text{avg}}[k] + \frac{\Delta t T_a}{\tau} - \frac{\Delta t \mu_Q}{c_p \rho L} + \frac{\eta \Delta t P^{\text{rate}} (N_{\text{on}}^{\text{ch}}[k] + N_{\text{opt}}[k])}{c_p \rho L N}, \quad (2.26)$$

The change in \tilde{E}_{avg} depends on the number of charging EWHs as well as background demand. T_a is assumed to be constant in this work. A similar expression can be obtained for a battery fleet using Equation 2.23. Note that the above expression

is only valid when the parameters τ , L , P^{rate} , z , and \bar{z} are common across all devices in the fleet (i.e., the homogeneity assumption). Clearly, the average SoC increases the more ON and opt-out devices there are, which are states driven by the rate of accepted requests. The requests only come from devices in standby mode (i.e., not in ON (charging or discharging) and not in opt-out modes) and are driven by $\tilde{E}_{\text{avg}}[k]$ and the request probabilistically in Equation 2.24. Therefore, the number of charging requests received by the coordinator during the interval k is,

$$x_r^{\text{ch}}[k] = P_{\text{req}}(\tilde{E}_{\text{avg}}[k])(N - N_{\text{on}}^{\text{ch}}[k] - N_{\text{on}}^{\text{dis}}[k] - N_{\text{opt}}[k]) \quad (2.27)$$

A similar expression can be obtained for the estimated number of discharging requests, $x_r^{\text{dis}}[k]$. Define $\beta_{\text{ch}}[k]$ and $\beta_{\text{dis}}[k]$ as the ratio of accepted charging and discharging requests during interval k , respectively. Then $\beta_{\text{ch}}^-[k]$ and $\beta_{\text{dis}}^-[k]$ are the proportion of expired charging and discharging requests during interval k , respectively. The dynamics of the number of ON (charging and discharging) devices can be expressed as:

$$N_{\text{on}}^{\text{ch}}[k+1] = N_{\text{on}}^{\text{ch}}[k] + \beta_{\text{ch}}[k]x_r^{\text{ch}}[k] - \beta_{\text{ch}}^-[k]N_{\text{on}}^{\text{ch}}[k], \quad (2.28)$$

$$N_{\text{on}}^{\text{dis}}[k+1] = N_{\text{on}}^{\text{dis}}[k] + \beta_{\text{dis}}[k]x_r^{\text{dis}}[k] - \beta_{\text{dis}}^-[k]N_{\text{on}}^{\text{dis}}[k]. \quad (2.29)$$

From this, it is clear that the number of ON devices increases if the coordinator accepts more (new) device requests than are expiring (i.e., completing their packet).

Finally, to capture the total number of devices opted out at timestep k , we consider

the number of devices opting out and the number of devices opting back in as follows:

$$N_{\text{opt}}[k + 1] = N_{\text{opt}}[k] + \mathcal{E}_{\text{opt-out}}[k] - \mathcal{E}_{\text{opt-in}}[k] \quad (2.30)$$

where $\mathcal{E}_{\text{opt-out}}[k]$ and $\mathcal{E}_{\text{opt-in}}[k]$ are the number of opt-outs and opt-ins during timestep k , respectively.

In [59], the model described by (2.26)-(2.30) is applied to a homogeneous fleet of EWHs. An extended Kalman filter (EKF) was then developed to accurately estimate \tilde{E}_{avg} . However, under heterogeneous conditions and for a collection of mixed DERs (e.g., batteries and EWHs), the model to estimate \tilde{E}_{avg} is not applicable. One common workaround is to decompose the fleet into different homogeneous groups and then model each group as a VB [60]. However, such approaches rely on the assumption that each device's set of parameters is accurately known, which is impractical [15]. Thus, in the case of a heterogeneous and diverse fleet of DERs, the above methods are not directly applicable, modeling becomes challenging and complex, and no guarantees exist on the observability of \tilde{E}_{avg} .

CHAPTER 3

DER COORDINATION TO PROVIDE FAST FREQUENCY RESPONSE

In this section, a method is presented to provide FFR, also called primary frequency control using DER coordination schemes with the assumption that the fleet is solely used for FFR. Next, we will generalize the methodology for the case where the fleet is used for both primary and secondary frequency control. The proposed scheme can be applied to any packet-based energy management. The main goals of this section can be summarized as follows:

- A responsive and fully decentralized frequency control policy is designed within a packet-based energy management system that automatically prioritizes resources based on local dynamic states.
- The decentralized energy packet interruption controller is generalized to consider bi-directional DERs and RoCoF to improve the fleet's response during either under- or over-frequency events.

- Using limited information available to the coordinator, the synthetic damping available from a fleet of packetized resources can be precisely estimated in real time.
- Spectral analysis of historical AGC data is used to develop and compute a probabilistic lower bound on the expected synthetic damping available from a fleet. This lower bound can be used to analyze the trade-off between a fleet's expected primary and secondary frequency control capabilities.
- Simulation-based analysis is provided on practical considerations for packet-based DER coordination and synthetic damping, such as local measurement resolution and sensing/controller delays.

3.1 DECENTRALIZED FREQUENCY CONTROL USING PACKET-BASED ENERGY COORDINATION

To design a decentralized control policy for PEM, one needs to consider the local data/measurements available to each DER n at node i : 1) frequency, $f_i[k]$, 2) temperature, $T_n[k]$, and 3) timer state, $t_n[k]$. These enable each DER to make local ON/OFF decisions. In that context, each DER decides whether or not requests should be sent to the aggregator. In other words, when a PEM-enabled DER senses that the frequency deviation exceeds a predefined dead band, the DER blocks requests locally and switches to a decentralized control policy. This is detailed next.

A dead band around nominal frequency, f_0 , is set in order to define the transmission reliability criteria. Within this dead band, Δf_{db} , conventional PEM is used to provide ancillary and wholesale energy market services. However, deviating beyond the dead band represents reliability concerns, so PEM-enabled DERs switch to a decentralized control policy to actively support primary frequency response.

For the sake of simplicity, this subsection focuses on EWHs. A more generalized case with both EWHs and batteries will be presented next. As mentioned earlier, the dynamic state of devices evolves slowly and does not change during the frequency event. In addition, the aggregator knows the timer state distribution. Therefore, one can estimate how the number of packet interruptions affects the damping provided by PEM devices (D_{PEM}). The analysis performed herein assumes a fleet whose aggregate energy dynamics (e.g., distribution of device temperatures) are not changing much with time. Under this assumption, the timer states distribution follows a uniform distribution, which simplifies analysis. Consider using PEM for tracking a slowly moving reference signal and the frequency is maintained close to the nominal frequency. Fig. 3.1 shows the distribution of timer states ($t_n[k]$) and temperatures ($T_n[k]$) for devices n that are ON at time-step k for an example system of 400,000 EWHs. The number of bins for temperature and timer status is 30 and 10, respectively, and $\delta=3$ minutes. The histogram of timers in Fig. 3.1 is constructed using (2.11) and (2.12) while the histogram of temperatures must be estimated. Note that some of the devices with high t_n have low temperatures because of recent high water usage. In addition, some of the devices with high temperatures have just started their timer. This is caused by the random nature of PEM requests. The clear correlation between temperature and timer occurs because the more energy that a

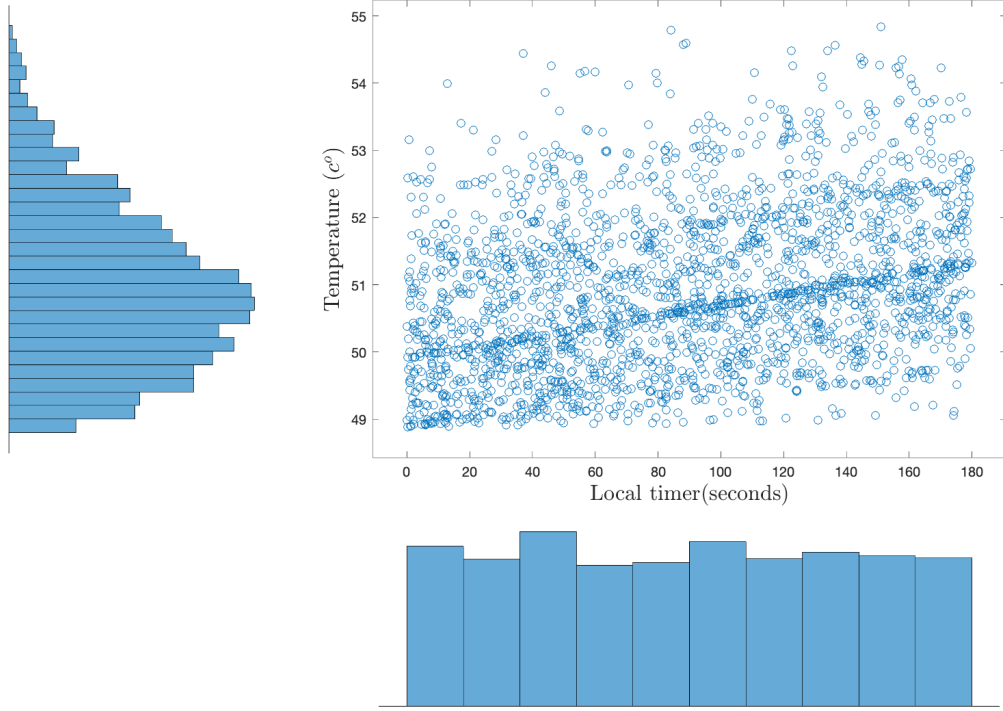


Figure 3.1: The state of local timers and temperature of ON devices before the disturbance.

device consumes, the higher the temperature. For simplicity, The DER capacities are assumed homogeneous. The dashed line shows the average number of devices in each bin, which is

$$\bar{x}[k] = \frac{1}{n_p}(\mathbf{1}_{n_p}^\top x[k]). \quad (3.1)$$

where $\mathbf{1}_{n_p} \in \mathbb{R}^{n_p}$ is vector of ones.

A naive initial approach to reduce demand implies automatically accepting or rejecting all packet requests during frequency disturbances. However, this does not offer a sufficient change in demand to affect the frequency response since such an

approach relies on slow packet completion rates. Another overly simplistic approach consists of interrupting all of the timers simultaneously when any frequency deviation occurs. This triggers a step change in demand that ignores the frequency's evolution and can cause system instabilities [61] if the share of DERs in the power system is significant. Therefore, it is necessary to prioritize devices so that the ones with higher timers or temperatures turn OFF first in under-frequency events. In fact, one needs to dynamically interrupt the packets to reduce demand and have a meaningful effect on the frequency.

In the proposed method, a packet interruption threshold is assigned to the local timer based on the local frequency measurement as shown in Fig. 3.2. That is, when the magnitude of frequency deviation is smaller than Δf_{db} , no control action is needed. The design of this dead zone depends on power system reliability requirements defined by transmission operators. For frequency deviations between Δf_{db} and Δf_{max} , $\eta \in [0, 1]$. If the frequency deviation is larger than Δf_{max} , the value of η will remain constant at $\eta_{\text{max}} \in [0, 1]$. Therefore, the only local design parameters are η_{max} , Δf_{db} , and Δf_{max} . For $\eta_{\text{max}} \approx 1$, the aggregate decentralized PEM response is more aggressive due to more interruptions for a given frequency deviation. A linear function is used for $\eta(\Delta f)$ which will result in an aggregate response that adds equivalent, constant damping to the system. The proposed local control law is given by:

$$\eta(\Delta f) = \begin{cases} 0, & \Delta f_{\text{db}} < \Delta f[k] \\ \frac{\Delta f[k] - \Delta f_{\text{db}}}{\Delta f_{\text{max}} - \Delta f_{\text{db}}} \eta_{\text{max}}, & \Delta f_{\text{max}} \leq \Delta f[k] \leq \Delta f_{\text{db}} \\ \eta_{\text{max}}, & \Delta f[k] < \Delta f_{\text{max}}. \end{cases} \quad (3.2)$$

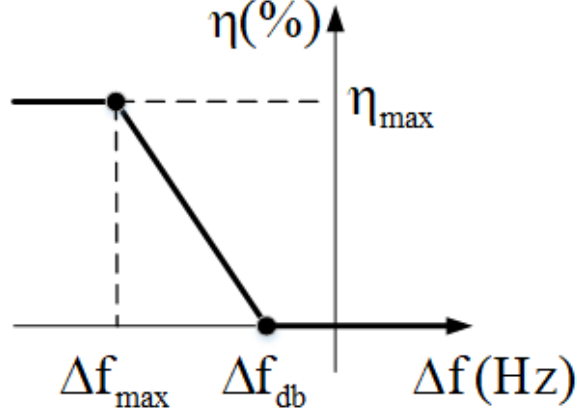


Figure 3.2: Illustrating the proportion of interrupted devices based on any locally measured frequency deviation from nominal, $\Delta f[k] := f[k] - f_0$.

The aggregate effect of the control law (3.7) in a simple two-area system is shown in fig. 3.3 for different values of η_{\max} . It can be seen that larger η_{\max} results in more damping. When η_{\max} is zero, none of the ON devices are interrupted. In this case, all of the requests are rejected locally and no new energy packet request is sent to the aggregator. Thus, consumption decreases with a constant rate equal to the packet completion rate which is $P^{\text{rate}}\bar{x}/\Delta t$. Observe in Fig. 3.3 that the packet completion rate is relatively slow and has a small impact on RoCoF (blue curve). Increasing packet interruption leads to a more sudden and larger drop in PEM demand for under-frequency events, which improves the RoCoF, maximum frequency deviation (also called the nadir point), and final frequency deviation. The demand starts to decrease, Δt seconds after the occurrence of disturbance. Table 3.1 shows RoCoF, Δf_{nadir} and final frequency deviation for different values of η_{\max} , which illustrates the effectiveness of the proposed prioritization scheme. As seen in Table 3.1, interrupting more energy packets (larger η_{\max}) improves the frequency response of the system.

Table 3.1: Characteristics of frequency response for different η_{max}

η_{max}	RoCoF (mHz/sec)	Δf_{Nadir} (mHz)	Δf_{∞} (mHz)
0	104	83	46
0.33	94	75	42
0.67	86	69	39
1	81	64	36

In a conventional power system, after a loss of generation, the frequency decreases rapidly until it achieves a minimum value and then it partially recovers due to the remaining generators' primary droop controllers and system damping. In this dissertation, Δf_{nadir} is defined as the frequency deviation at the nadir point. According to (3.7), when the frequency achieves its nadir point, η achieves its maximum value, which means that the largest proportion of devices are interrupted at this time. After the frequency recovers away from the nadir point, η decreases, but this does not change the number of interrupted devices since no new devices are turned ON after the nadir point. In other words, the frequency deviation at the nadir point provides the largest η , which determines the damping provided by the PEM fleet.

Clearly, the decentralized PEM scheme can provide damping as seen in Fig. 3.3. This damping is achieved with no coordination between DERs and aggregators. Being able to estimate the damping available from a fleet of DERs would be valuable for grid operators and market participants interested in FFR markets [62]. The next section provides an accurate online estimate of the equivalent damping provided by a fleet of DERs operating under (3.7).

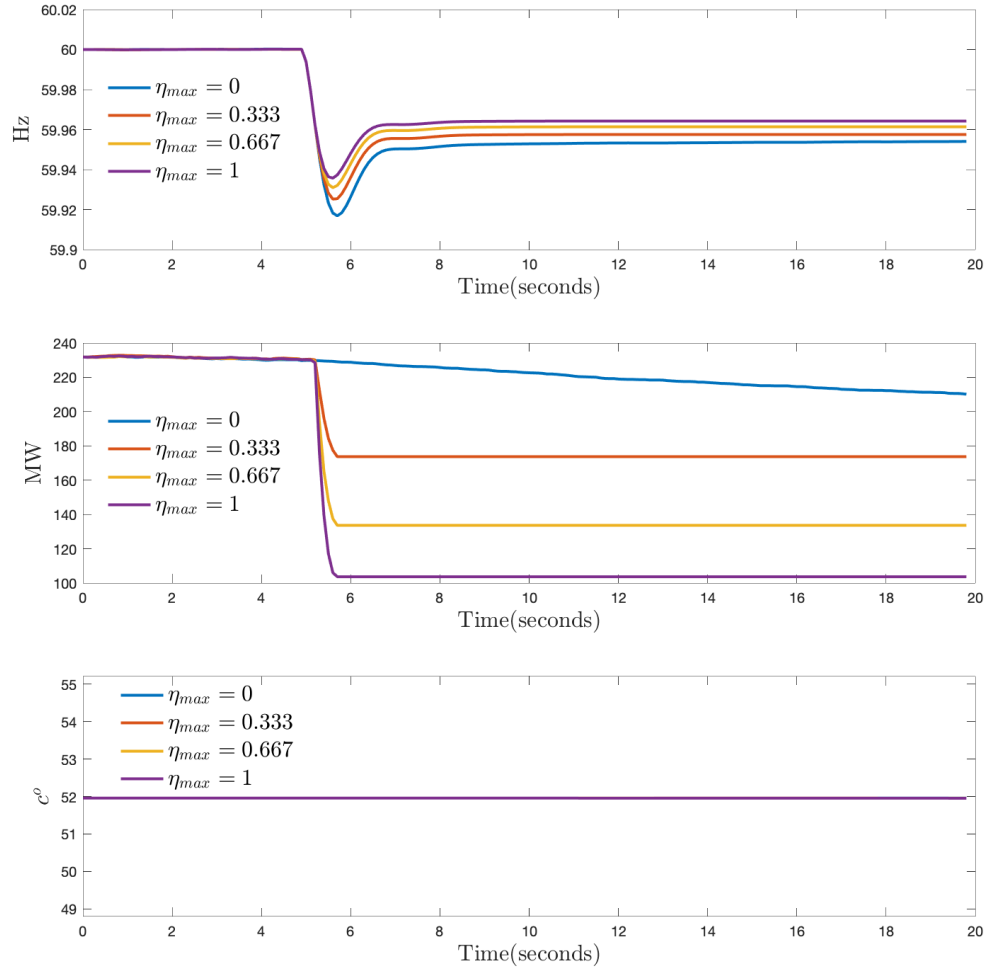


Figure 3.3: Aggregate power, frequency, and average temperature for different values of η_{max} for 400,000 DERs. A 500 MW drop in total generation occurs at $t = 5$ seconds.

3.2 PREDICTING THE AGGREGATE RESPONSE

In this section, the equivalent damping provided by a fleet of DERs operating under the decentralized control law in (3.7) is estimated analytically. In addition, (3.7) is augmented to combine both local timer and temperature information in the fully decentralized packet interruption scheme and estimate the resulting equivalent damping. While the PEM aggregator has direct access to the distribution of timer states, the temperature distribution required for the online estimate must be obtained indirectly with a state estimator [52, 63].

Next, an analytical estimate of the equivalent damping for just the aggregator's timer state distribution is provided.

3.2.1 TIMER-BASED PRIORITIZATION

In order to predict the equivalent PEM damping, the aggregator leverages available real-time information about the distribution of timer states. The aggregator makes use of the following simplifying assumptions that are reasonable in a practical setting, to estimate the damping.

Assumption 1. *The DER population is large enough and operates near nominal power so that the timer bins are well-approximated by $\bar{x}[k]$ in (3.1).*

Assumption 2. *The average number of devices at each bin \bar{x}_{nom} does not change with time. That is, $\bar{x}_{\text{nom}} \approx \bar{x}[k]$.*

Assumption 3. *The frequency response event duration is less than 30 seconds. That is, it is assumed that the nadir point is such that $\eta(\Delta f_{\text{nadir}}) > \frac{30}{\delta}$. This implies that*

one can neglect the effect of the packet completion rate.

For example, consider a PEM system with $\delta = 180$ s and frequency event with a nadir such that $\eta(\Delta f_{\text{nadir}}) = 0.9$. Then, all devices with timer state $t_n > 18$ are interrupted and natural packet completions will not occur for 162 seconds and can, therefore, be neglected. The analytical estimate is embodied by the following theorem.

Theorem 1. *Let δ , Δf and P^{rate} , and n_p be fixed for a DER fleet with decentralized control policy (3.7) and chosen η_{max} , Δf_{max} and Δf_{db} . Under assumptions 1, 2 and 3, the PEM fleet responds to frequency deviations with an equivalent damping of*

$$D_{\text{PEM}} = \begin{cases} 0, & \Delta f_{\text{db}} < \Delta f_{\text{nadir}} \\ P^{\text{rate}} \frac{\eta_{\text{max}} n_p \bar{x}_{\text{nom}}}{\Delta f_{\text{db}} - \Delta f_{\text{max}}}, & \Delta f_{\text{nadir}} \in [\Delta f_{\text{max}}, \Delta f_{\text{db}}] \\ P^{\text{rate}} \frac{\eta_{\text{max}} n_p \bar{x}_{\text{nom}}}{\Delta f_{\text{db}} - \Delta f_{\text{nadir}}}, & \Delta f_{\text{nadir}} < \Delta f_{\text{max}} \end{cases} \quad (3.3)$$

Proof. The proof is by construction. A PEM-enabled DER can either naturally complete or interrupt its packet. From (3.7), if $\Delta f_{\text{nadir}} > \Delta f_{\text{db}}$, then no device is interrupted and the PEM fleet is not responsive to the frequency, so the equivalent damping is zero.

For larger frequency deviations, assumption 3 ensures that one only has to consider packet interruptions. Thus, the total change in PEM load for system area j is described as:

$$\Delta P_j^{\text{PEM}}(\Delta f_{\text{nadir}}) = P^{\text{rate}} \sum_{i=[(1-\eta\Delta f_{\text{nadir}})n_p]}^{n_p} x_i[k], \quad (3.4)$$

where $x_i[k]$ is the i^{th} entry of an arbitrary timer states distribution $x[k]$. From As-

sumption 1, the total number of interruptions can be approximated by multiplying the total number of ON devices and $\eta(\Delta f_{\text{nadir}})$. Therefore, (3.4) can be rewritten as follows:

$$\Delta P_j^{\text{PEM}}(\Delta f_{\text{nadir}}) \approx P^{\text{rate}} \eta(\Delta f_{\text{nadir}}) (\mathbf{1}_{n_p}^\top x[k]), \quad (3.5)$$

In addition, from Assumption 2, $\mathbf{1}_{n_p}^\top x[k] \approx N_b \bar{x}_{\text{nom}}$. For $\Delta f_{\text{nadir}} \in [\Delta f_{\text{max}}, \Delta f_{\text{db}}]$, (3.7) gives $\eta(\Delta f_{\text{nadir}}) = \left(\frac{(\Delta f_{\text{nadir}} - \Delta f_{\text{db}}) \eta_{\text{max}}}{\Delta f_{\text{max}} - \Delta f_{\text{db}}} \right)$ and substituting this into (3.5) yields

$$\Delta P_j^{\text{PEM}}(\Delta f_{\text{nadir}}) = P^{\text{rate}} \left(\frac{(\Delta f_{\text{nadir}} - \Delta f_{\text{db}}) \eta_{\text{max}}}{\Delta f_{\text{max}} - \Delta f_{\text{db}}} \right) n_p \bar{x}_{\text{nom}}.$$

Since this change in power occurs over frequency deviation $\Delta f_{\text{nadir}} - \Delta f_{\text{db}}$, the equivalent damping in (3.3) is obtained.

Finally, for $\Delta f_{\text{nadir}} < \Delta f_{\text{max}}$, (3.7) saturates and $\eta(\Delta f_{\text{nadir}}) = \eta_{\text{max}}$. Then, $\Delta P_j^{\text{PEM}}(\Delta f_{\text{nadir}}) \approx P^{\text{rate}} \eta_{\text{max}} N_b \bar{x}_{\text{nom}}$. The equivalent damping is then $\frac{\Delta P_j^{\text{PEM}}(\Delta f_{\text{nadir}})}{\Delta f_{\text{nadir}} - \Delta f_{\text{db}}}$, which results in (3.3). This concludes the proof. \square

Remark. *Theorem 1 allows the PEM fleet to be modeled as a proportional controller with gain D_{PEM} . In the case of arbitrary reference signal, D_{PEM} will no longer be constant for all $\Delta f_{\text{nadir}} \in [\Delta f_{\text{max}}, \Delta f_{\text{db}}]$.*

Next, the proposed scheme is implemented on a two-area system to verify its performance.

3.3 NUMERICAL VALIDATION WITH TWO-AREA SYSTEM

Consider the so-called two-area model [64]. When a fleet of DERs under PEM interact with this system as in Fig. 3.4, the steady-state frequency deviation and damping for a two area system are given, respectively, by

$$\begin{aligned} \Delta f_\infty &= \frac{\Delta P_G}{D_{\text{PEM}}^{\text{actual}} + 2(D_j + \frac{1}{R_j})} \text{ and} \\ D_{\text{PEM}}^{\text{actual}} &= \frac{\Delta P_G}{\Delta f_\infty} - 2 \left(D_j + \frac{1}{R_j} \right), \end{aligned} \quad (3.6)$$

where D_j and R_j are the damping in MW/Hz and droop constant in Hz/MW in each area j . It is assumed that the two areas are equal, i.e., $D_1 = D_2$ and $R_1 = R_2$. Here, it has been assumed that both areas have equal damping and inertia. PEM loads and generation drops are in area 2. The two-area system parameters and simulation setup with respect to PEM are presented in table 3.2. Fig. 3.4 depicts the two area systems interacting with PEM loads. Equation (3.6) is used to compute the actual damping of the system in simulations. In what follows, $D_{\text{PEM}}^{\text{actual}}$ will be compared against (3.3) in Theorem 1.

3.3.1 EQUIVALENT DAMPING OF PEM LOADS

As seen in the previous subsection, when energy packets are interrupted ($\eta_{max} \neq 0$), the number of natural completions during the disturbance is negligible. Therefore, (3.3) can be used to calculate the estimated damping of the population of PEM

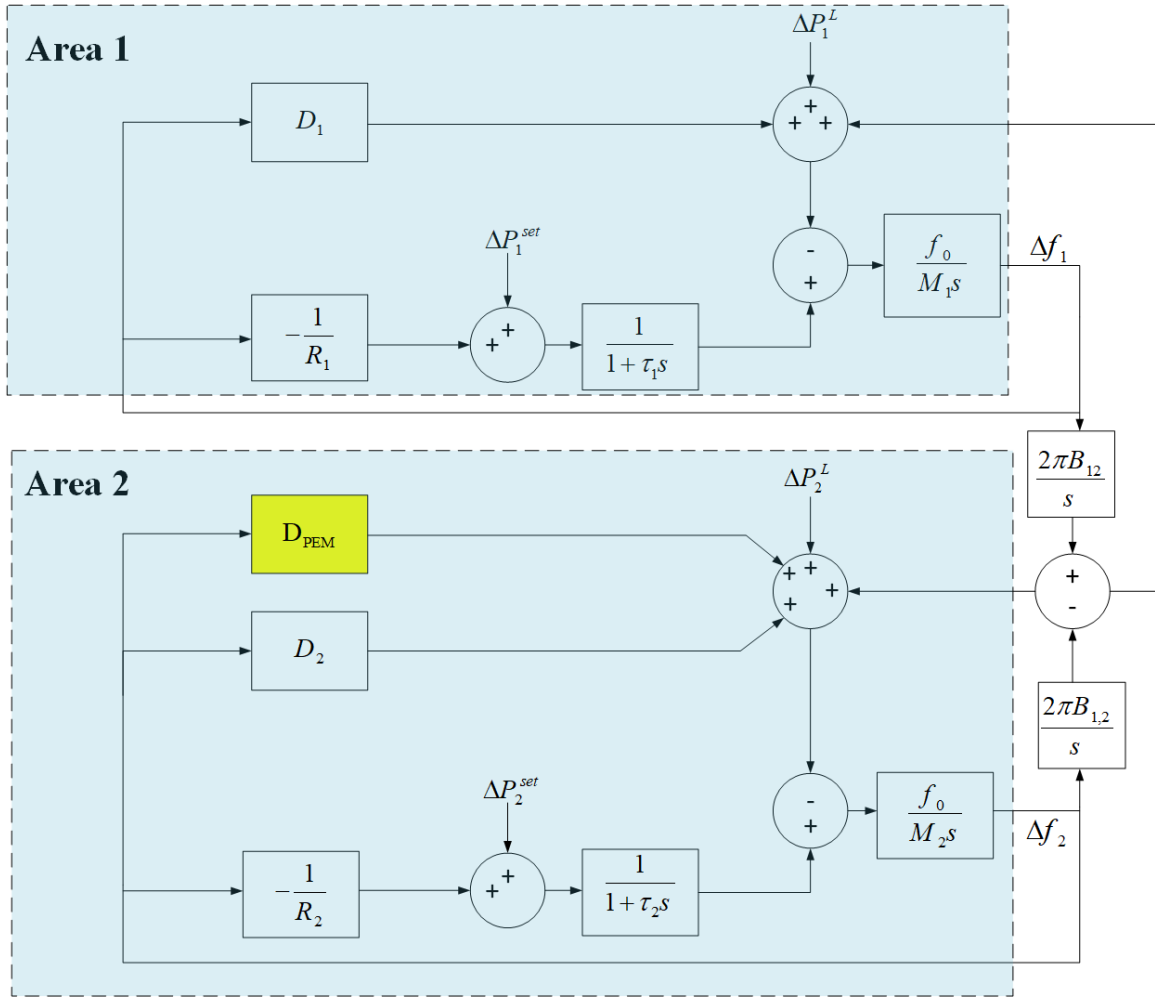


Figure 3.4: Block diagram of primary frequency control of a two-area power system

Table 3.2: Simulation Parameters

Parameter	Value
H	5 seconds
f_0	60 Hz
D_j	200 MW/Hz
R_j	$\frac{1}{5000}$ Hz/MW
Δf_{db}	20 mHz
Δf_{max}	100 mHz
T_n^{set}	52 C°
T_n^{max}	55.2 C°
T_n^{min}	48.8 C°
Δt	100 ms
Simulation Time	20 seconds
MTTR	3 min
Fleet size	400,000
Disturbance	-500MW @ $t = 5$ sec
Epoch	3 min

loads. Then, the PEM fleet operating under decentralized control policy from (3.7) can be modeled as a simple, lumped proportional frequency-responsive demand D_{PEM} . Fig. 3.5, compares simulation results using PEM loads against equivalent proportional controller. It can be seen that for $\eta_{max} = 0$, the error is higher compared to other cases since packet completion rates are not negligible. The Root Mean Square Error (RMSE) for different values of η_{max} and relative error in damping estimation is presented in table 3.3. The estimation error is calculated as $100 \times \frac{D_{PEM}(\Delta f_{nadir}) - D_{PEM}^{actual}}{D_{PEM}^{actual}}$. The results show that the relative accuracy of the damping estimate improves as the frequency deviation increases, however, for all estimates, the resulting frequency response in Fig. 3.5 matches closely with $RMSE < 1.2mHz$. The estimate is made solely based on the distribution of timers, which is available to the aggregator. No online measurements or communication are required for DERs to respond to frequency. The

error in the blue curve, representing the case with no packet interruptions, is attributed to the unmodeled packet expiration. When frequency deviation occurs, the threshold is reduced, causing packets that are closer to the end of their epoch to be interrupted, turning them off (in an under-frequency event). Therefore, as the frequency starts to recover after reaching the nadir point, no packets are expired because they were already interrupted. This is why we have not included packet expiration in our model. However, in the blue curve, which illustrates the case with no interruptions, the natural expiration of packets is not zero. This discrepancy results in some error in the case when $\eta_{\max} = 0$. In the other cases, the small error is attributed to quantization error.

Table 3.3: Accuracy of online estimation of Damping

η_{\max}	RMSE (mHz)	Estimation error (%)
0	1.1	-
0.33	0.6	12.4
0.67	0.6	5.5
1	0.5	-0.5

3.4 EXTENDING THE METHOD TO ARBITRARY REFERENCE SIGNALS

In the previous sections, a fully decentralized proportional controller to provide synthetic damping from a TCL fleet was presented. In this section, the results are extended to arbitrary reference signals. While the proposed control scheme is tested on a timer-based prioritization scheme [51], it can be applied to other *fitness-based*

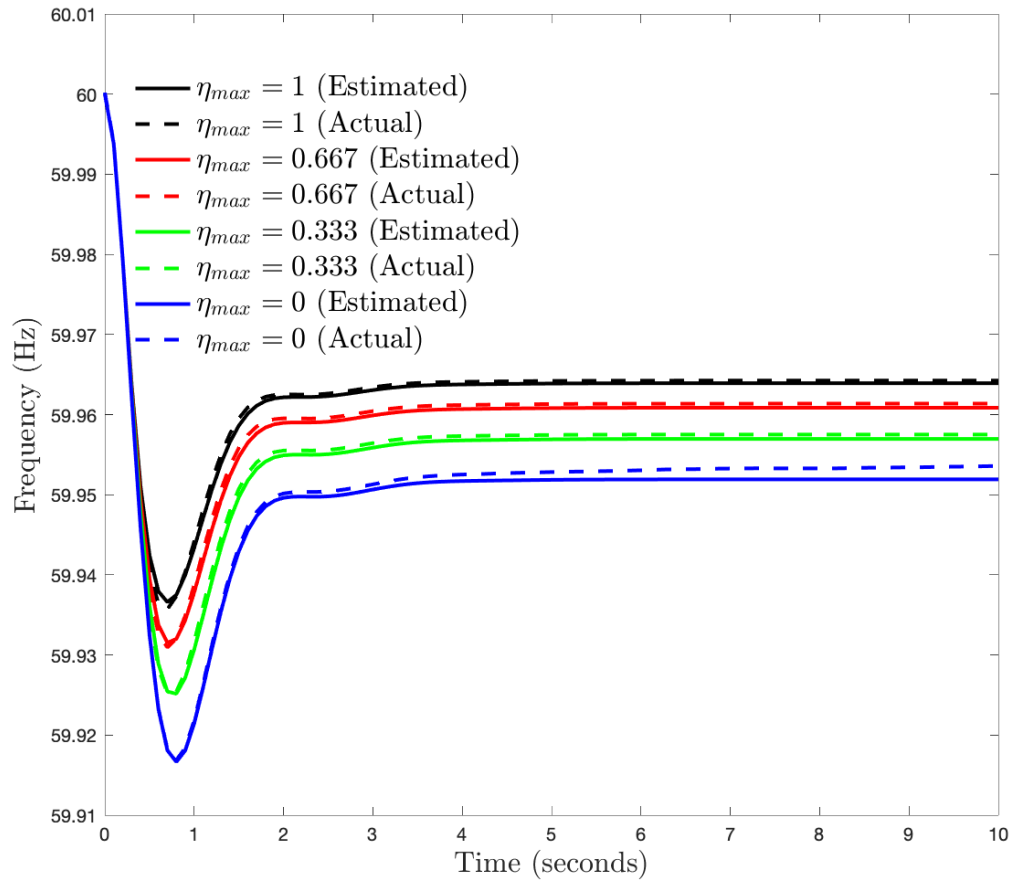


Figure 3.5: Estimation of frequency response for different values of η_{max}

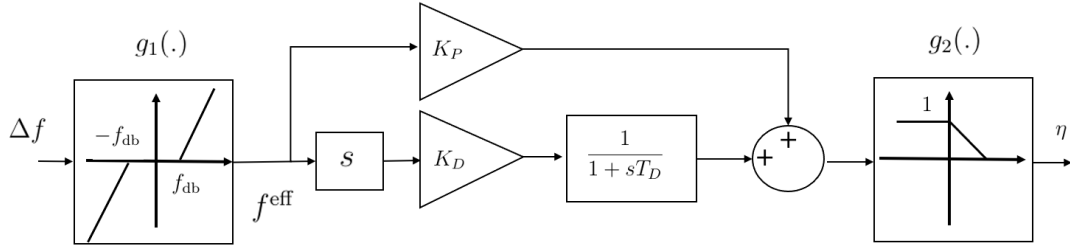


Figure 3.6: Block diagram of the proposed derivative-proportional control law. $g_1(\cdot)$ and $g_2(\cdot)$ are defined in (3.8)

DER prioritization schemes (e.g., [65]) as well. Each DER measures frequency locally and based on the designed control law, a frequency-dependent threshold on the timer is calculated. Based on the calculated threshold, devices determine whether to participate in primary frequency control or not. To the best of the author’s knowledge, this is the first work to provide an analytical estimate of the amount of synthetic damping that can be extracted from a DER fleet.

3.4.1 MODIFYING THE PROPOSED CONTROL LAW

The controller from (3.7) is modified to take into account the bi-directional DERs, as well as RoCoF. The designed controller creates additional damping from the DER fleet which is added to the conventional system damping, i.e., D_j in equation (2.1b). The overall layout of the proposed controller is shown in Fig. 5.16. A deadband with a size of f_{db} is defined such that if $|\Delta f[k]| < f_{db}$ DER does not respond to a frequency deviation. f_{db} is assumed 36 mHz to match a typical synchronous generator droop controller’s deadband. A fleet’s maximum participation is achieved at f_{max} when all of the active devices have participated in primary frequency control.

η_{\min} determines the portion of the timer that does not participate in FFR. In other words, devices will be locked for $\eta_{\min}\delta$ seconds after their request is accepted.

The proposed local control law is:

$$\eta_n[k] = \begin{cases} 1, & |\Delta f[k]| < f_{\text{db}} \\ g_2 \left(K_P f^{\text{eff}}[k] + K_D \mathcal{D}(f^{\text{eff}}[k]) \right), & f_{\text{db}} \leq |\Delta f[k]| \leq f_{\text{max}}, \\ \eta_{\min} & |\Delta f[k]| > f_{\text{max}} \end{cases} \quad (3.7)$$

where $K_P = 1/(f_{\text{max}} - f_{\text{db}})$ and K_D are the design parameters representing proportional and derivative gains, respectively, and T_D is the derivative time constant. The derivative in the Laplace domain is denoted by s . $f^{\text{eff}}[k] := g_1(\Delta f[k])$ with $\Delta f[k]$ the deviation from nominal frequency (e.g., 60 Hz) and functions

$$g_1(x) := \begin{cases} 0, & |x| \leq f_{\text{db}} \\ |x| - f_{\text{db}}, & f_{\text{db}} \leq |x| \leq f_{\text{max}} \end{cases}, \quad (3.8)$$

$$g_2(x) := \min\{\max\{-|x| + 1, \eta_{\min}\}, 1\}.$$

Note that $\mathcal{D}(f)$ is the backward discrete-time difference operator as expressed in (3.9). It estimates the rate of change of frequency (RoCoF) over the standard 500 ms window [66].

$$\mathcal{D}(f[k]) = \frac{f[k] - f[k - \alpha_w/\Delta t_s]}{\alpha_w} \quad (3.9)$$

where α_w is the window size in [sec]. Thus, each device calculates its η_n based on the locally measured frequency and participates in the frequency response, if $t_n[k]/\delta \geq$

$\eta_n[k]$ for charging packets and $-t_n[k]/\delta \geq \eta_n[k]$ for discharging packets. Immediately after a typical frequency event, the frequency deviation is zero while the magnitude of RoCoF is largest (i.e., $\mathcal{D}(f^{\text{eff}})$ is a monotonic function and $\mathcal{D}(f^{\text{eff}})$ approaches 0 exponentially). Therefore, the aggregate power response is initially due to the differential term $K_d\mathcal{D}(f^{\text{eff}})$ in (3.7). However, since $\mathcal{D}(f^{\text{eff}}) \rightarrow 0$ exponentially (top plot in Fig. 3.7), the proportional term $K_p f^{\text{eff}}$ becomes dominant, resulting in a linear decrease in aggregate power with respect to the frequency deviation. Finally, after the frequency reaches its nadir point and starts to recover, no more DERs participate, as shown in the bottom plot of Fig. 3.7. As illustrated in Fig. 3.7, the local control law can effectively coordinate packet participation at scale to improve the frequency response with higher K_D values leading to more responsive (and aggressive) DER participation. Some remarks on controller tuning are presented in Subsection 3.5.4. The next subsection makes use of the timer definition and the proposed control law to determine the available synthetic damping in real-time.

3.4.2 REAL-TIME ESTIMATION OF DAMPING

Since the coordinator determines how many devices are accepted during each time step and the packet height, i.e., P_n^{rate} is known for any packet request, $x_{\text{tcl}}^{\text{ch}}[k]$, $x_{\text{ess}}^{\text{ch}}[k]$, and $x_{\text{ess}}^{\text{dis}}[k]$ can be accurately estimated by the coordinator in (effectively) real-time. Furthermore, to overcome any inaccuracies associated with the communication or actuation delays, the coordinator can use feedback in the form of a simple acknowledgment sent (asynchronously) from each device when its operating state transitions. In addition, the frequency of the system can be measured by the coordinator, and from (3.7), a single $\eta[k]$ can be calculated for the entire fleet in real time. Moreover,

given that the number of ON devices in each timer bin is known, the coordinator can then determine the available load reduction in response to frequency deviation without the need for additional communication with devices. For example, (3.10) determines the amount of available power for an under-frequency event.

$$\begin{aligned} \Delta P^{\text{DER}}[k] = \sum_{i=1}^{\tilde{K}} & \left(x_{\text{icl}}^{\text{ch}}[k - \delta/\Delta t + i - 1] \right. \\ & \left. + 2x_{\text{ess}}^{\text{ch}}[k - \delta/\Delta t + i - 1] \right), \end{aligned} \quad (3.10)$$

where $\tilde{K} := \lfloor \eta[k]\delta/\Delta t \rfloor$. Thus, from the aggregate fleet power and any potential system frequency event (i.e., a deviation with nadir Δf_{nadir}), the coordinator can simply and, in real-time, estimate the available synthetic damping from a DER fleet as

$$D^{\text{syn}}[k] = \frac{\Delta P^{\text{DER}}[k]}{\Delta f_{\text{nadir}} - f_{\text{db}}}. \quad (3.11)$$

As seen in Fig. 3.7, after reaching the nadir frequency, the frequency begins to recover, which results in an increase in $\eta_n[k]$ according to (3.7). However, it is important to highlight that even as $\eta_n[k]$ increases, DERs that have already been interrupted will not switch back on again. That is, the drop in load is sustained. Therefore, the amount of damping added from the fleet of DERs is determined by the nadir frequency, as described in (3.11). Fig. 3.8 illustrates the accuracy of the synthetic damping estimate compared with actual damping provided by the DER fleet for 10 different frequency events. The top figure shows the change in power versus the change in frequency for one of these realizations.

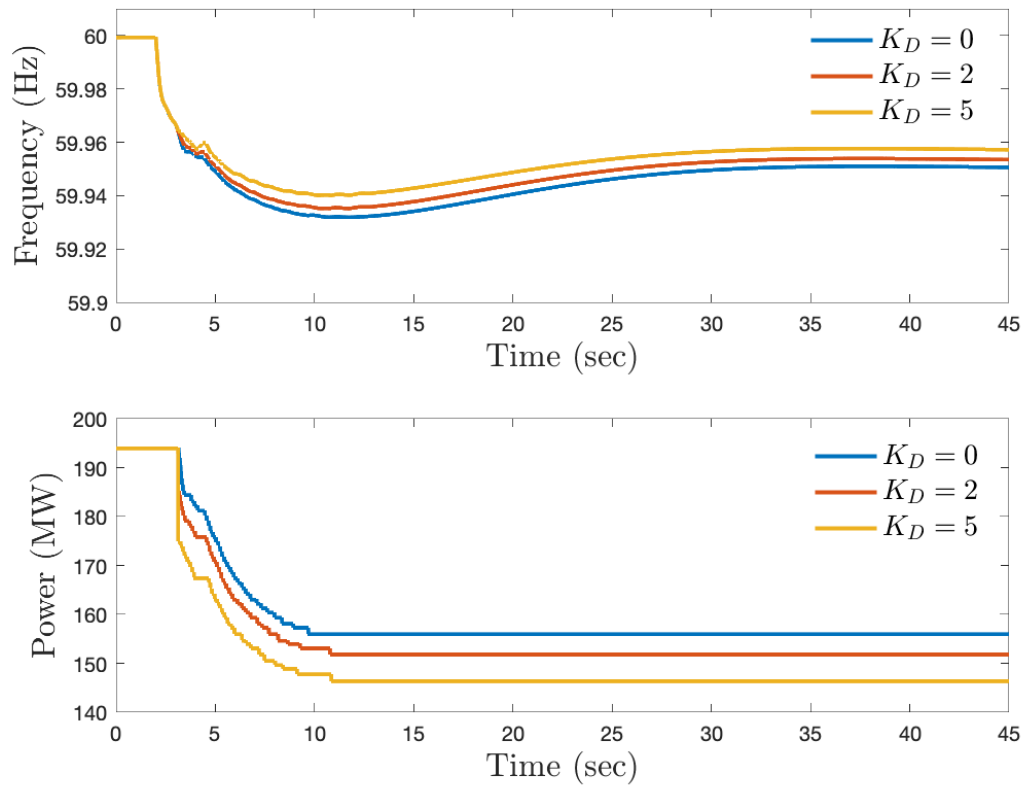


Figure 3.7: Frequency response of 200,000 TCLs for different values of K_D .

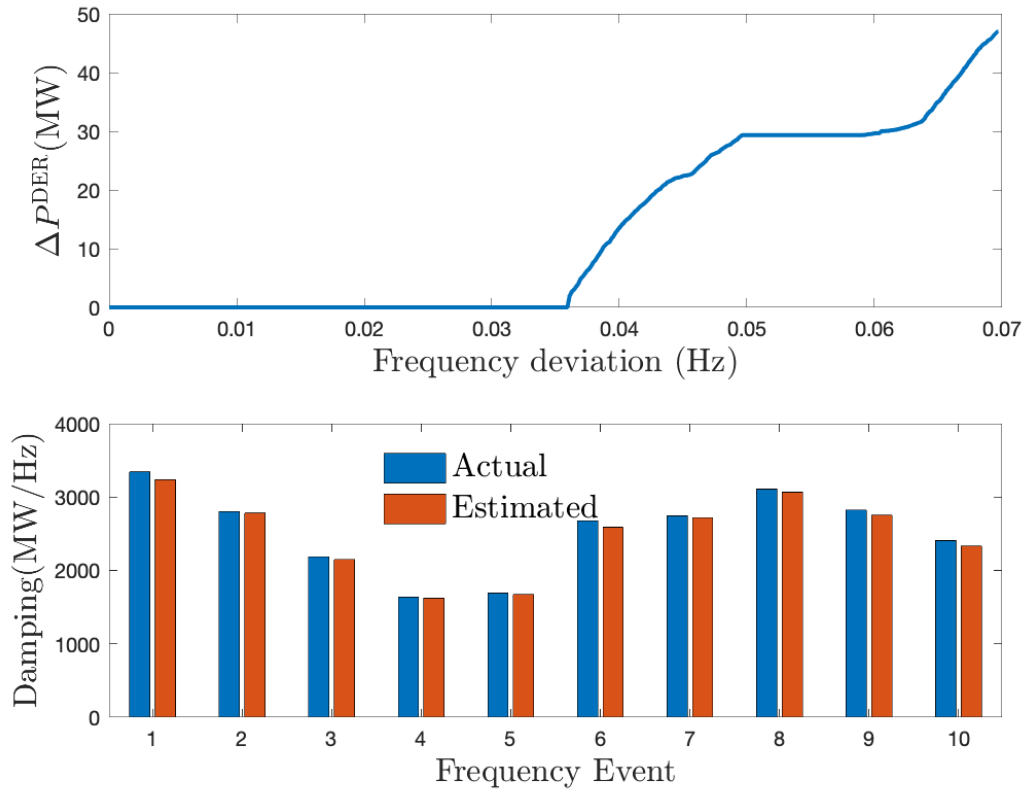


Figure 3.8: (Top) A single frequency event with $\Delta f_{nadir} = 0.07\text{Hz}$ yields a large load reduction in the aggregate DER fleet as a function of the frequency deviation, packet timer distribution, and designed control law. (Bottom) Comparing the actual damping with the real-time estimate of synthetic damping for 10 different frequency events.

Calculation time to find synthetic damping for a fleet of 200,000 DERs from Eq. (3.7), (3.10) and (3.11) takes less than 500 μs which is acceptable for real-time applications. This allows the coordinator to accurately and continuously estimate the available synthetic damping across a number of what-if scenarios (e.g., different frequency nadir and RoCoF pairs). Clearly, 100s of these calculations could be executed every 60 seconds to provide the coordinator/ISO with an accurate and real-time estimate of available synthetic damping capability from a fleet of DERs. The ISOs could then use these data/capabilities to evaluate stability margins/contingencies/ancillary services needs/etc.

While secondary frequency control services markets have been well-established across the world, markets explicitly designed for Fast Frequency Response services are relatively rare. This scarcity can be attributed to certain factors, such as traditional generators being inherently equipped with governors capable of providing FFR, and large interconnected power systems typically having surplus FFR capacity thanks to synchronous generators. Nevertheless, as the penetration of renewable generation increases in power systems, these conventional conditions may no longer hold true. Notably, in the existing landscape, New Zealand has already implemented a market design for FFR, known as "instantaneous reserve," while the Australian Energy Market Commission (AEMC) is poised to enact a rule for a similar market from the year 2025 onward. These developments calls for more emphasis on developing strategies for participants in the potential FFR markets.

In this section, a method is provided for the coordinator to accurately estimate the synthetic damping available from a fleet of DERs in any real-time operating condition (i.e., with an arbitrary, but known timer distribution). However, the coordinator may

want to know a day- or hour ahead how much synthetic damping will be available from the fleet, in which case the timer distribution is unknown. Thus, in the next section, a probabilistic prediction of the available synthetic damping from a fleet of DERs participating in frequency regulation (e.g., PJM’s Reg-D) is developed that captures a range of operating conditions via the amplitude of the Reg-D regulation signal. The method in [54] is generalized to a bidirectional fleet by leveraging a specific packet-acceptance policy from [67] to ensure a unique mapping between the reference signal and the power-timer distribution. This enables an analytical characterization of synthetic damping statistics. It also can toggle the load between charging and discharging modes which double the synthetic damping available. Consequently, this permits us to analyze the trade-off between expected primary (damping) and secondary frequency control capabilities and (statistically) guarantee a DER fleet’s ability to deliver synthetic damping.

3.5 CHARACTERIZING THE AVAILABLE SYNTHETIC DAMPING

Here, a probabilistic framework incorporating historical AGC data is used to characterize the available synthetic damping that can be guaranteed (i.e., a lower bound) from a fleet of DERs that are coordinated via ON/Charge/Discharge packets and providing a certain MW-level of frequency regulation (AGC) services. The process of mapping a representative AGC signal from the fleet’s timer distribution to the change in the fleet’s aggregate power due to a frequency event is outlined next. It is based on a spectral decomposition of historical AGC (PJM Reg-D) data and was inspired

by [68, 69].

To map timer states to changes in power, ΔP^{DER} , for a given frequency event, the (conveniently) designed frequency-dependent timer threshold, η is leveraged.

Remark. *The minimization policy, as presented in [67], aims to track the reference signal with the fewest number of DERs. This policy guarantees that the number of DERs in the timer is always lower compared to other control policies. Consequently, it establishes a lower limit on the flexibility (i.e., synthetic damping) achievable for a given fleet.*

However, the shape of the timer distribution is unknown in advance as it depends on the fleet’s operating conditions (i.e., the reference signal and the number of available packet requests). Under the assumptions that (A1) a sufficient number of packet requests are available to the DER coordinator for effective aggregate power reference tracking (i.e., negligible tracking error); (A2) a fixed packet-request-acceptance policy (e.g, minimize the number of accepted packets) is adopted [67]; and (A3) the power reference signal is known ahead of time, then the exact timer distribution can be constructed over the duration of a packet epoch and the available synthetic damping can be estimated. However, if the coordinator wants to *predict* the available synthetic damping ahead of time (e.g., for possible FFR markets or planning studies), the exact AGC power reference will be unknown (i.e., assumption A3 will not hold), which implies that the timer distribution will be unknown. To overcome this challenge, historical AGC data is used to characterize the statistics of the timer distribution and thus to provide a probabilistic lower bound on the synthetic damping availability. Hence, the methodology for characterizing the synthetic damping availability from a fleet of DERs consists of the following steps:

1. Decompose historical AGC signals into its N most salient harmonics.
2. From the spectral decomposition and under assumptions A1 and A2, determine the statistics of the corresponding timer distribution.
3. Using the timer distribution statistics, determine a probabilistic lower bound on the number of packets in each timer.
4. Compute the probabilistic lower bound on the available synthetic damping from the fleet.

3.5.1 SPECTRAL DECOMPOSITION OF AGC DATA

Following [69], where a clustering technique is able to categorize similar 2-hour samples of historical AGC data based on spectral analysis, a 2-hour AGC sample is considered. That is, the *methodology* is representative of a historical 2-hour AGC signal. However, the methodology can readily be applied to larger AGC data sets via methods presented in [69].

Consider the spectral (Fourier-based) decomposition of a 2-hour-long historical AGC sample signal of 2-second resolution into its N most salient harmonics as

$$AGC[k] \approx A \sum_{h=1}^N H_h[k], \quad (3.12)$$

where $H_h[k] := c_h \cos(2\pi h f_0 k - \phi_h)$. The coefficient c_h for the h -th harmonic is scaled between 1 and -1, while phase shift is denoted by ϕ_h , and f_0 is the signal's fundamental frequency. A is the amplitude of the reference signal in MW. The reference signal is then defined as $P^{\text{ref}}[k] = P^{\text{nom}} + AGC[k]$ where P^{nom} is the power set-point that

maintains the average SoC of the fleet stationary and $AGC[k]$ is obtained from (3.12). The goal is to map P^{ref} to the coordinator's timer distribution (under assumptions A1 and A2). The procedure is detailed next for under-frequency events. The derivation for over-frequency events follows similarly. An expression for the total power of accepted requests at time k for each harmonic h , $q_h^+[k]$, must be found first. $q_h^+[k]$ determines the power in the first bin of the timer at time k for harmonic h . This is then used to find $q^+[k]$ which is the total number of accepted requests at time k .

It is convenient to decompose H_h into two functions an increasing function ($Y_h[k]$) and a decreasing function ($Z_h[k]$). That is, $H_h[k] := Y_h[k] - Z_h[k]$, where

$$Y_h[k] = \begin{cases} H_h[k], & \text{if } H_h[k] - H_h[k-1] > 0 \\ 0, & \text{otherwise} \end{cases} \quad (3.13a)$$

$$Z_h[k] = \begin{cases} -H_h[k], & \text{if } H_h[k] - H_h[k-1] < 0 \\ 0, & \text{otherwise} \end{cases}. \quad (3.13b)$$

Under assumption A1, $Y_h[k] - Y_h[k-1]$ and $Z_h[k] - Z_h[k-1]$ define, respectively, the net increase and decrease in DER aggregate power reference signal at each time step k . Now, if enough packet requests are assumed available, the coordinator can accept enough of them to match this increase or decrease. Thus, at each k , each of the reference signal's harmonics can be matched with enough number of accepted packet requests entering the coordinator's timer. Note that when the fleet includes both charging and discharging requests, the mapping becomes non-unique (since charging and discharging packets can effectively *cancel* each other out). To ensure a unique mapping between (harmonic) reference signals and accepted requests, a minimizing

packet accepting the policy at the coordinator is employed that essentially does not select both charging and discharging requests at the same time [67].

Thus, under assumptions A1 and A2, $q_h^+[k]$ is written as,

$$\begin{aligned} q_h^+[k] = & \\ & (f(Y_h[k] - Y_h[k - 1]) - f(Z_h[k - n_p] - Z_h[k - 1 - n_p])) \\ & + (f(Y_h[k - n_p] - Y_h[k - 1 - n_p])), \end{aligned} \quad (3.14)$$

where $f(x) = x$ for $x \geq 0$ and $f(x) = 0$, otherwise. In (3.14), $f(Y_h[k] - Y_h[k - 1])$ determines the increase in the reference signal while the second and third terms determine the number of expired discharging and charging packets, respectively.

The next theorem characterizes the statistics of the charging timer for the minimization policy.

Theorem 2. *Let δ , Δf , P^{cap} , and n_p , η_{min} , f_{max} , f_{db} and K_D be fixed for a given fleet under decentralized control policy (3.7). The mean and standard deviation of q^+ are given by:*

$$\mathbb{E}(q^+) = n_u + \frac{N_d A \sum_{h=1}^N h c_h \Delta t}{T}, \quad (3.15)$$

$$\sigma^2(q^+) = \sum_{h=1}^N \left(\frac{1 - e^{-\frac{T^2}{6h^2}}}{2} (2\pi \Delta t f_h A c_h)^2 + \frac{2N_d A^2 h c_h^2 \Delta t}{T} \right), \quad (3.16)$$

where $n_u = P^{nom}/(n_p)$, $N_d = 2$ for ESS fleet and $N_d = 0$ for TCL fleet.

Proof. The proof is done by construction. The properties of Y_h and Z_h are utilized to simplify (3.14) and find the mean and standard deviation. From (3.13a) and (3.13b)

and the definition of f , it can be seen that

$$f(Y_h[k] - Y_h[k - 1]) = \begin{cases} 0, & k \in \frac{iT}{2} \quad i = \pm 1, \pm 2, \dots \\ Y_h[k] - Y_h[k - 1], & \text{otherwise} \end{cases} \quad (3.17)$$

In the case of the ESS fleet, the above equation implies that there are two discontinuities in $f(Y_h[k] - Y_h[k - 1])$ during a period. That is $N_d = 2$. In the case of a TCL fleet, since there are no discharging requests, $Z_h[k] = 0$, and $H_h[k] = Y_h[k]$, which leads to $N_d = 0$. Note also that $Y_h[k] - Y_h[k - 1] = 0$ when $Y_h[k] = 0$ and in any other case

$$\begin{aligned} Y_h[k] - Y_h[k - 1] &= A c_h \cos(2\pi f_h k \Delta t) - A c_h \cos(2\pi f_h (k - 1) \Delta t) \\ &\approx -2\pi f_h A c_h \Delta t \sin(2\pi f_h k \Delta t), \end{aligned} \quad (3.18)$$

where $\omega_h = 2\pi f_h$.

Using (3.17) and (3.18), one can find the mean and variance of q_h^+ directly from the mean and variance of $\sin(2\pi f_h k \Delta t)$, where $k \sim \mathcal{U}(0, 1/f_h)$ represents the random time of failure.

The interest here is to find the mean and variance of $f(Y_h[k] - Y_h[k - 1])$, which can be obtained using the corresponding mean and variance of $Y_h[k] - Y_h[k - 1]$ given that these expressions only differ by N_d over each period. Recalling that for a set X_1, X_2, \dots, X_N of mutually independent normal random variables with corresponding

means $\mu_1, \mu_2, \dots, \mu_N$ and variances $\sigma_1^2, \sigma_2^2, \dots, \sigma_N^2$ one has that

$$Y = \sum_{h=1}^N c_h X_h \sim \mathcal{N} \left(\sum_{h=1}^N c_h \mu_h, \sum_{h=1}^N c_h^2 \sigma_h^2 \right), \quad (3.19)$$

and assuming that the dependence between harmonics of the AGC decomposition is negligible, then the mean and variance of the timer variable q^+ can be obtained by adding the mean and variance of each harmonic. In addition, the expected value of the power of the accepted requests corresponding to tracking P^{nom} is $n_u = P^{\text{nom}}/(n_p)$ [54]. Therefore, using (3.19), q^+ has a Gaussian distribution with mean and standard deviation given by (3.15) and (3.16). □

3.5.2 FINDING PROBABILISTIC LOWER BOUND ON AVAILABLE DAMPING

Theorem 2 is now used to compute a robust lower bound on the total power in each bin of the timer, P_{\min} , analytically as follows,

$$P_{\min} = \mathbb{E}(q^+) - F\sigma(q^+). \quad (3.20)$$

where F is a *safety factor* determined by the operator. P_{\min} estimates, at each time step, the minimum power inside the timer. We use P_{\min} to compute minimum available damping. The following example is used to illustrate how P_{\min} is computed:

Example 1. *Let us assume our distribution has 5 bins. The coordinator accepts 3, 4.5 kW packets and 2, 5 kW packets at $k - 4$. It accepts 2, 5 kW packets at $k - 3$. It*

accepts 4, 4.5 kW packets at $k - 2$. It accepts 4, 6 kW packets at $k - 1$ and 2, 4.5 kW packets and 3, 3 kW packets at k . The power in each bin of the timer at k , is 18 kW, 24 kW, 18 kW, 10 kW, and 23.5 kW in bins 1 to 5, respectively. For simplicity, assume that there have been no ON packets in the beginning. In this case, P_{min} is 10 kW, which is the minimum power across the bins. This is illustrated in Fig. 3.9.

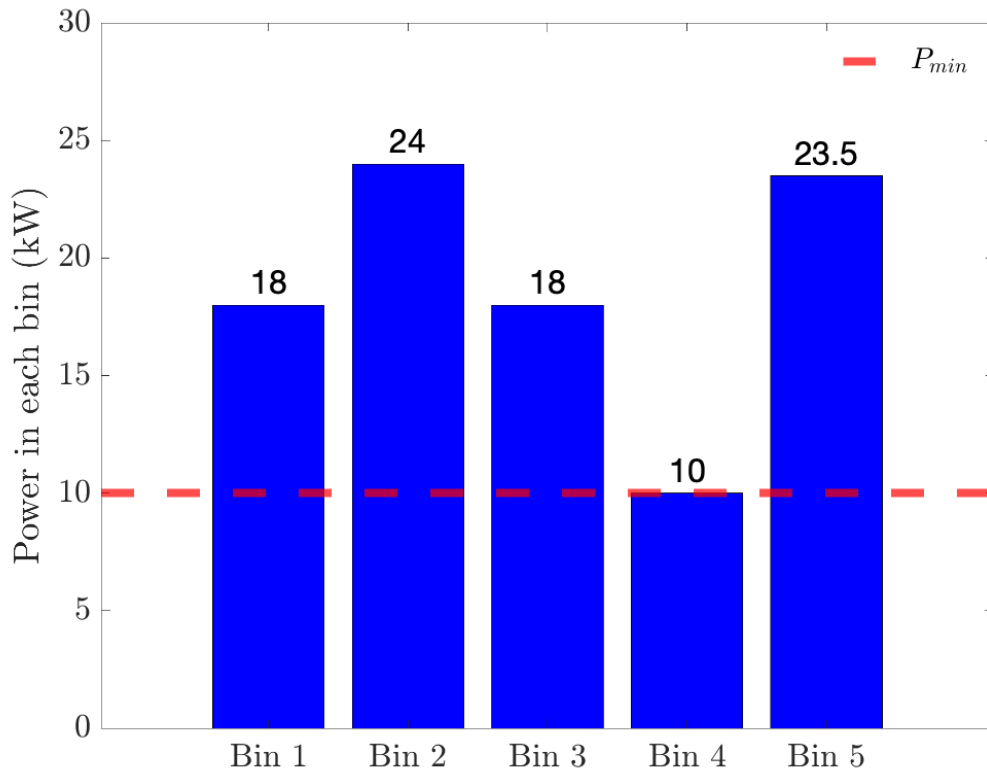


Figure 3.9: Illustrative example for computation of P_{min}

Higher F leads to a more robust estimate but at the same time results in a more conservative estimate of the fleet's available damping. F is usually defined by the information available on the underlying distribution of the uncertainty, e.g., distribution, statistics, etc. If more information is available about the distribution

of uncertainty, less conservative estimation can be made. The probability of being within F standard deviations is defined as $\rho := P(q^+[k] > \mathbb{E}(q^+) - F\sigma(q^+))$. If no information about the distribution of P_{\min} is available (only mean and standard deviation are known), then using the Borel-Cantelli inequality [70], F is

$$F = \left(\frac{1 - \rho}{\rho} \right)^{\frac{1}{2}}. \quad (3.21)$$

The bounds obtained by Borel-Cantelli inequality are the worst-case scenarios and are unlikely to be encountered in practice. By assuming that there exists evidence that the distribution is unimodal, the Chebyshev generating function (CGF) can be used as shown below

$$F = \left(\frac{1 - \rho}{e\rho} \right)^{\frac{1}{1.95}}. \quad (3.22)$$

[71]. Furthermore, if the distribution is Gaussian, the safety factor is found as follows:

$$F = \sqrt{2} \operatorname{erf}^{-1}(1 - 2\rho). \quad (3.23)$$

where ρ is the probability of violation of the lower bound on P_{\min} calculated by (3.20) and illustrates the proportion of cases with violations. By choosing the desired level for ρ and based on the level of information available to the coordinator, F is selected from the above equations.

In [54] a method to calculate the synthetic damping for a uniform timer distribution was presented. By assuming that all of the timer bins are at P_{\min} , one can use the method described in [54], to calculate a constant value for lower-bound damping.

The next theorem is used to find the probabilistic lower bound on damping from P_{\min} .

Theorem 3. *Given Theorem 2, for a given contingency with known $\Delta f_{\text{nadir}} \in (f_{\text{db}}, f_{\text{max}})$ and RoCoF, the minimum damping for under-frequency events is,*

$$D^{\min} = n_p P_{\min}^{\text{eff}} \left(K_P + \frac{K_D R^{\text{max}}}{\Delta f_{\text{nadir}} - f_{\text{db}}} \right). \quad (3.24)$$

where $P_{\min}^{\text{eff}} = P_{\min}$ for TCLs and $P_{\min}^{\text{eff}} = 2P_{\min}$ for ESS.

Proof. The proof is by construction. From (3.7), the total change in the fleet's aggregate power for a uniform distribution is:

$$\Delta P^{\text{DER}} = (1 - \eta_{\text{nadir}}) P_{\text{ON}}, \quad (3.25)$$

where η_{nadir} is the calculated η at nadir frequency. P_{ON} is the total power of ON devices and is calculated as $n_p P_{\min}$. In under-frequency events, charging devices participate in frequency response, and discharging devices do not participate. From control law in (3.7), and (3.25) and the damping definition [20], the estimated damping is $D^{\min} = \Delta P^{\text{DER}} / (\Delta f_{\text{nadir}} - f_{\text{db}})$, which leads to $n_p P_{\min} \left(K_P + \frac{K_D R^{\text{max}}}{\Delta f_{\text{nadir}} - f_{\text{db}}} \right)$ for $f_{\text{db}} \leq |\Delta f_{\text{nadir}}| \leq f_{\text{max}}$. As mentioned in 3.4.1, the magnitude of $\mathcal{D}(f^{\text{eff}}[k])$ is at its maximum at the beginning of the disturbance and it decreases exponentially. Therefore, it is possible to replace $\mathcal{D}(f^{\text{eff}}[k])$ with the known maximum RoCoF of the event, R^{max} . Since ESS charging devices can be toggled to discharge during the frequency event, they can provide twice their capacity. This is captured by $P_{\min}^{\text{eff}} = P_{\min}$ for TCLs and $P_{\min}^{\text{eff}} = 2P_{\min}$ for ESS. If the frequency deviation is less than f_{db} , damping is zero as indicated by (3.7). Finally, if frequency deviation exceeds f_{max} , all of the available power is shed, resulting in $D^{\min} = (P^{\text{cap}} n_p n_{\min}) / (\Delta f_{\text{nadir}} - f_{\text{db}})$. \square

Observe that from Eqs. (3.21), (3.22) or (3.23) the probability of violation of $P_{\min}(\rho)$ can be found based on the level of information available about the timer distribution. To relate ρ to the probability of violation of D^{\min} , the following remark is used.

Remark. *It is straightforward to show that the probability of violation of the calculated minimum damping in Theorem 3, is always smaller or equal to the probability of violation of $P_{\min}(\rho)$.*

Fig. 3.10 shows the estimated probability of violating the bounds for different information available versus the actual percentage of violations. 9 and 18 MW are chosen for A which are equal to 5% and 10% of the nominal power. The green and blue curves show the percentage of violations obtained in simulations whereas the blue, red, and yellow dashed lines are obtained from Eqs. (3.21), (3.22) and (3.23), respectively.

Remark. *It should be noted that the lower bound on damping is derived under the assumption of negligible tracking error. Based on the previous work, an epoch length of 3 minutes or less satisfies this assumption [72]. For higher amplitudes of AGC, the tracking error increases since the reference signal has higher fluctuations around the nominal power. Therefore, for higher AGC amplitudes, because of the higher tracking error, the probability of violation of the calculated bounds is higher. This can be seen in Fig. 3.10 by comparing the violation probabilities for A being 5% and 10% of the nominal power.*

Fig. 3.11 shows the accuracy of the estimated damping versus the true damping for different amplitudes of AGC. A fleet of 200,000 EWHs with 4.5 kW capacity each

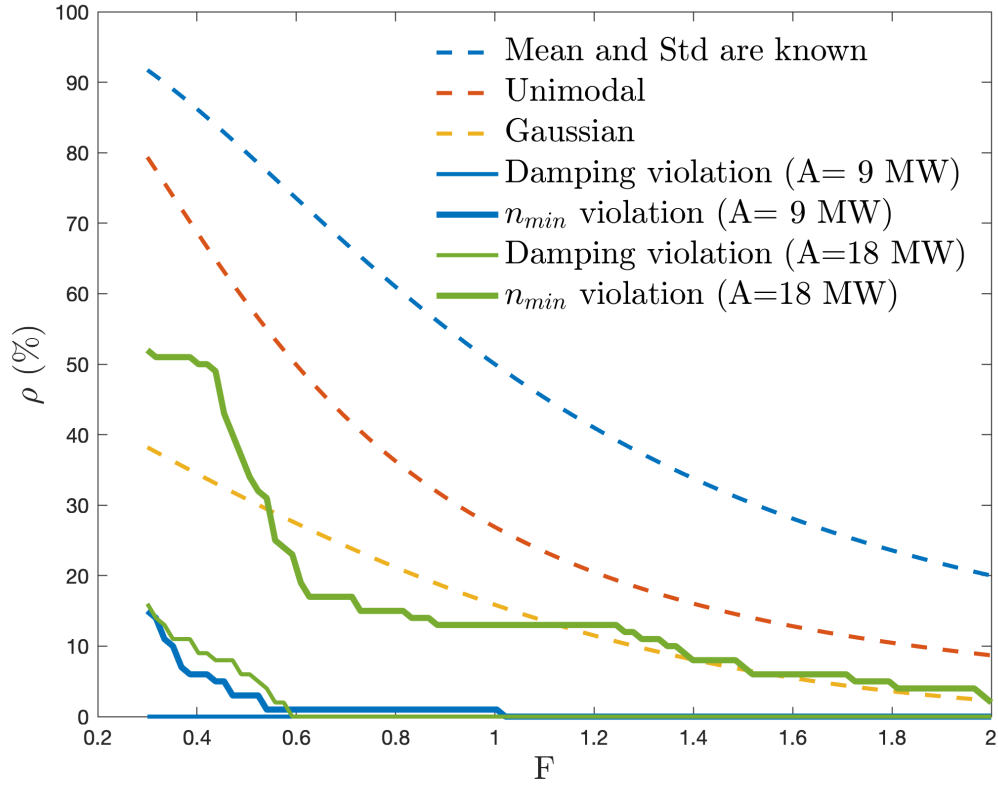


Figure 3.10: Probability of violating the bounds

is used in a two-area power system. The blue curve shows the mean of the true damping for 100 different realizations, while the green and purple curves show the mean minus 1 and 2 standard deviations, respectively. The dashed line indicates the estimated lower bound on damping calculated by (3.24). Similar results are given for an ESS fleet in Fig. 3.12 when $K_D = 5$. It should be noted that for each fleet, the reference signal is scaled around the fleet's nominal power. Therefore, the reference signal used to generate figures 3.11 and 3.12 is different which leads to a difference in the provided damping as seen in the figures.

To find the number of harmonics (N) required to reconstruct the AGC signal a

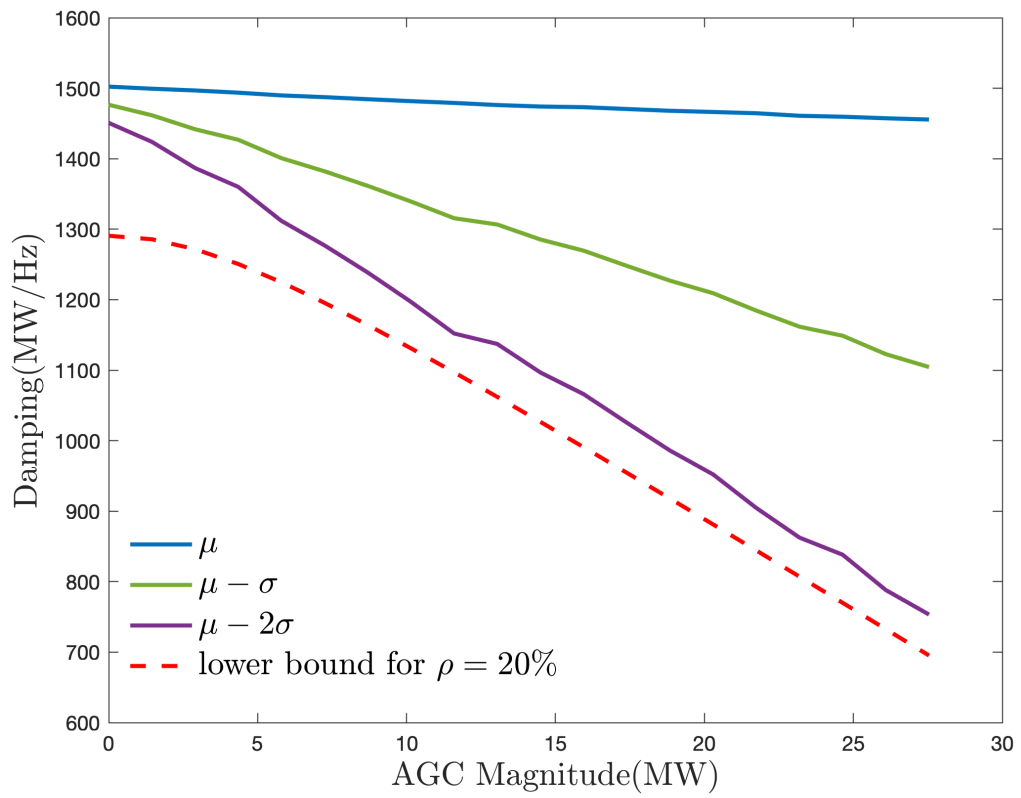


Figure 3.11: The actual vs estimate damping lower bound for 200,000 TCLs

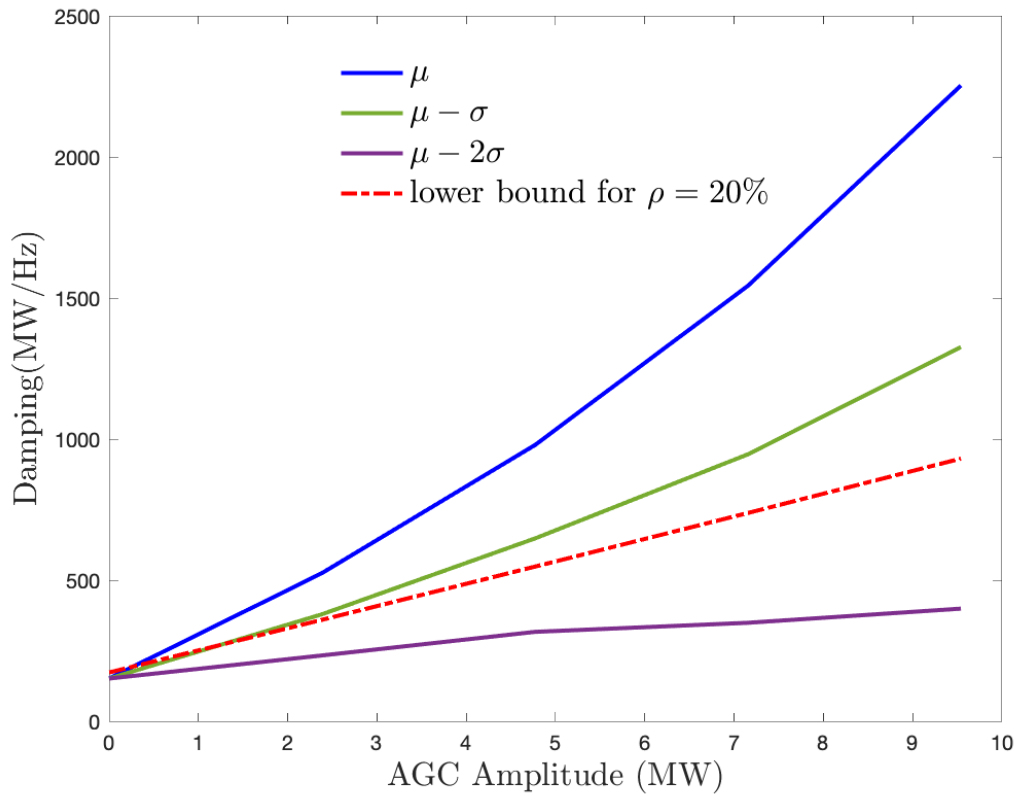


Figure 3.12: The actual vs estimate damping lower bound for 200,000 batteries

compromise between computation burden and accuracy must be taken into account. The goal is to find a N that gives an acceptable reconstruction error for all of the 1-hour samples of the AGC data. To do so, the reconstruction error is calculated for all of the 1-hour samples in one year. The simulation results show that for $N = 23, 35, 53$ the RMSE of reconstruction error is always lower than 30%, 20%, and 10%, respectively. Therefore, by choosing $N = 53$, it can be guaranteed that the reconstruction error for any day of the year is lower than 10%. In this work, $N = 100$ is chosen which limits the construction error for any given day to 6%.

3.5.3 FFR VERSUS FREQUENCY REGULATION TRADE-OFF

From Theorem 2, (3.20) and (3.24), it can be seen that tracking a larger AGC signal (larger A) leads to higher variance. This always translates to lower n_{\min} and D^{\min} for TCL fleet. For the ESS fleet, since $\mathbb{E}(q^+)$ is a function of A , as mentioned in Theorem 2, higher A does not necessarily lead to lower synthetic damping. In this section, a procedure to determine the proper A , for a TCL fleet is presented to maximize the total profit. The same procedure can be applied to the ESS fleet, as well.

If the prices of frequency regulation is β^{Reg} [\$/MW] and FFR damping is β^{FFR} [\$/MW/Hz], then the total revenue can be written as $\beta^{\text{Reg}}A + \beta^{\text{FFR}}D^{\min}$. If one defines $O := A\beta + D^{\min}$, where $\beta := \beta^{\text{Reg}}/\beta^{\text{FFR}}$, then it is straightforward to show that maximizing O maximizes the total revenue. By replacing (3.15) and (3.16)

in (3.20), one gets

$$P_{\min} = n_u - 2F\pi\Delta t f_0 A \sqrt{\sum_{h=1}^N h^2 c_h^2 \left(\frac{1 - e^{-\frac{T^2}{6h^2}}}{2} \right)} \quad (3.26)$$

Now, substituting (3.26) in (3.24) gives

$$O = A\beta + n_p \left(n_u - 2F\pi\Delta t f_0 A \sqrt{\sum_{h=1}^N h^2 c_h^2 \frac{1 - e^{-\frac{T^2}{6h^2}}}{2}} \right) \cdot \left(K_P + \frac{K_D R^{\max}}{\Delta f_{nadir} - f_{db}} \right). \quad (3.27)$$

To maximize O in (3.27), the derivative with respect to A is calculated as $\frac{\partial O}{\partial A} = \beta - \beta^{\text{thr}}$, where

$$\beta^{\text{thr}} = n_p 2F\pi\Delta t f_0 \sqrt{\sum_{h=1}^N h^2 c_h^2 \frac{1 - e^{-\frac{T^2}{6h^2}}}{2}} \left(K_P + \frac{K_D R^{\max}}{\Delta f_{nadir} - f_{db}} \right). \quad (3.28)$$

From (3.28), it can be seen that β^{thr} is a function of frequency events. Then, for a set of credible system contingencies $\{\mathcal{C}_1, \dots, \mathcal{C}_{N_c}\} \in \mathcal{C}$, with known $\Delta f_{nadir,c}$, R_c^{\max} and probability w_c , $\beta_1^{\text{thr}}, \dots, \beta_{N_c}^{\text{thr}}$ can be calculated from (3.28). Finally, a weighted average for β^{thr} is calculated as follows:

$$\overline{\beta^{\text{thr}}} = \sum_{c=1}^{N_c} w_c \beta_c^{\text{thr}}. \quad (3.29)$$

The normalized revenue, $O[MW/Hz]$, is presented in Figure 3.13 for different β and A . Total revenue in dollars [\$] is obtained by $\beta^{\text{FFR}} O$. The following conclusions can be derived from (3.27), (3.28), and (3.29):

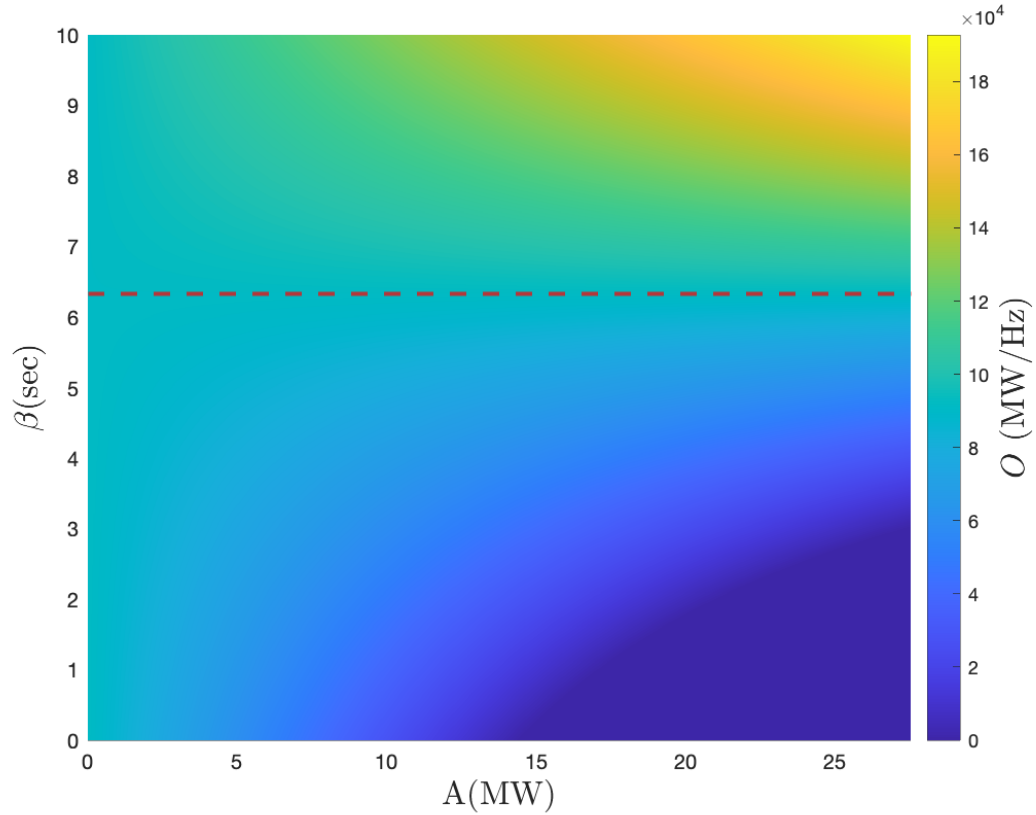


Figure 3.13: The impact of ancillary service prices on the total normalized revenue, O [MW/Hz]. The red line indicates β^{thr} above which larger AGC magnitudes, increase revenue.

1. If $\beta \geq \overline{\beta^{thr}}$, $\frac{\partial O}{\partial A} > 0$, which means that to maximize the profit, the largest possible value for A must be chosen, subjects to the fleet being able to track without a considerable increase in the tracking error.
2. If $\beta < \overline{\beta^{thr}}$, $A^{opt} = 0$.

In the proposed method, DERs are used in two modes. When the frequency is close to nominal (i.e., $|\Delta f[k]| < f_{db}$) the fleet tracks the AGC signal, and when frequency deviation exceeds f_{db} fleet goes to primary frequency control mode. Larger

AGC amplitudes mean that more resources are used for AGC tracking. It can be seen from Fig. 3.11 that for a TCL fleet, this leads to higher variation in damping which limits the ability to guarantee a minimum value for damping. Therefore, a fundamental trade-off between primary and secondary frequency control capability exists as seen in (3.26).

Another observation from (3.28) is that by using derivative control (i.e., increasing K_D), $\overline{\beta^{\text{thr}}}$ increases. This means that providing primary frequency control will be profitable for lower FFR prices (β^{FFR}).

3.5.4 TUNING OF THE CONTROLLER PARAMETERS

The coordinator is assumed to only have access to its own DER information and not that of the grid operators or other coordinators. As such, the tuning of K_P, K_D is based on the coordinator's fleet information and published system-wide reliability metrics, such as frequency nadir and RoCoF. For credible contingencies in the system, the initial post-contingency RoCoF (R^{max}) and nadir frequency are considered by the coordinator to characterize the network's frequency response and the DER fleet's available capacity to respond. It might be necessary to lock the devices for a certain time after turning them ON for reliability issues or to avoid excessive switching. This can be done by setting $\eta_{\text{min}} > 0$. Using the designed controller, the constraint on η_{min} leads to the following inequality:

$$\begin{aligned} \eta &= 1 - \frac{\Delta f_{\text{nadir}} - f_{\text{db}}}{f_{\text{max}} - f_{\text{db}}} - K_D R^{\text{max}} \geq \eta_{\text{min}} \\ \Rightarrow K_D &\leq \frac{1}{R^{\text{max}}} \left(1 - \frac{\Delta f_{\text{nadir}} - f_{\text{db}}}{f_{\text{max}} - f_{\text{db}}} - \eta_{\text{min}} \right). \end{aligned} \quad (3.30)$$

In addition to (3.30), the coordinator needs to design K_P and K_D with the corresponding minimum damping from (3.24) in mind relative to a desired predefined damping value.

To illustrate these results, η_{\min} and minimum damping are plotted versus K_D in Fig. 3.14 for the simulation setup of Fig. 3.7. For example, Fig. 3.14 depicts the relationship between η_{\min} , K_D and expected available damping. When $\eta_{\min} \leq 0.67$, then $K_D \leq 8.30$, which means that the expected available damping will be less than 4300 MW/Hz. The next section provides insight into practical considerations for packet-based DER coordination and primary frequency control via simulation-based analysis.

3.6 PRACTICAL CONSIDERATIONS

In this section, different practical considerations are tested to verify the performance of the proposed frequency-responsive controller for FFR. Different frequency measurement resolutions (between 1 mHz to 100 mHz) and random actuation delays (between 133 ms to 600 ms) are tested, and the effect on primary frequency control is analyzed. Moreover, simulation results are provided to determine how many DERs are needed to provide equal damping to an average droop-controlled generator in the network. The proposed decentralized controller is tested on the New England 39-bus system [73]. $K_D = 2$ unless otherwise specified. A generation outage of 250 MW occurs at bus 30 at $t = 2$ seconds. All of the DERs are connected to bus 20. The simulation setup is provided in table 3.4.

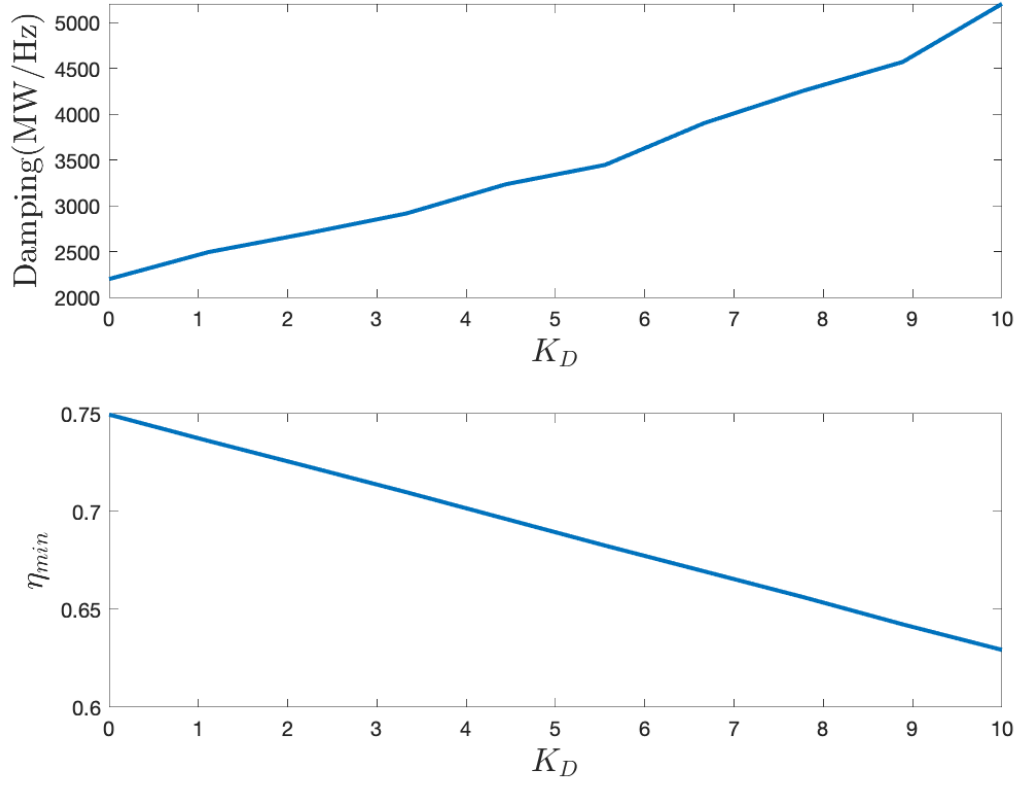


Figure 3.14: Unused timer and minimum damping for different values of K_D .

Table 3.4: Simulation Parameters

Parameter	Value
Fleet size	200,000
Δt	10 ms
$(\Delta f_{db}, \Delta f_{max})$	(36, 200) mHz
$T_n^{min/set/max}$	48.8/52.0/55.2 C°
$(\delta, MTTR)$	(3,3) mins

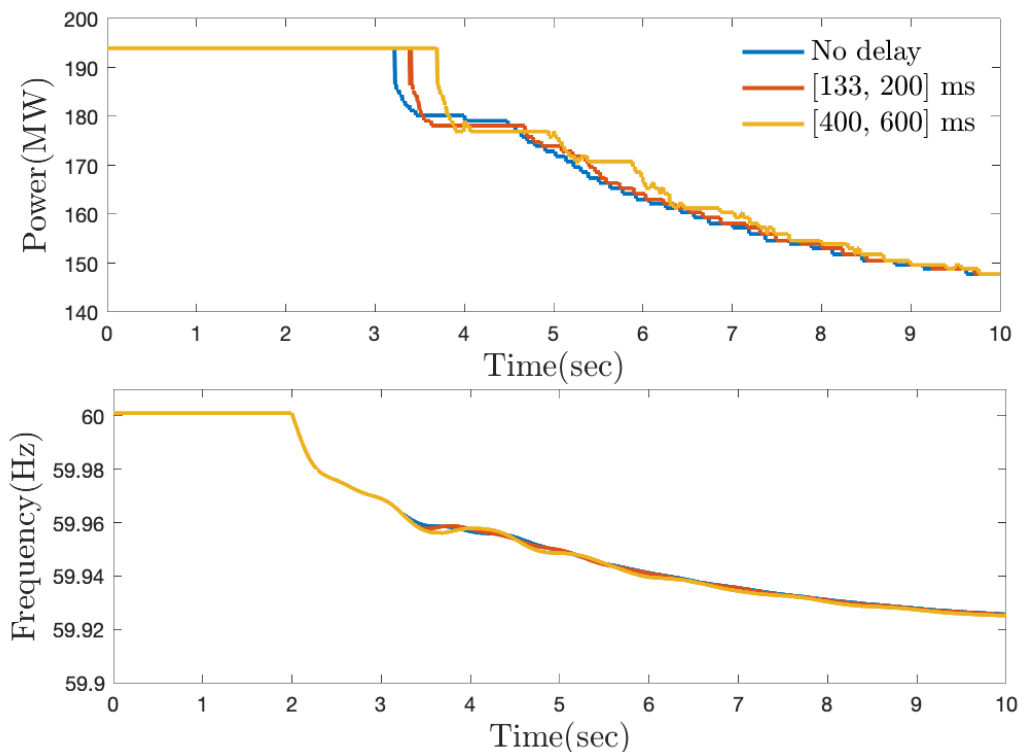


Figure 3.15: The frequency response for different actuation delays for a population of 200,000 DERs. The disturbance occurs at $t=2$ s.

3.6.1 ACTUATION DELAY

The effect of actuation delays is shown in Fig. 3.15. With no actuation delay, the fleet responds to frequency deviation immediately after frequency deviation exceeds f_{db} . While the delay slightly affects the transient behavior, the impact on final frequency (and damping) is negligible. The results illustrate the acceptable performance of the proposed approach even with a 400 to 600 ms delay which is the typical delay value in practice.

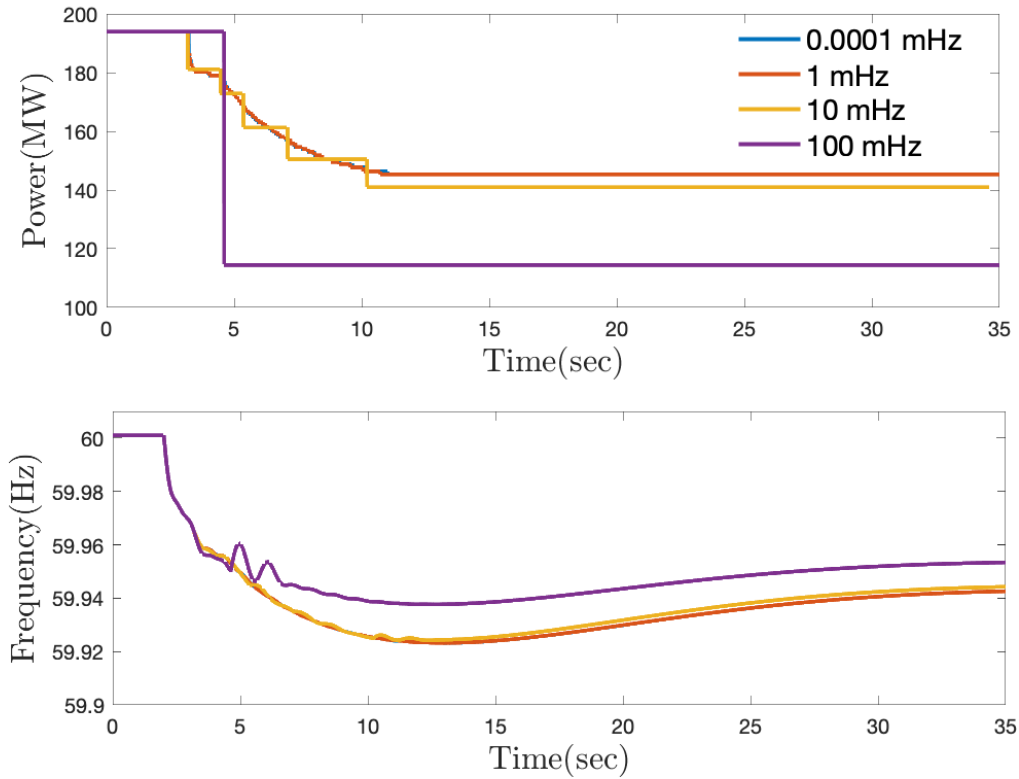


Figure 3.16: The frequency response for different frequency measurement resolutions for a population of 200,000 TCLs.

3.6.2 FREQUENCY MEASUREMENT RESOLUTION

Fig. 3.16 shows the impact of frequency measurement resolution on frequency response. The root mean square error (RMSE) of power interruption is 0.84 MW for 1 mHz resolution, 4.25 MW for 10 mHz resolution, and 34.78 MW for 100 mHz resolution. It can be seen that for 10 mHz frequency measurement resolution, the results are close to the actual values. Therefore, the effect of measurement inaccuracy can be neglected if the measuring devices' accuracy is at least 10 mHz.

3.6.3 RELATING THE SCALE OF AGGREGATE DER RESPONSE

When coordinating aggregations of DERs, it is of value to understand how many DERs are needed to replicate the synthetic available from a realistic power plant. To answer this question, an experiment is performed in which a generator in the IEEE 39-bus test system is tripped at bus 30, disconnecting 250 MW power. Then, the frequency at bus 39 is measured in two cases: *i*) 1000 MW Generator at bus 39 with 5% droop coefficient and no responsive loads *ii*) deactivate the droop control at bus 39 and replacing it with 80,000 EWHs, each of which has a 4.5 kW power rating. The simulation results are presented in Fig. 3.17. The yellow curve shows the frequency response at bus 39 without droop control and without DER coordination. The red curve shows the frequency response with 5% droop control at bus 39, and the blue curve shows the frequency response when the droop controller is replaced with 80,000 EWHs with 4.5 kW power. The results show that 80,000 coordinated EWHs can provide a droop-like fast frequency response equivalent to a 1000 MW generation unit with a 5% droop coefficient.

3.7 CONCLUSION

A fully decentralized frequency-based DER controller is designed and an analysis is presented that enables a DER aggregator to precisely estimate the synthetic damping available (online) from a fleet of aggregated DERs. To understand the impact of participating in ancillary services (i.e., frequency regulation) while also guaranteeing

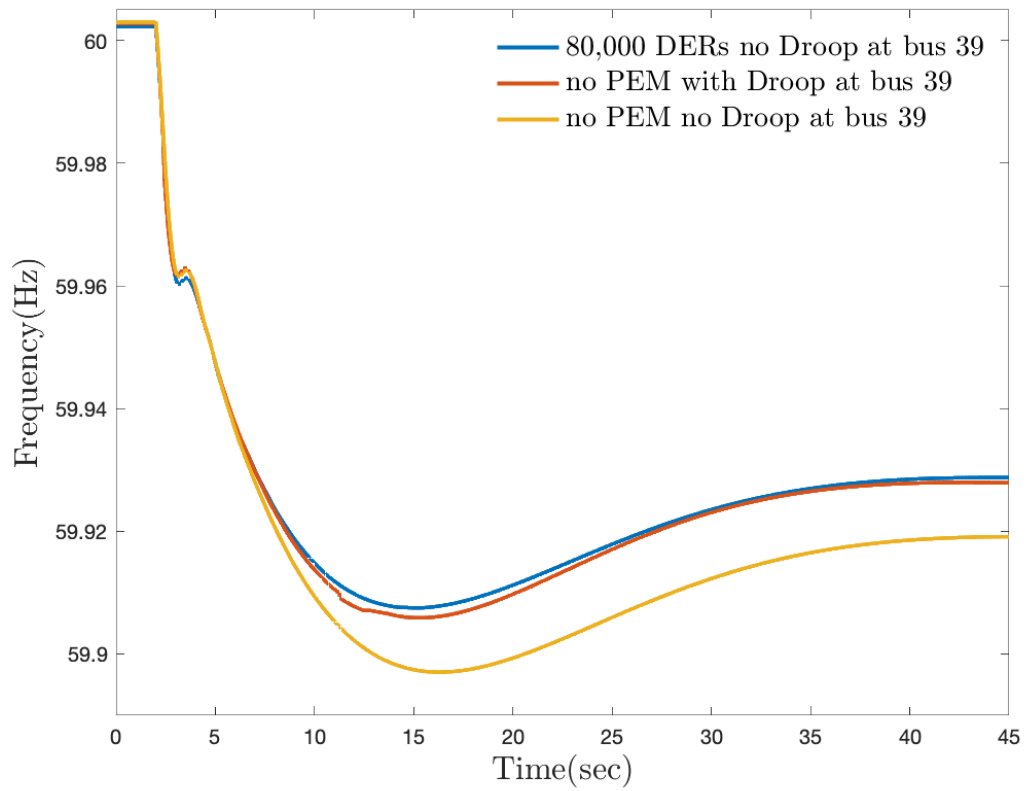


Figure 3.17: Frequency response, with/without droop control at bus 39 and with/without DER coordination.

available synthetic damping from the fleet, a comprehensive analysis is provided to characterize a probabilistic lower bound on the available synthetic damping. This bound enables trade-off analysis between the fleet's ability to provide frequency regulation versus synthetic damping. Finally, practical considerations of the proposed decentralized control scheme are presented in a simulation-based study concerning the effects of actuation delays and frequency measurement resolutions. Future research directions include adapting the decentralized controller parameters based on spatial grid information to differentiate and prioritize certain locations/buses/feeders, as a way to incorporate the proposed synthetic damping with existing under-frequency load-shedding (UFLS) schemes. Another venue of interest represents the development of market mechanisms for incentivizing and valuing synthetic damping in low-inertia power systems.

CHAPTER 4

METHODOLOGY TO COMPARE DER CO- ORDINATION SCHEMES

In this section, we illustrate a novel methodology for comparing and quantifying the performance of different DER coordination schemes' ability to deliver frequency regulation services across a number of salient criteria. The schemes considered include *i*) a bottom-up device-driven scheme called PEM [51]; *ii*) a fitness-based prioritization scheme [74], and *iii*) an optimization-based direct scheduling scheme [75]. The criteria of interest include tracking performance, scalability of communication, scalability of computation, device availability, ability to maintain consumer quality of service (CQoS) relative to delivered hot water temperatures, and impact on the device quality of service (DQoS) such as average cycling rates. Moreover, we augment the fitness-based method with an ability to estimate the fitness values dynamically which significantly reduces the communication burden while maintaining the tracking capability. Finally, the simulations and corresponding comparisons are based on a representative subset of PJM's historical Reg-D data.

The main contributions of this section are listed below:

- Quantitative methodology is proposed for holistically analyzing the performance of DER coordination schemes across a set of proposed salient and practical metrics.
- A fitness-based DER coordination scheme is specifically extended by enabling the DER coordinator to dynamically update the DER fleet’s fitness values, which permits significantly lower communication burden and DQoS without negatively impacting the ability to deliver grid services and CQoS.
- The real-time, cyber-enabled DER simulation platform from [76] is extended to incorporate two more DER coordination schemes. This improved platform is utilized in the simulation of a fleet of 1000 EWHs to illustrate the quantitative methodology for different DER coordination schemes from the literature.

The goal of any DER coordinator managing N TCLs is to maintain CQoS (i.e., keep $z_n[k]$ close to a customer’s desired set-point $z_n^{\text{set}} \in (z_n^{\text{min}}, z_n^{\text{max}}) \forall n$) while tracking reference signal in aggregate: minimize $\|P_{\text{ref}}[k] - \sum_{n=1}^N P_n^{\text{rate}} s_n[k]\|_2$. In doing so, a coordinator will need to cycle devices on/off while considering possible device lock-on/off constraints on device operations (impacting DQoS) and rely on computing and communications to be responsive to changes in the reference signal. PEM, fitness-based and optimization-based methods which were described in section 2.4 attempt to achieve these goals.

In this work, we consider two versions of (2.8):

1. `Opti(0)`: Allow DERs to cycle each time-step.

2. **Opti**(a): Limit cycling by locking the DER state $s_n[k]$ for a minutes every time we transition.

Since the optimization-based method does not look ahead more than one time step, we expect that locking will serve to simplify the problem (fewer decision variables), reduce cycling (and improve DQoS), and reduce communication overhead (since we do not need state info for locked TCLs), but at the cost of worse tracking and more CQoS violations.

For PEM, two versions are considered:

1. **PEM**(a, m_R): fixed packet length a and MTTR parameter m_R for all DERs in fleet.
2. **PEM**($[\underline{a}, \bar{a}], m_R$): every accepted request has random (and uniformly distributed) packet duration, $a \sim U[\underline{a}, \bar{a}]$, [2].

In the next subsection, the fitness-based method described in 2.4.3 is augmented to enable the estimation of the fitness values dynamically which reduces the communication burden while maintaining the tracking capability.

4.1 FITNESS-BASED COORDINATION AND ESTIMATION

To achieve the desired coordinator objectives (tracking and CQoS), the coordinator forms separate queues for on and off-fitness values. When aggregate DER fleet power, $\sum_{n=1}^N s_n[k]P_n^{\text{rate}}$, is larger than the reference signal, $P_{\text{ref}}[k]$, the coordinator will select

the devices with the highest $F_n^{\text{OFF}}[k]$ to turn off until $|P_{\text{ref}}[k] - \sum_{n=1}^N s_n[k]P_n^{\text{rate}}| \leq \epsilon$. The case when aggregate fleet power is lower than the reference signal is similar with the coordinator selecting the highest $F_n^{\text{ON}}[k]$ devices to turn on. A key challenge with the fitness-based method is the communication overhead associated with the coordinator keeping a fleet's fitness values up-to-date. That is, since TCLs compute their fitness values based on their dynamic state, which is a function of background demand, a device's fitness value may change significantly over a period of 5-15 minutes. This means that devices perceived by the coordinator to have a high/medium fitness value, may in fact no longer be "fit" for coordination and cause unexpected tracking errors or CQoS challenges. To address this challenge, we augment the fitness-based coordinator with a simple dynamic estimate of fitness values based on historical fitness data available to the coordinator. Thus, the dynamic fitness estimation should provide the coordinator with a more accurate estimate of the state of the fitness queues and improve CQoS. In improving CQoS, we expect lower opt-outs and more accurate tracking at an equivalent or lower communication overhead.

Thus, the coordinator is able to estimate the evolution of each device's ON and OFF fitness values with the following simple model:

$$F_{\text{est},n}^{\text{ON}}[k+1] = F_{\text{est},n}^{\text{ON}}[k] + \alpha_n^{\text{ON}}, \quad F_{\text{est},n}^{\text{ON}}[0] = F_n^{\text{ON}}[0] \quad (4.1)$$

where constant parameter α_n^{ON} is obtained from the coordinator's historical data on device n 's fitness values using linear regression. The case of $F_{\text{est},n}^{\text{OFF}}$ and α_n^{OFF} is identical. In the interval between devices updating their fitness value, the coordinator uses the dynamic estimate of fitness. Every 5-15 minutes, DERs update their fitness value based on the measured z_n using equation (2.14) which resets the fitness values at

coordinator to the actual ones.

In this work, we consider different versions of the fitness-based method, $\text{Fit}(a, b, C)$, where a , b , and C represents the devices' update rate for fitness values (mins), devices' locked out duration after cycling (mins), and whether coordinator employs dynamic fitness estimation or not (i.e., $C=E$ means *with* estimation).

Finally, Fig.4.1 summarizes the information flow for the aforementioned schemes, highlighting that they all represent different feedback control schemes that are each implemented in the real-time DER simulation platform from [76]. The green, red, and blue text describes the types of information shared in **Opti**, **Fit**, and **PEM** schemes, respectively. In the next section, we briefly outline the methodology for quantitatively comparing DER coordination schemes.

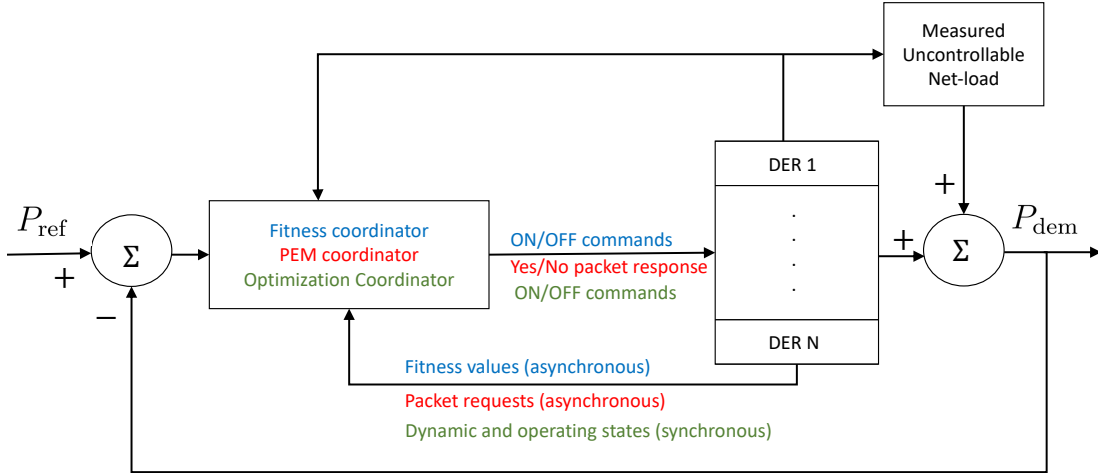


Figure 4.1: Feedback control system for different coordination schemes.

4.2 METHODOLOGY FOR COMPARING DER SCHEMES

To compare DER schemes, we have designed a set of metrics that are relevant for practical implementation and technical evaluation. To quantify the performance of any DER schemes in providing frequency regulation, consider N_s 1-hour samples of PJM's historical Reg-D data set, where each sample $i \in \{1, \dots, N_s\}$ represents $w_i \in [0, 1]$ proportion of the Reg-D data-set and $\sum_i w_i = 1$. Specifically, the metrics used to evaluate the performance of each scheme are denoted as follows for each 1-hour Reg-D sample i :

1. **Device QoS (DQoS):** $M_{4,i} = 1 - X_{4,i}/\max_i\{X_{4,i}\}$, where $X_{4,i}$ is the total number of DER cycles across fleet.
2. **Consumer QoS (CQoS):** $M_{3,i} = 1 - X_{3,i}/\max_i\{X_{3,i}\}$, where $X_{3,i}$ is the number of devices that experience opt-out.
3. **Scalability of communications (SoComm):** $M_{5,i} = 1 - X_{5,i}/\max_i\{X_{5,i}\}$, where $X_{5,i}$ is the average communication in kilobits per second (kbps) per device sent to/from the coordinator from/to DERs in one hour.
4. **Tracking accuracy:** $M_{1,i} = 1 - X_{1,i}/\max_i\{X_{1,i}\}$, where

$$X_{1,i} = \sqrt{\frac{1}{K} \sum_{k=1}^K \left(P_{\text{ref},i}[k] - \sum_{n=1}^N P_n^{\text{rate}} s_n[k] \right)^2},$$

and $K = 1800$ is the number of time-steps in Reg-D sample i .

5. **PJM composite score:** $M_2 \in [0, 1]$ is PJM’s formula and includes accuracy, precision, and delay component defined in [2].
6. **Scalability of computing (SoComp):** $M_{6,i} = 1 - X_{6,i}/\max_i\{X_{6,i}\}$, where $X_{6,i}$ is the total processing time used by coordinator.
7. **Device availability:** $M_{7,i} \in [0, 1]$ is defined as the average fraction of available devices [77], i.e., devices that are not locked nor opted out.

The above metrics are used to capture different facets of DER coordination. Because of trade-offs in control and communications, no single method will dominate across all metrics. Thus, a utility or aggregator must weigh the metrics based on their preferences. Now, for each 1-hour Reg-D sample $i \in \{1, \dots, N_s\}$, consider metric j , M_{ji} , for $j = 1, \dots, N_M$. Then, a DER coordination scheme’s weighted average metric j is $\overline{M}_j = \sum_{i=1}^{N_s} M_{ji}w_i \quad \forall j = 1, \dots, N_M$. In addition, to further characterize how each scheme performs across the set of N_s samples, we also consider the worst-case performance, $\underline{M}_j = \min_i\{M_{ij}\}$ for all N_M metrics. In the next section, we illustrate the methodology by quantifying the weighted mean and worst-case performance of three different classes of DER coordination across a representative subset of PJM’s 8760-hour Reg-D data set.

4.3 SIMULATION RESULTS

In this section, a simulation-based illustration of the methodology for comparing DER schemes is presented. The simulations consider sixteen representative 1-hour Reg-D samples of AGC. The process for selecting the representative samples (and their weights w_i) is briefly described next.

4.3.1 DETERMINING REPRESENTATIVE 1-HOUR AGC SAMPLES

In this section, we select a representative subset of the PJM Reg-D annual (8760 samples) data set by using K -mean clustering. This method partitions the PJM data set into K sub-sets from which we can select representative “centroids” and appropriate weights (related to relative sizes of the sub-sets).

In this work, for each 1-hour Reg-D sample, the sample’s average and pegging amount (which is the number of instances in the sample where the reference signal is at ± 1) are used in a K -mean clustering algorithm [78] to find the representative subset of the sample. Based on applying the K -mean algorithm and sweeping across a range of K , it was found that $N_s = 16$ clusters were optimal. Interestingly, the resulting 16 samples represent eight months of the year, all days of the week, and nine-day hours. In the next section, simulation-based analysis is used to illustrate the methodology for comparing DER coordination schemes across these N_s samples.

4.3.2 MULTI CRITERIA DECISION MAKING

Technique for Order of Preference by Similarity to Ideal Solution (TOPSIS), a well-known multi-criteria decision-making method [79], is used in this work to rank DER coordination schemes based on the aforementioned criteria. The fundamental idea of TOPSIS is to identify solutions that are closest to the ideal solution and farthest from the anti-ideal solution. The method can be summarized as follows,

1. **Normalization of the Decision Matrix:** Given a decision matrix, the values

are normalized to create a normalized decision matrix, R . The normalization is done using:

$$r_{ij} = \frac{a_{ij}}{\sqrt{\sum_{i=1}^m a_{ij}^2}}, \quad (4.2)$$

where a_{ij} is the original value of the decision matrix, and m is the number of alternatives.

2. **Calculate the Weighted Normalized Decision Matrix:** This is obtained by multiplying the normalized decision matrix by the corresponding weights of the criteria. If w_j is the weight of the j^{th} criterion, then:

$$v_{ij} = w_j \cdot r_{ij}. \quad (4.3)$$

3. **Determine the Ideal and Anti-Ideal Solutions:** The ideal solution, A^* , and the anti-ideal solution, A^- , are given by:

$$A^* = \left(\max_i v_{i1}, \max_i v_{i2}, \dots, \max_i v_{in} \right) \quad (4.4)$$

$$A^- = \left(\min_i v_{i1}, \min_i v_{i2}, \dots, \min_i v_{in} \right) \quad (4.5)$$

4. **Calculate the Separation Measures:** The separation from the ideal solution, S_i^* , and the separation from the anti-ideal solution, S_i^- , are computed for

each alternative as:

$$S_i^* = \sqrt{\sum_{j=1}^n (v_{ij} - A_j^*)^2} \quad (4.6)$$

$$S_i^- = \sqrt{\sum_{j=1}^n (v_{ij} - A_j^-)^2} \quad (4.7)$$

5. **Calculate the Relative Closeness to the Ideal Solution:** The relative closeness, C_i^* , of each alternative with respect to the ideal solution is given by:

$$C_i^* = \frac{S_i^-}{S_i^* + S_i^-} \quad (4.8)$$

6. **Rank the Alternatives:** Rank the alternatives in descending order based on their relative closeness to the ideal solution.

4.3.3 SIMULATION CASE STUDY

The results are shown next and leverage and extend the real-time, cyber-enabled DER simulation platform, which is detailed in [76]. Specifically, this paper augments the platform with optimization and fitness-based methods to enable comparisons of DER coordination methods. The simulation platform uses Python 3.9 for the simulation of diverse DER fleets. Local DER control logic and model is implemented in C/C++ based on the simplified first-order state of charge dynamics. Gurobi 9.0.1 solver is used for the optimization-based method. The DER coordinator is implemented in Python using the requests module and an open-source event-driven networking engine called Twisted. Specifically, Hypertext Transfer Protocol (HTTP) which is a

standard protocol for asynchronous communication between Web servers and clients, is used to exchange messages between DERs and coordinator. The platform uses communication mechanisms that closely align with those used by IoT-enabled devices in real-world demand dispatch. Specifically, the simulation platform enables a real-time simulation of 1000 EWHs, each of which has a 4.5 kW power rating, and the DER coordinator responds, in aggregate, to a Reg-D power reference signal that is updated every 2 seconds with a baseline power value equal to 400 kW and an amplitude (capacity) of ± 200 kW. The results for mean and worst performance are summarized in Table 4.1 where *avg* and *worst* refer to the average and worst values of $X_{j,i}$ across $i = 1, \dots, N_s$. To better illustrate the results, in Fig. 4.2, \overline{M}_j is compared for seven DER coordination schemes. In addition, in Fig. 4.3, the worst performance across all representative 1-hour samples is compared.

By comparing $\text{Fit}(15, 3, \text{NE})$ and $\text{Fit}(15, 3, \text{E})$ in table 4.1 it can be seen that CQoS is improved significantly when estimation is added to fitness based method (i.e., (4.1)). On the other hand, by comparing $\text{Fit}(3, 3, \text{NE})$ and $\text{Fit}(3, 3, \text{E})$, very small difference is seen. This shows that the estimation method is more useful when the fitness update time. When the update time is small, the error in fitness values is insignificant leading to a small impact on estimation. As expected, by increasing the update time, CQoS decreases due to an increase in the number of opt-outs.

As expected, $\text{Opt}(0)$ outperforms other methods in tracking \underline{M}_4 since it does have access to full knowledge and control. The main drawback is that the scalability of communication is low which makes the implementation difficult for large fleets. As expected, the DQoS index is the lowest for the optimization-based method since this method leads to more frequent cycling. By adding a lock in the optimization-based

method it can be seen that the number of cyclings significantly drops, but this will worsen tracking, and PJM scores considerably. In fact, lock-out represents a plant model change and the results show that the optimization method is not adapting well to this change in the plant model (i.e., when reality hits). By comparing $\text{Fit}(15, 3, E)$ and $\text{Fit}(15, 0, NE)$ it can be seen that removing the cycling constraint and using Eq. (2.15) improves the tracking ability both in terms of PJM composite score and tracking. The same impact is seen for the 3-minute fitness update time. In the PEM method, we can see that randomizing packets improves the tracking significantly while decreasing the CQoS since there exist longer packets in this case which are more likely to exceed the temperature limit. The results show that the fitness-based method and PEM can provide tracking scores close to the optimization-based method while providing much higher M_6 and M_7 scores.

Table 4.1: Comparing the performance of DER coordination schemes in terms of average and worst values of $X_{j,i}$ across $i = 1, \dots, N_s$

Method	DQoS		CQoS		SoComm(bps)		Tracking (kW)		PJM score		SoComp(sec)		Availability		Ranking
	avg	worst	avg	worst	avg	worst	avg	worst	avg	worst	avg	worst	avg	worst	
Fit(3, 3, NE)	1608	2145	62.0	104	1.470	2.942	7.9	30.2	0.940	0.896	0.031	0.039	0.967	0.963	2
Fit(3, 3, E)	1606	2139	63.4	101	1.470	2.942	7.5	28.7	0.940	0.896	0.137	0.148	0.967	0.964	5
Fit(3, 0, E)	1619	2221	62.8	99	1.470	2.942	1.5	1.6	0.943	0.902	0.142	0.155	0.999	0.998	1
Fit(15, 3, NE)	1774	2385	150.7	223	0.2978	0.2978	11.3	48.8	0.939	0.891	0.032	0.038	0.969	0.965	7
Fit(15, 3, E)	1605	2145	62.5	103	0.2978	0.2978	7.5	30.2	0.940	0.896	0.137	0.151	0.967	0.963	4
Fit(15, 0, E)	1617	2213	63.6	106	0.2978	0.2978	1.5	1.6	0.943	0.902	0.140	0.159	0.999	0.998	3
Opt(0)	49862	55449	0.063	1	68.11	68.12	4.6	6.6	0.944	0.905	9.117	10.98	0.999	0.999	10
Opt(3)	3558	4039	163	248	68.01	68.01	166.1	248.4	0.747	0.639	3.343	3.876	0.966	0.964	9
PEM(3, 3)	3797	4188	100.6	151	0.107	0.116	65.1	108.5	0.855	0.739	0.021	0.055	0.995	0.992	8
PEM([1, 5], 3)	3665	4057	112.7	150	0.107	0.113	37.1	72.9	0.919	0.863	0.023	0.047	0.997	0.996	6

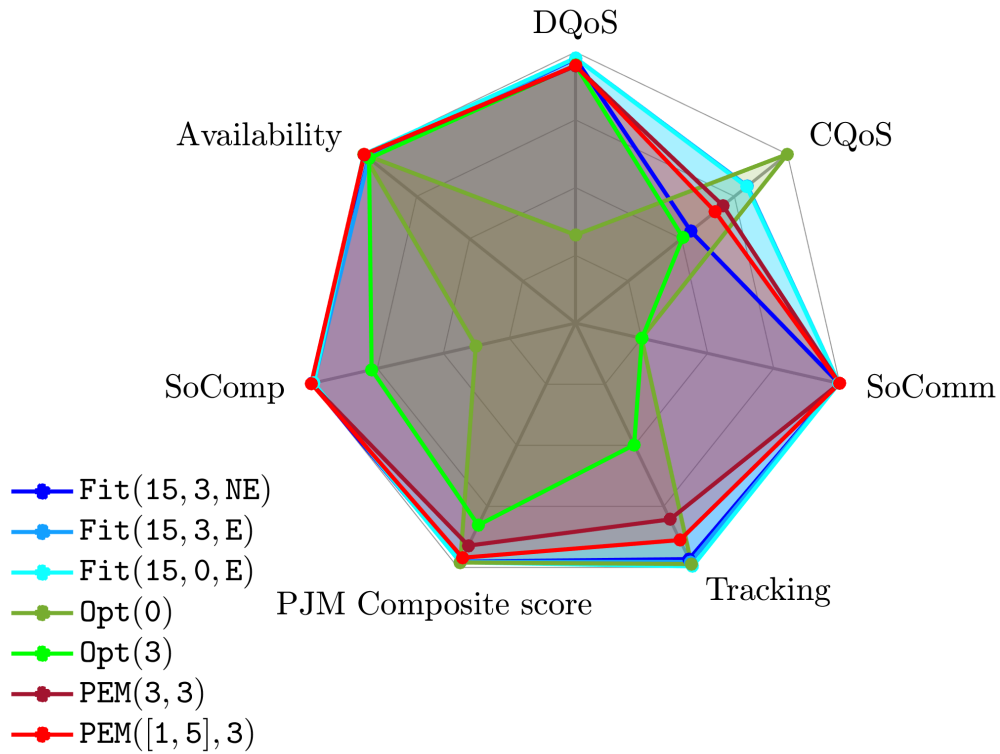


Figure 4.2: Comparing the mean performance of coordination schemes.

4.4 CONCLUSION

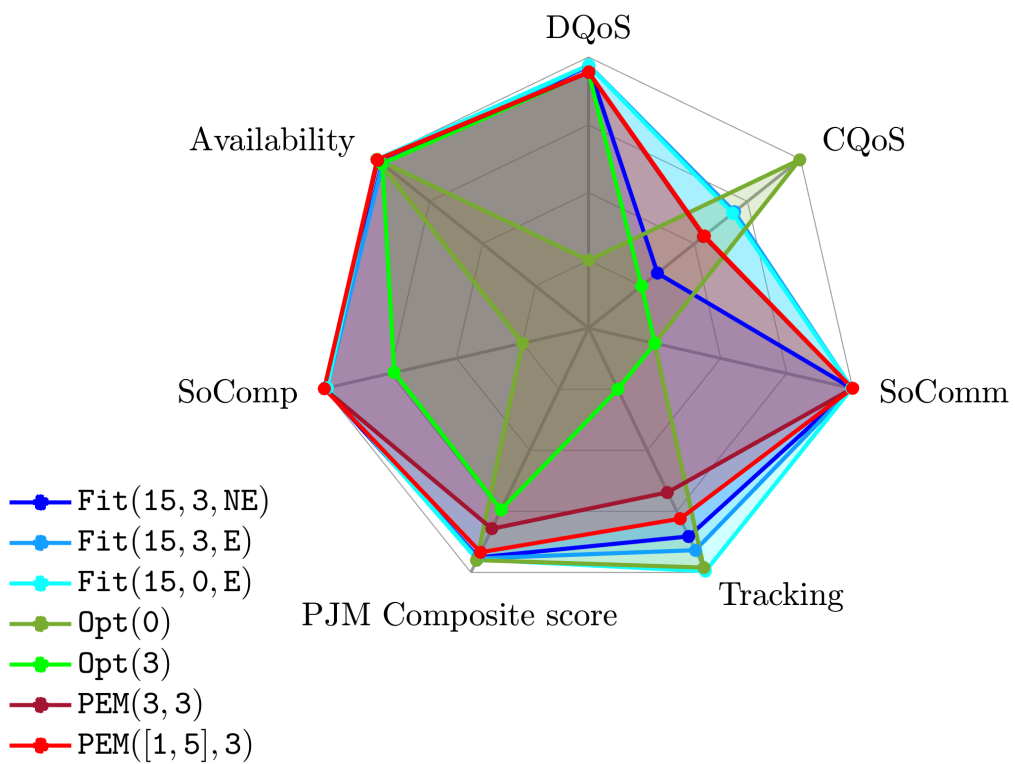


Figure 4.3: Comparing the worst performance of coordination schemes.

CHAPTER 5

HOSTING CAPACITY IN DISTRIBUTION SYSTEMS

In the literature, there are either simplified models used to compute hosting capacities with no guarantees or guarantees applicable only to simplified systems. It is within this context that this work contributes to the field of computing hosting capacity for realistic systems with outlined trade-offs between optimality and guaranteed feasibility:

- The recently presented optimization-based approach for computing the hosting capacity of single-phase distribution feeders in [43] has been extended to three-phase, unbalanced distribution feeders. An analysis is also conducted to provide technical conditions under which our proposed per-phase HC estimates can be combined to guarantee that 3-phase phase grid constraints are satisfied.
- The HC estimate for unbalanced feeders is then improved by iteratively adjusting voltage bounds within the per-phase optimization framework, accounting

for mutual impedances and unbalanced load in the 3-phase system.

- Finally, the methodology is validated through simulation-based analysis on the IEEE 37-node feeder and a real 3-phase network with more than 500 three-phase nodes.

This chapter uses CIA of the AC power flow to tackle the optimization problem of quantifying a three-phase distribution feeder's capacity to host DERs. This is often connoted HC, but herein we consider separative bounds for each node on positive and negative DER injections, which ensures that injections within these nodal limits satisfy feeder voltage and current limits and across nodes sum up to the feeder HC. The methodology decomposes a three-phase feeder into separate phases and applies CIA-based techniques to each phase. An analysis is developed to determine the technical condition under which this per-phase approach can still guarantee three-phase constraints. New approaches are then presented that modify the per-phase optimization problems to overcome conservativeness inherent to CIA methods and increase HC, including selectively modifying the per-phase impedances and iteratively relaxing per-phase voltage bounds. Discussion is included on trade-offs and feasibility. To validate the methodology simulation-based analysis is conducted with the IEEE 37-node test feeder and a real 534-node unbalanced radial distribution feeder.

5.1 EXTENDING CIA TO UNBALANCED FEEDERS

The method described in 2.5 is proposed in [80] to obtain HC for a balanced feeder. Given an unbalanced feeder, how can we approximate or decompose it for HC analysis? In this section, we seek to answer this question. Specifically, we consider methods for 1) approximating feeders as balanced (e.g., by modifying line impedances and nodal loads and 2) decomposing feeders along their phases. These are summarized next.

- **Method 1 - balanced feeder approximation:** This strategy involves transforming an unbalanced feeder into an *approximate* balanced model, which is then used to determine p^-, p^+ from $\mathbf{P}_{CIA}^{\phi,+ \setminus -}$. The resulting per-phase HC is then distributed equally to each phase. We consider two different ways to approximate a balanced feeder:
 - i) Take the maximum line impedance and minimum loads across all three phases to capture the worst-case voltage drop/rise.
 - ii) Average line impedances and loads across phases a/b/c to create a balanced approximation of a feeder. This approximation can potentially cause voltage violations at the corresponding HC value.
- **Method 2 - per-phase analysis:** In this approach, we extract each phase separately and compute p^- and p^+ . This per-phase approach is considered for two different implementations:

- i) One phase is selected and nodal HC values, (p_i^-, p_i^+) , are computed for that phase. For the 3-phase feeder, the same (p_i^-, p_i^+) values are then applied to all phases at a three-phase node. We denote the sub-methods $2i^\phi$ for $\phi = \{a, b, c\}$, e.g., $\overline{\text{HC}}_{3\phi} = 3 \times \mathbf{1}_N^\top p_a^+$ for method $2i^a$.
- ii) All three phases are extracted separately and we compute (p^-, p^+) for each phase, which yields hosting capacity, e.g., $\overline{\text{HC}}_{3\phi} = \mathbf{1}_N^\top (p_a^+ + p_b^+ + p_c^+)$.

Each of these methods estimate the three-phase HC, e.g., $\overline{\text{HC}}$ by computing net nodal injections, e.g., p_ϕ^+ , which are then applied to the full three-phase network to determine the corresponding three-phase voltages and currents. In Fig.5.1, these voltage and current profiles for Method 2ii are presented for the IEEE 37-node test feeder [81]. As can be seen, despite single-phase analysis underpinning the HC estimate, phase voltages are within $\bar{V} = 1.05$ pu across all nodes and phases. Next, we are interested in metrics that can be used to compare the different methods.

- **Total number of violations**, N_v , counts the number of nodes and phases for which $|V_i^{3\phi}| \notin [\underline{V}, \bar{V}]$.
- **Maximum violation in per unit**, M_v , provides a measure of the severity of the violations:

$$M_v = \max_{i=1, \dots, 3N} \left\{ \max \left\{ 0, E_i^u, E_i^l \right\} \right\}, \quad (5.1)$$

where, $E^u := |V^{3\phi}| - \bar{V} \mathbf{1}_{3N}$ and $E^l := \underline{V} \mathbf{1}_{3N} - |V^{3\phi}|$.

- **Sum of violations**, S_v , captures the cumulative severity of violations across

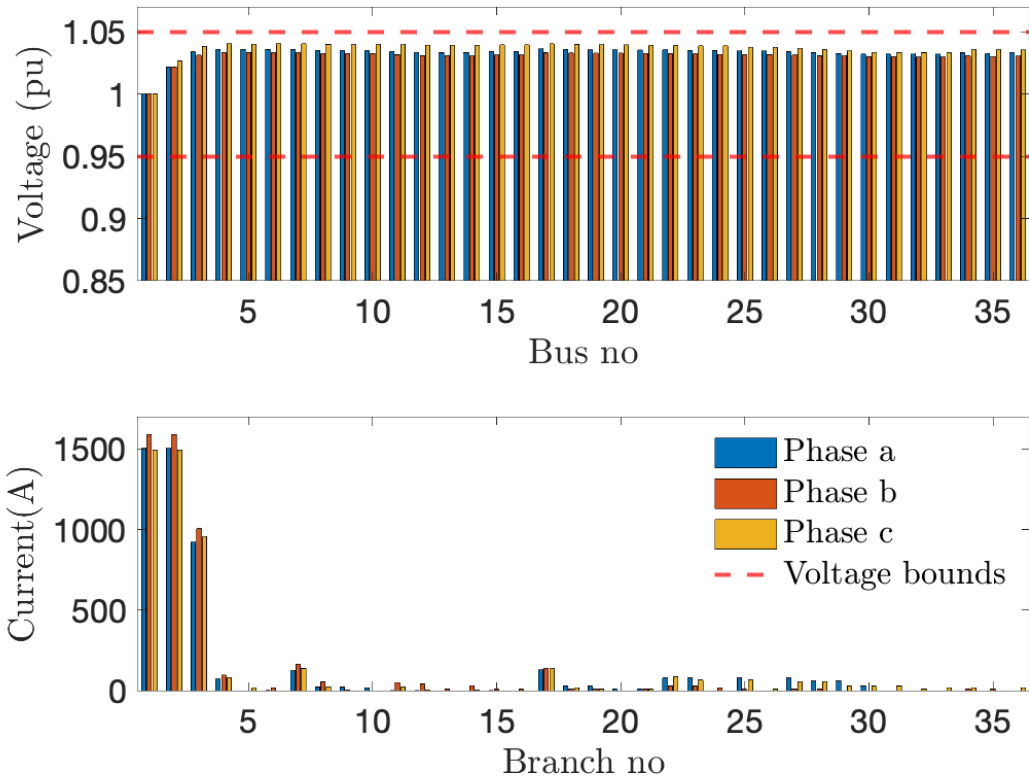


Figure 5.1: Illustrating the effects of Method 2ii on three-phase voltage and current profiles following the addition of nodal injections $p_a^+ + p_b^+ + p_c^+$. The dashed red line indicates the ANSI voltage limits of $[0.95, 1.05]$ pu.

the network:

$$S_v = \sum_{i=1}^{3N} \max(0, E_i^u, E_i^l). \quad (5.2)$$

- **Average voltage margin**, W_M , measures how conservative the HC results from $\mathbf{P}_{\text{CIA}}^{\phi,+/-}$ are:

$$W_M = \frac{1}{3N} \sum_{i=1}^{3N} \max\{0, \Delta W_i\}, \quad (5.3)$$

where $\Delta W_i := \min\{|V_i^{3\phi}| - \underline{V}, \bar{V} - |V_i^{3\phi}|\}$.

- **Voltage unbalance factor (VUF)** provides a relative measure (in %) of voltage unbalance caused by nodal HC injections:

$$\text{VUF} = \frac{100}{N} \sum_{i=1}^N \frac{\max\{|V_i^{3\phi}| - \frac{1}{3}\mathbf{1}_3^\top |V_i^{3\phi}| \mathbf{1}_3\}}{\frac{1}{3}\mathbf{1}_3^\top |V_i^{3\phi}|}. \quad (5.4)$$

It should be noted that none of the methods leads to voltage violation in the IEEE 37 node feeder. That is due to the inherent conservativeness of the CIA. To provide a clearer distinction between methods 1 and 2, three scenarios are considered: *i*) the load in phase c is increased by 20% while decreasing loads in phase b by an equal margin. *ii*) in scenario *i*, the loads are swapped between phases b and c. *iii*) in scenario *i*, the loads are swapped between phases a and b. The power factor is kept fixed. Table 5.1 uses the metrics above to compare minimum HC estimates, i.e., using $\mathbf{P}_{\text{CIA}}^{\phi,-}$, W_M , VUF, S_v and N_v , for scenarios *i*, *ii* and *iii*. To further compare the performance of the aforementioned methods, 100 scenarios are

generated by gradually increasing the load from 0 to 40% in each of the scenarios *i*, *ii*, and *iii*. The cumulative distribution function (CDF) of W_M , VUF, S_v , and N_v is presented in Figs. 5.2 to 5.6. Notably, the comparison shows that Method 2ii does not incur any voltage violations. Additionally, in Method 2ii, the variation in W_M is notably less than that observed in other methods. While other methods can result in either a low W_M (potentially causing voltage violations) or an excessively high W_M (indicating over-conservatism) for certain scenarios, Method 2ii maintains a more balanced approach across all scenarios. Method 1i leads to an overly loaded network which makes the optimization problem infeasible. Other methods have resulted in voltage violations. Therefore, results in Table 5.1 justify the selection of Method 2ii for further analysis. Given that Method 2ii uses information from all phases without averaging, it was somewhat expected that Method 2ii could outperform the other approaches. It should be noted that considering the mutual impedance can lead to less or more conservative HC depending on the characteristics of z_{ij}^m . The next section presents technical conditions under which per-phase analysis and HC optimization extend to three-phase networks.

5.2 MODIFYING $\mathbf{P}_{\text{CIA}}^{\phi,-/+}$ FOR THREE-PHASE GRID

In this section, we present an approach for adapting the per-phase HC estimates to deal with the inherent conservativeness of CIA. The method effectively modifies the impedance matrix to take into account the impact of mutual impedance. The approach makes the following assumptions:

Assumption 4. *The sum of the phase load currents is zero.*

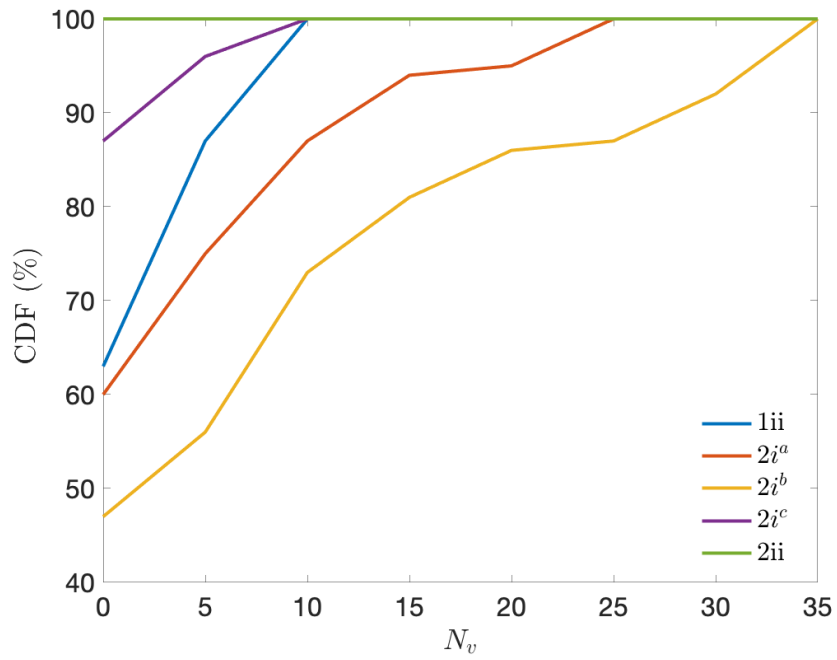


Figure 5.2: Comparison of N_v between different methods across 100 scenarios.

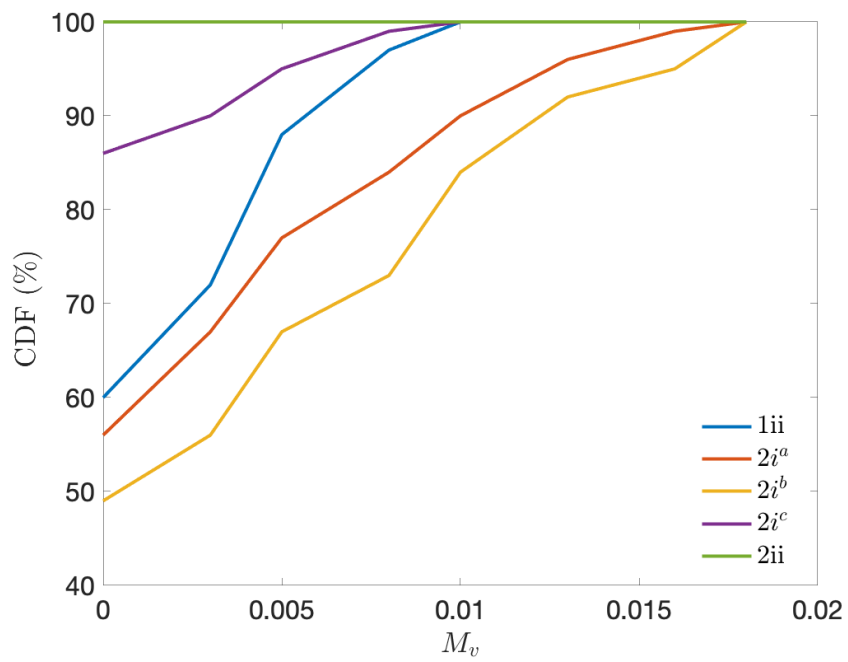


Figure 5.3: Comparison of M_v (pu) between different methods across 100 scenarios.

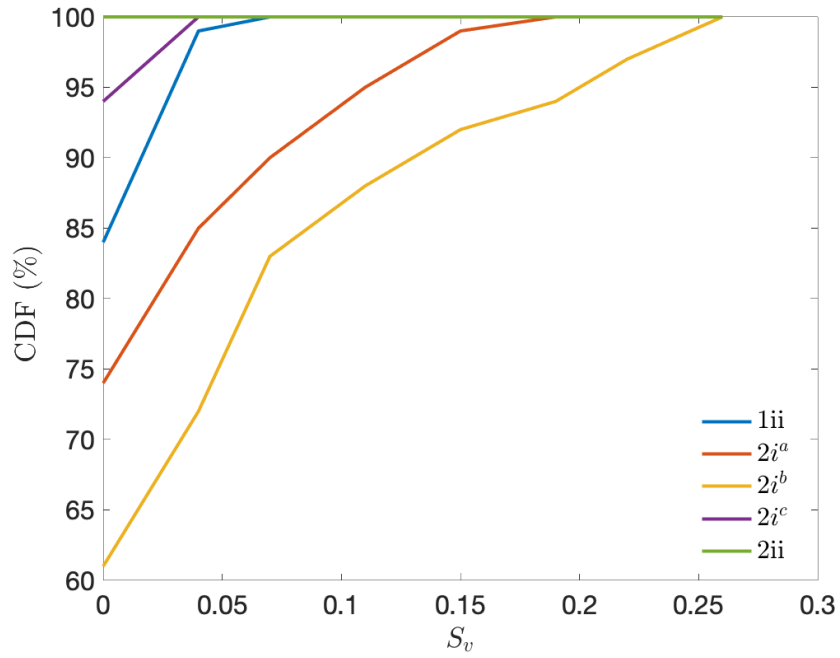


Figure 5.4: Comparison of S_v (pu) between different methods across 100 scenarios.

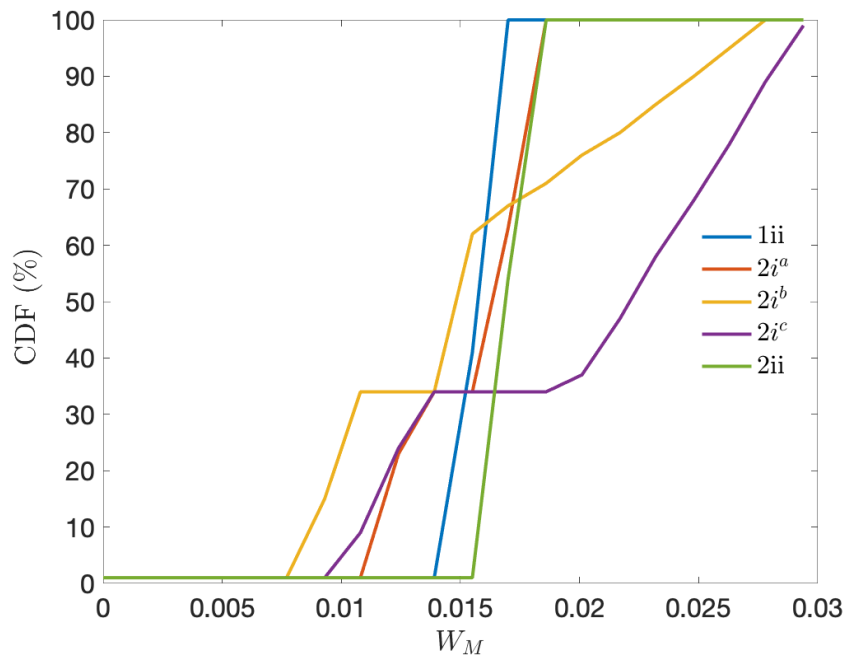


Figure 5.5: Comparison of W_M (pu) between different methods across 100 scenarios.

Table 5.1: Performance of the proposed methods for Three Scenarios

Method	N_v	$M_v(\text{pu})$	VUF (%)	S_v (pu)	W_M (pu)	$\frac{HC}{(MW)}$
Scenario 1						
1i	0	0	0.74	0	0.0395	0
1ii	0	0	0.48	0	0.0173	-14.68
2i ^a	0	0	0.49	0	0.0187	-14.03
2i ^b	0	0	0.56	0	0.0248	-11.07
2i ^c	4	0.0028	0.44	0.0086	0.0129	-16.82
2ii	0	0	0.58	0	0.0185	-13.98
Scenario 2						
1i	0	0	0.81	0	0.0392	0
1ii	8	0.0043	1.03	0.0166	0.0172	-14.68
2i ^a	4	0.0028	1.02	0.0086	0.0185	-14.03
2i ^b	24	0.0125	1.08	0.1240	0.0108	-18.13
2i ^c	0	0	0.96	0	0.0267	-10.03
2ii	0	0	0.40	0	0.0188	-14.06
Scenario 3						
1i	0	0	0.88	0	0.0394	0
1ii	9	0.0050	1.10	0.0234	0.0174	-14.68
2i ^a	14	0.010	1.14	0.0763	0.0133	-16.81
2i ^b	9	0.006	1.11	0.0342	0.0164	-15.19
2i ^c	0	0	1.03	0	0.0268	-10.03
2ii	0	0	0.45	0	0.0187	-14.01

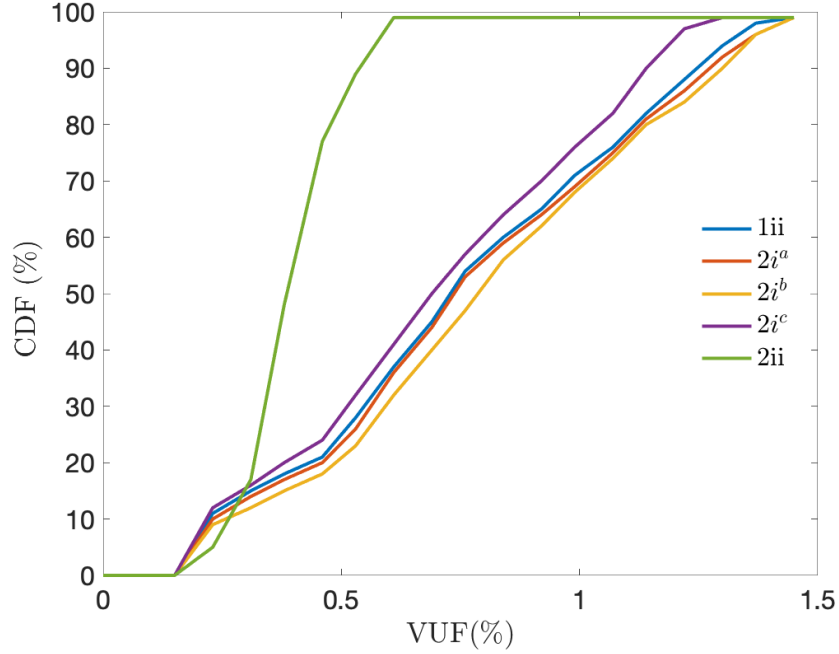


Figure 5.6: Comparison of $VUF(\%)$ between different methods across 100 scenarios.

Assumption 5. Three-phase lines are transposed, such that mutual impedances are

$$\text{identical: } z_{ij}^{3\phi} = \begin{bmatrix} z_{ij}^a & z_{ij}^m & z_{ij}^m \\ z_{ij}^m & z_{ij}^b & z_{ij}^m \\ z_{ij}^m & z_{ij}^m & z_{ij}^c \end{bmatrix}.$$

From the above assumptions, the following theorem holds.

Theorem 4. Given a 3-phase system that satisfies Assumptions 4 and 5, if per-phase optimization $\mathbf{P}_{CIA}^{\phi,+}$ satisfies $\underline{V} \leq V_i(p^+) \leq \bar{V} \forall i \in \mathcal{V}$, then the three-phase system satisfies $\underline{V} \leq V_i^{3\phi}(p^+) \leq \bar{V} \forall i \in \mathcal{V}$. Same holds for $\mathbf{P}_{CIA}^{\phi,-}$ and $V_i(p^-)$.

Proof: please see Appendix 5.6.

Theorem 4 states when a three-phase distribution feeder can be decomposed into three decoupled single-phase distribution systems with modified impedances, $z_{ij}^{\phi} - z_{ij}^m$,

to provide guarantees that the resulting HC will not engender voltage violations in the three-phase system.

Remark. *Using a similar approach, and by further assuming identical conductor impedances $z_{ij}^a = z_{ij}^b = z_{ij}^c$, Theorem 4 extends to Delta-connected loads.*

For real power systems, when assumptions 4 and 5 do not hold z_{ij}^m is approximated by

$$z_{ij}^m = (z_{ij}^{\mathbf{ab}} + z_{ij}^{\mathbf{ac}} + z_{ij}^{\mathbf{bc}})/3. \quad (5.5)$$

From each phase, we construct a sub-feeder from which we can compute nodal HC (net) injections p_i^- and p_i^+ using Method 2ii. The resulting voltages of the single-phase networks, $|V_i|$, are then compared with those of the full 3-phase load flow, $|V_i^{3\phi}|$, with the 3-phase (net) injections $p_{3\phi}^+ := [p_{a,i}^+, p_{b,i}^+, p_{c,i}^+]_{i \in \mathcal{V}}$ added to the system load. We denote the approach of solving $\mathbf{P}_{\text{CIA}}^{+/-}$ with modified impedance from Theorem 4 as **Mod-Z** HC.

In Fig. 5.7, a scatter plot of three-phase and single-phase voltage magnitudes is provided, i.e., $|V_i^{3\phi}|$ vs. $|V_i|$ for IEEE 37-node system. The red dots represent $|V_i^{3\phi}|$ with injections $p_{3\phi}^+$ added and the blue dots correspond to $|V_i^{3\phi}|$ when $p_{3\phi}^-$ is added. Fig. 5.8 shows the results after applying **Mod-Z**. Specifically, in $\mathbf{P}_{\text{CIA}}^+$ and $\mathbf{P}_{\text{CIA}}^-$, the impedance of each line is augmented by the mutual impedance from (5.5). The same results are presented for the 534-node feeder in Figs. 5.9 and 5.10. It can be seen in Fig. 5.9 that in the 534-node feeder the difference between $|V_i^{3\phi}|$ and $|V_i|$ is more significant. Therefore, we expect that using the Mod-Z method should lead to more improvement in the 534-node feeder compared to the IEEE 37-node feeder.

As expected, using the proposed method, the single-phase voltages become very close to the three-phase voltages since the impact of mutual impedance is considered. The small differences in Fig. 5.8 between $|V_i^{3\phi}|$ and $|V_i|$ are caused by (5.5).

It should be noted that using the modified impedance in \mathbf{P}_{CIA}^+ and \mathbf{P}_{CIA}^- successfully increases the HC by incorporating the mutual impedances in the \mathbf{P}_{CIA}^+ problem. Specifically, \overline{HC} increases from 25.09 MW to 30.22 MW (a 20% increase), while \underline{HC} increases from 14.89 MW to 19.30 MW (a 30% increase). However, this increase can lead to voltage violations as seen in Fig. 5.8.

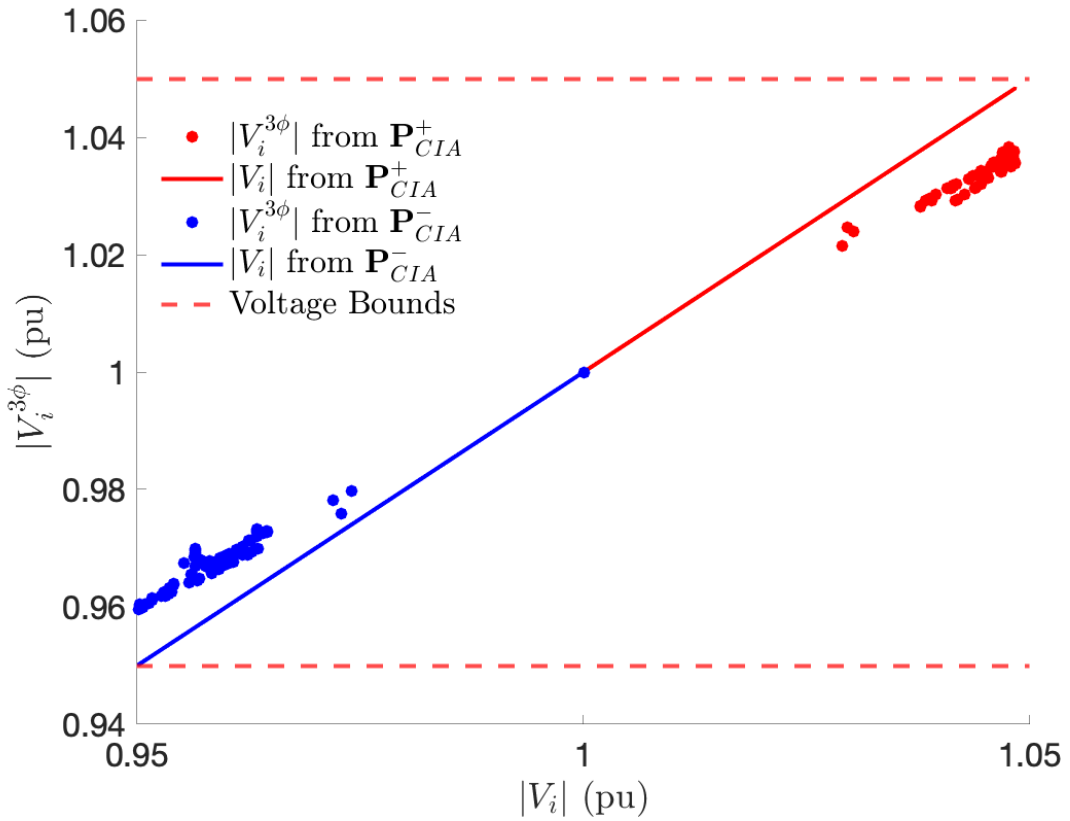


Figure 5.7: Comparison between three-phase and single-phase voltages for the modified IEEE 37-node system. The dashed red lines indicate the voltage limits.

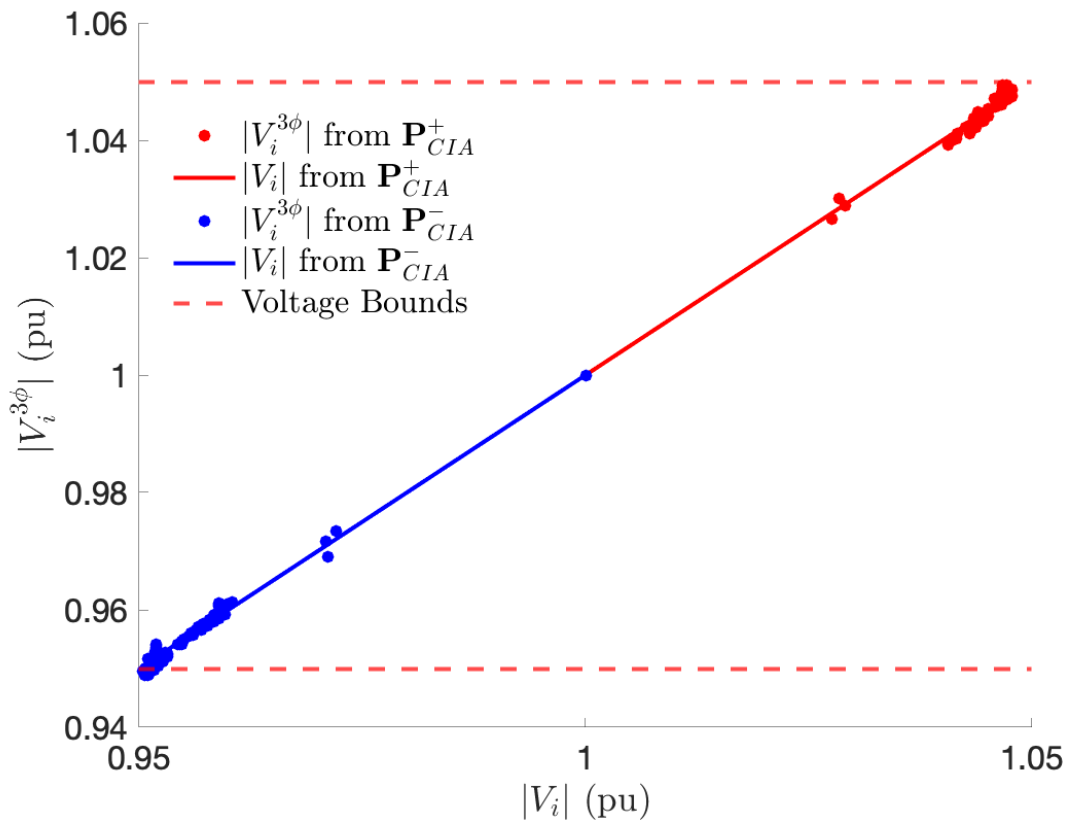


Figure 5.8: Three-phase voltages after modifying the impedance matrix based on Theorem 4 for the IEEE 37-node system. The dashed red lines indicate the voltage limits.

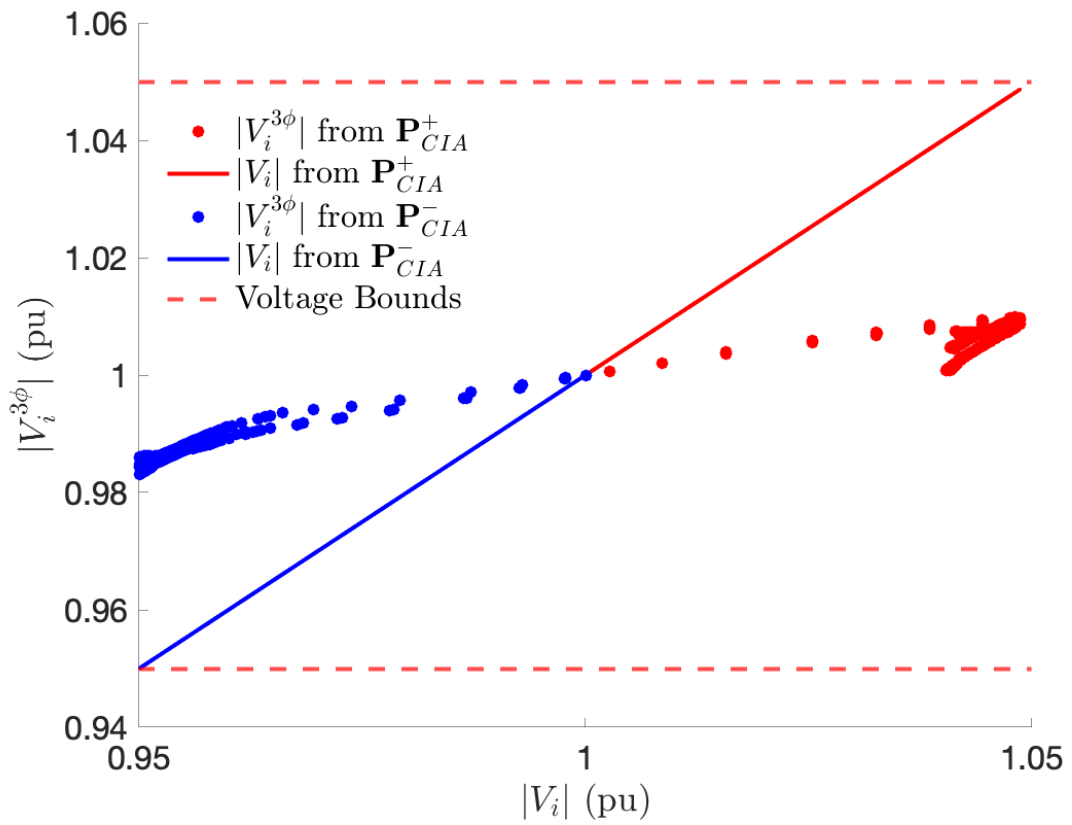


Figure 5.9: Comparison between three-phase and single-phase voltages for the modified 534-node feeder. The dashed red lines indicate the voltage limits.

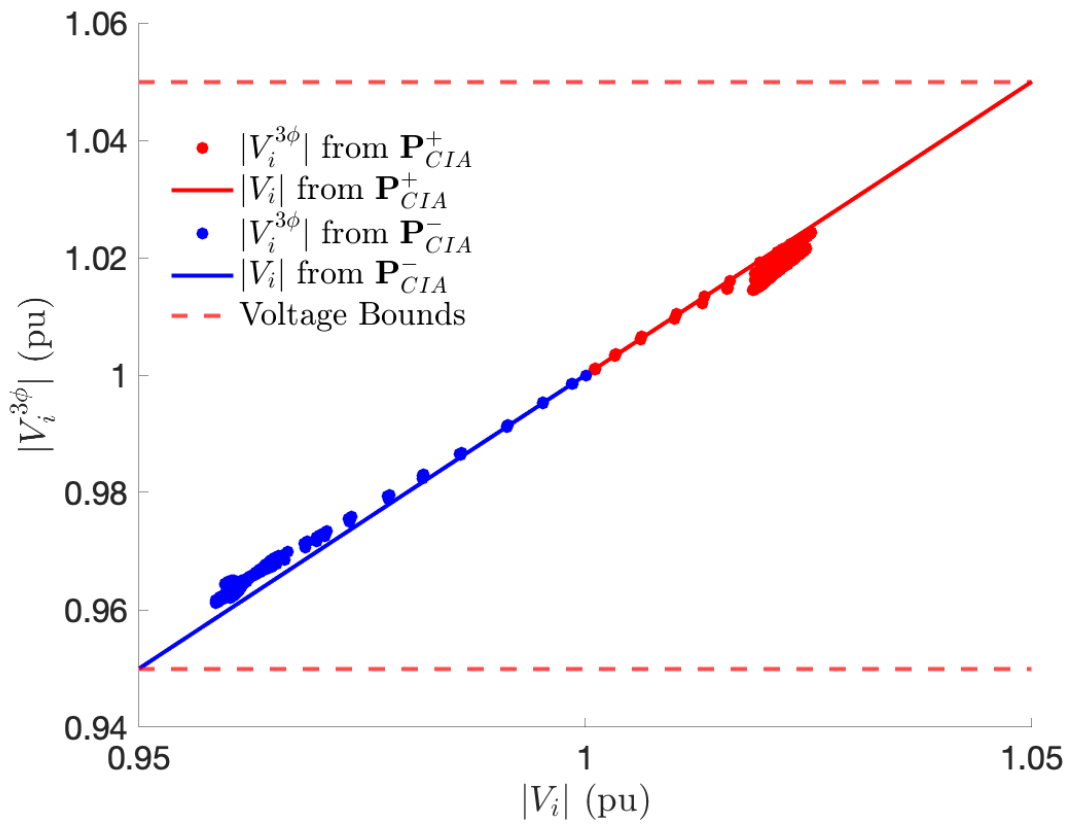


Figure 5.10: Three-phase voltages after modifying the impedance matrix based on Theorem 4 for the 534-node feeder. The dashed red lines indicate the voltage limits.

Table 5.2: The impact of modifying the impedance matrix on HC and voltage violations for the modified IEEE 37-node system.

ϵ (pu)	0	0.0005	0.0010	Method 2ii
$\overline{\text{HC}}$ (MW)	30.2	27.5	27.4	25.1
$\underline{\text{HC}}$ (MW)	-19.3	-17.5	-17.3	-14.9
N_v	10	5	0	0
M_v	0.0012	0.0004	0	0
# modified lines in $\mathbf{P}_{\text{CIA}}^+/\mathbf{P}_{\text{CIA}}^-$	36/36	22/27	9/16	-

5.2.1 ITERATIVE MOD-Z

In the remainder of this section, we present a simulation-based approach to adjust the impedance matrix in Mod-Z to eliminate the voltage violations. Thus, instead of (naively) altering the impedance for all branches at once, only the branches connected to nodes with simulated voltage violations are modified. Specifically, we modify the impedance of lines connected to nodes which satisfy the following condition,

$$\left| |V_i^{3\phi}| - |V_i| \right| > \epsilon \quad \forall i, \quad (5.6)$$

where ϵ is a design parameter that allows us to limit the number of line modifications. We denote Mod-Z(ϵ) as the Mod-Z method with the parameter ϵ . Modifying more lines leads to higher HC, but it comes at the cost of increased voltage violations. No free lunch in engineering.

To explore this tradeoff further, Table 5.2 tabulates the effects of different ϵ values in the **Mod-Z** approach. Clearly, with $\epsilon = 0.0010$ pu, only 9 of 36 lines are modified in $\mathbf{P}_{\text{CIA}}^+$, while all voltage violations are eliminated, and the reduction in HC is less than 10%.

This section showed the value of selectively modifying line impedances to enable per-phase optimization to apply directly to unbalanced distribution systems. Next, we seek to further enlarge the three-phase HC by not just modifying impedances of each phase, but also by (incrementally) relaxing voltage bounds in the per-phase optimization formulation.

5.2.2 MOD-Z FOR UNBALANCED GRIDS

In this subsection we look at conditions when the assumptions 4, 5 are slightly relaxed. First, assume that the load is unbalanced. That is, $|I_{ij}^a + I_{ij}^b + I_{ij}^c| \leq \epsilon$. This leads to,

$$-\epsilon \leq I_{ij}^a + I_{ij}^b + I_{ij}^c \leq \epsilon \quad (5.7)$$

$$I_{ij}^a - \epsilon \leq I_{ij}^b + I_{ij}^c \leq I_{ij}^a + \epsilon \quad (5.8)$$

similarly, for phase b and c, we have:

$$I_{ij}^b - \epsilon \leq I_{ij}^a + I_{ij}^c \leq I_{ij}^b + \epsilon \quad (5.9)$$

$$I_{ij}^c - \epsilon \leq I_{ij}^a + I_{ij}^b \leq I_{ij}^c + \epsilon \quad (5.10)$$

Using the above equations, for phase a, we have,

$$\Delta V_{ij}^a = z_{ij}^a I_{ij}^a + z_{ij}^m (I_{ij}^b + I_{ij}^c) \quad (5.11)$$

which leads to,

$$z_{ij}^a I_{ij}^a + z_{ij}^m (-\epsilon - I_{ij}^a) \leq \Delta V_{ij}^a \leq z_{ij}^a I_{ij}^a + z_{ij}^m (\epsilon - I_{ij}^a) \quad (5.12)$$

$$I_{ij}^a (z_{ij}^a - z_{ij}^m) - \epsilon z_{ij}^m \leq \Delta V_{ij}^a \leq I_{ij}^a (z_{ij}^a - z_{ij}^m) + \epsilon z_{ij}^m \quad (5.13)$$

Using the same procedure for phase b and c, we get:

$$\begin{aligned} & \left(\begin{bmatrix} z_{ij}^a - z_{ij}^m & 0 & 0 \\ 0 & z_{ij}^b - z_{ij}^m & 0 \\ 0 & 0 & z_{ij}^c - z_{ij}^m \end{bmatrix} + z_{ij}^m \epsilon \mathbf{1}_3 \right) I_{ij}^{3\phi} \leq \Delta V_{ij}^{3\phi} \\ & \leq \left(\begin{bmatrix} z_{ij}^a - z_{ij}^m & 0 & 0 \\ 0 & z_{ij}^b - z_{ij}^m & 0 \\ 0 & 0 & z_{ij}^c - z_{ij}^m \end{bmatrix} + z_{ij}^m \epsilon \mathbf{1}_3 \right) I_{ij}^{3\phi}. \end{aligned} \quad (5.14)$$

For $\epsilon \approx 0$, (5.14) is equal to (6.11). Load Unbalance, represents an added voltage buffer equal to $z_{ij}^m \epsilon$. Next, we use an experiment to study the impact of ϵ on the performance of the mod-Z method. The goal is to check how sensitive the results are for different ϵ . To do so, all of the impedances in phase a are multiplied by α while the impedances in phase c are divided by α . Then α is changed between 1 to 2, in 20 steps and the results for each step are stored. Increasing α leads to more unbalance in line impedances. We measure the impedance unbalance as follows,

$$\text{ZUF} = \frac{100}{N-1} \sum_{i=1}^{N-1} \frac{\max \left\{ |Z_{ij}^{3\phi}| - \frac{1}{3} \mathbf{1}_3^\top |Z_{ij}^{3\phi}| \mathbf{1}_3 \right\}}{\frac{1}{3} \mathbf{1}_3^\top |Z_{ij}^{3\phi}|}. \quad (5.15)$$

Increasing α increases ZUF as seen in the following figure. $P_{CIA}^{+/-}$ problems only use self

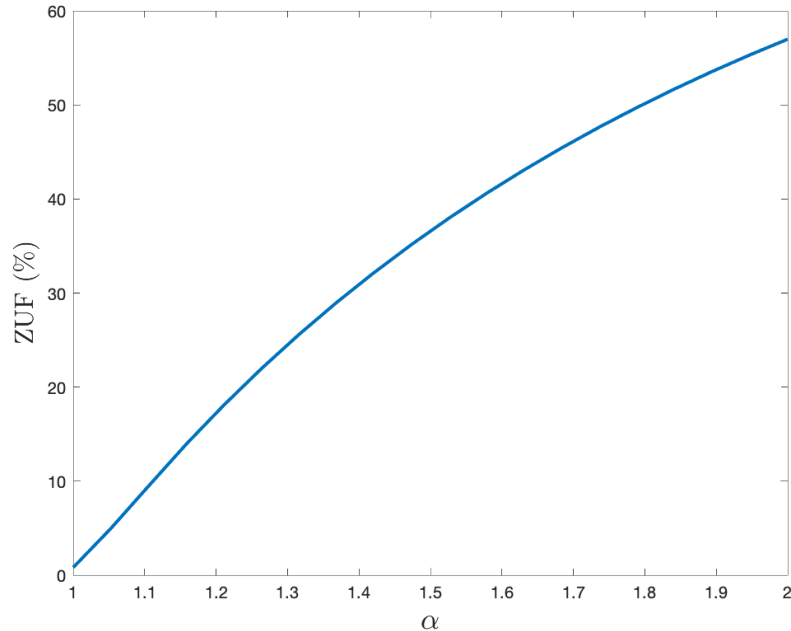


Figure 5.11: ZUF (%) versus α for different scenarios in the IEEE 37 bus system.

impedances to find HC. Therefore, higher unbalance in self impedances, i.e., higher ZUF, results in increased difference between HC in different phases. This can be seen in Fig. 5.12. As expected, higher impedance has led to lower HC and vice versa. This unbalance in HC, leads to unbalance in load, increasing ϵ as shown below. For higher values of ϵ the assumption 4 is not valid anymore. This can lead to voltage violations in mod-Z. N_v and M_v are shown for different values of ZUF. It can be seen that if the impedance of different phases is very different, then mod-Z leads to large violations. One should keep that into consideration when using mod-Z. It should be noted that in real power systems, typical values of ZUF are less than 1 %. In the next subsection, a novel iterative method to find HC is proposed which guarantees no grid constraint violations.

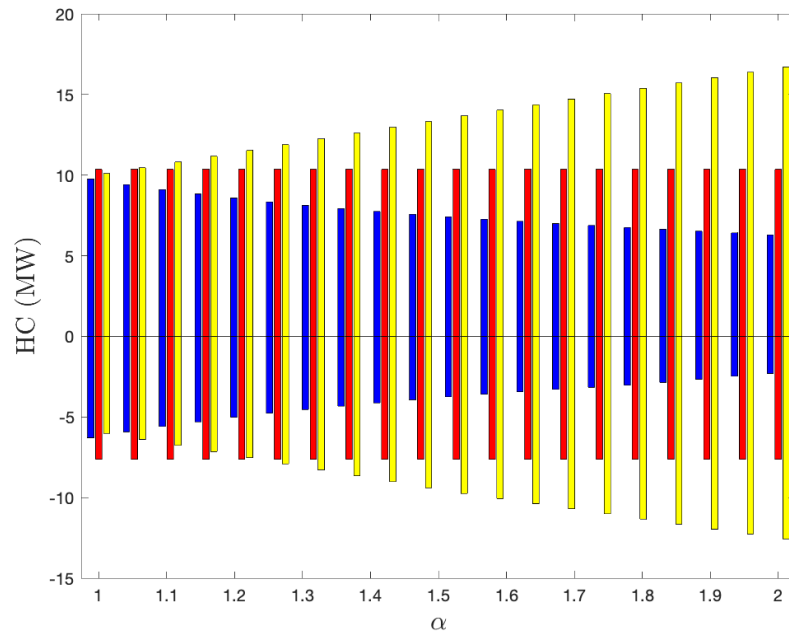


Figure 5.12: HC versus α in the IEEE 37 bus system. Blue, red and yellow curves show the HC for phases a, b, and c, respectively.

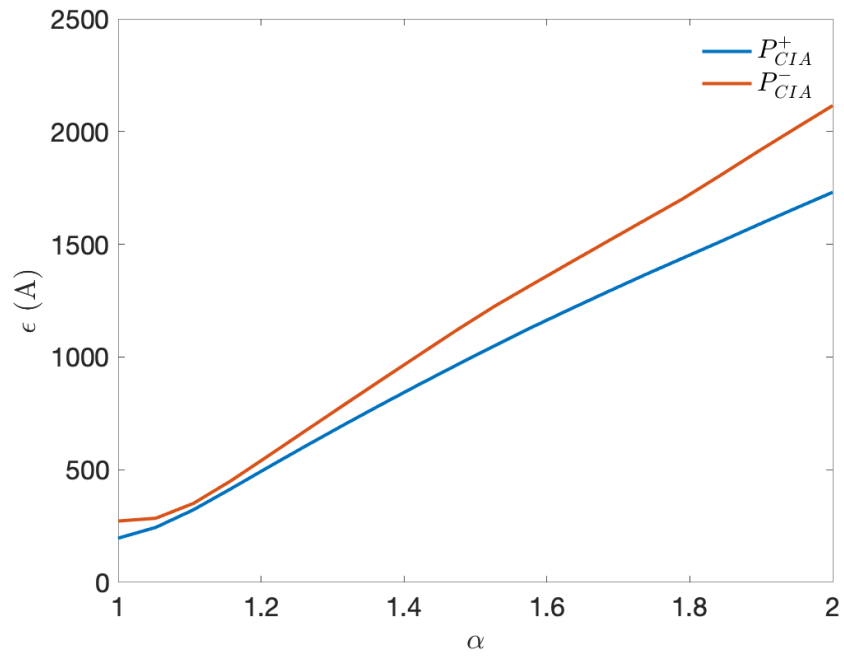


Figure 5.13: ϵ versus α in the IEEE 37 bus system.

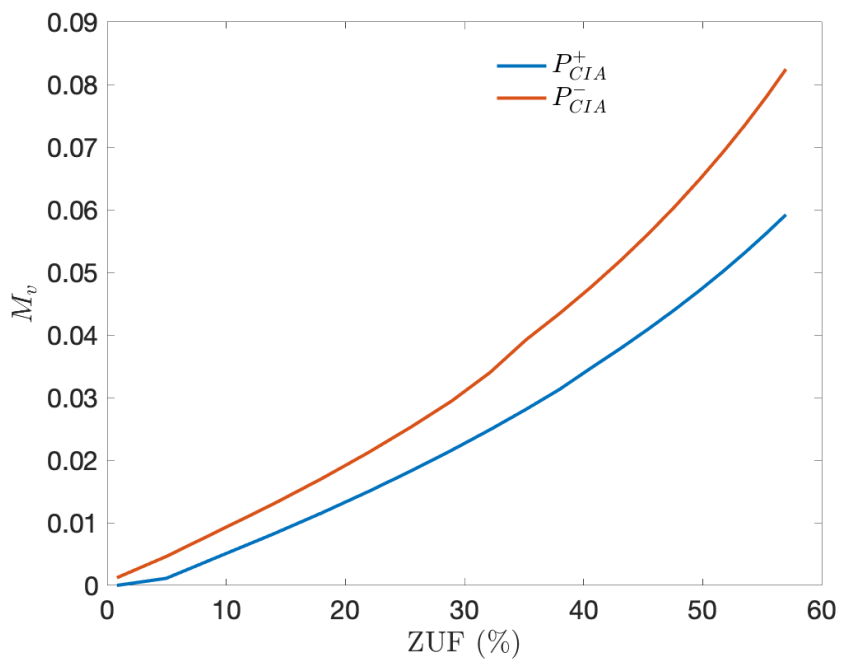


Figure 5.14: M_v versus ZUF in the IEEE 37 bus system.

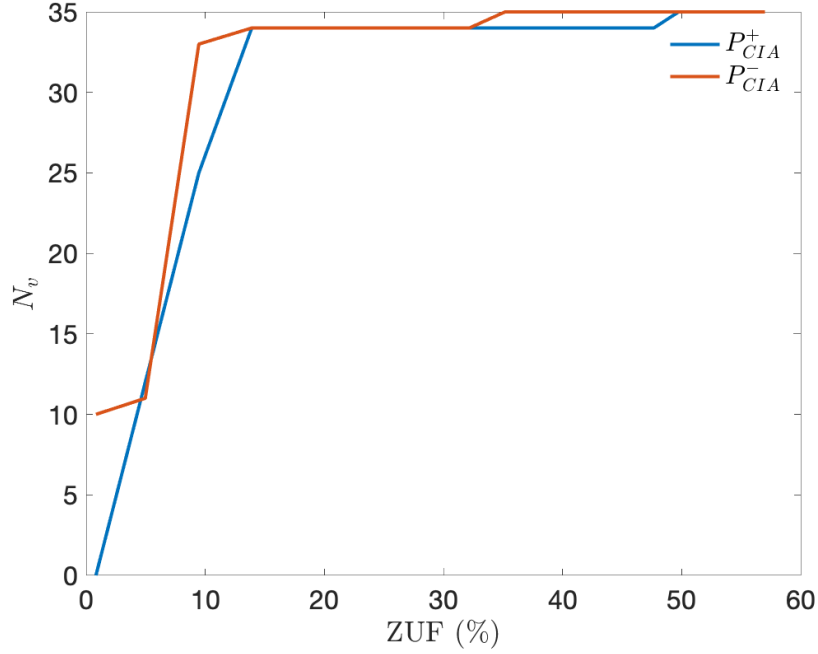


Figure 5.15: N_v versus ZUF in the IEEE 37 bus system.

5.3 ITERATIVE VOLTAGE BOUNDS TO INCREASE HC

In this section, a novel approach is introduced that incrementally improves the three-phase HC estimate by coupling 3-phase load flows with per-phase optimization $\mathbf{P}_{CIA}^{\phi,+ \setminus -}$. The proposed method is summarized in Fig. 5.16 and outlined as follows for $p^+ \overline{\text{HC}}$ (the approach is similar for p^- and $\underline{\text{HC}}$):

1. *Single-phase optimization*: given per-phase voltage bounds \underline{V} and \overline{V} , solve \mathbf{P}_{CIA}^+ for each phase using Method 2ii to get nodal HC values p_ϕ^+ and $\overline{\text{HC}}_\phi$.
2. *Single-phase load flow*: Apply p_ϕ^+ to each phase ϕ and perform single-phase load

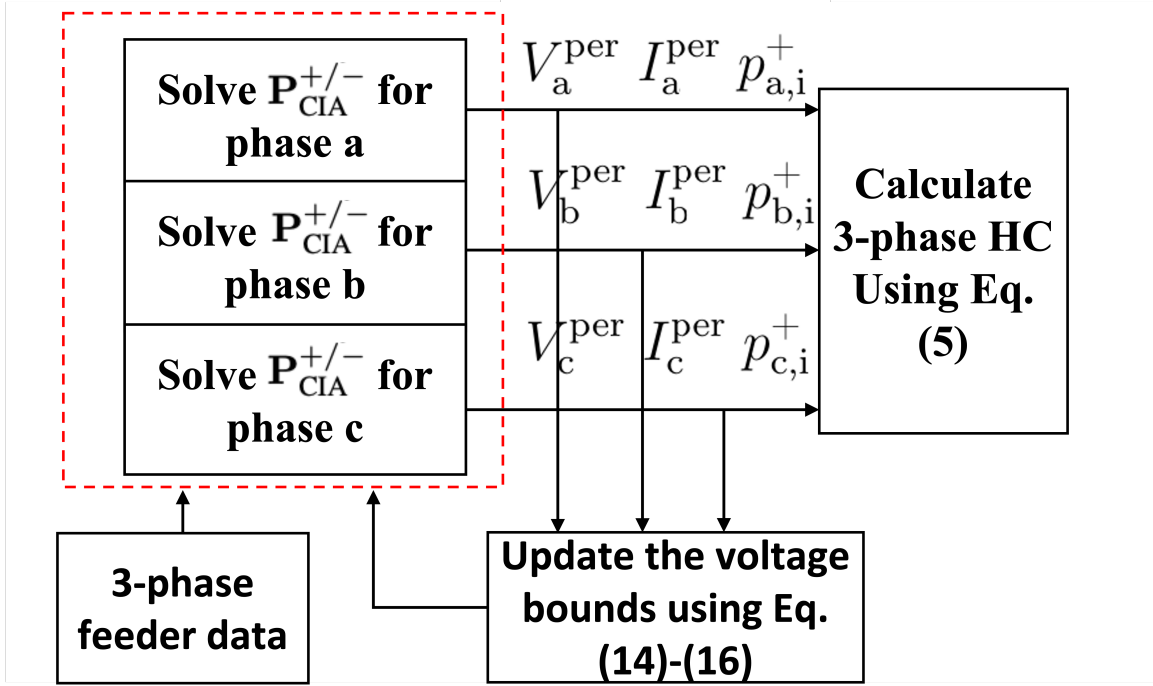


Figure 5.16: Flowchart of the proposed iterative voltage bound approach.

flow: V_ϕ^{per} and I_ϕ^{per} .

3. *Three-phase load flow*: Apply $\{p_\phi^+\}_{\phi=\{a,b,c\}}$ to 3-phase system and perform load flow: $V^{3\phi}$ and $I^{3\phi}$.
4. *Termination condition*: The algorithm stops if any element of $|V_i^{3\phi}|$ exceeds $[\underline{V}, \bar{V}]$.
5. *Estimate per-phase voltage*: The per-phase model ignores mutual impedances, which leads to a voltage difference across phases relative to the three-phase model. To estimate this difference, consider (2.7) and assume currents $I_{ij}^\phi \approx I_{ij, \phi}^{3\phi}$ are common across both the per-phase and three-phase systems. Then, the estimated voltage for each phase becomes,

$$V_j^{\text{est}} = V_i^{\text{est}} - \begin{bmatrix} z_{ij}^a & z_{ij}^{\text{ab}} & z_{ij}^{\text{ac}} \\ z_{ij}^{\text{ba}} & z_{ij}^b & z_{ij}^{\text{bc}} \\ z_{ij}^{\text{ca}} & z_{ij}^{\text{cb}} & z_{ij}^c \end{bmatrix} I_{ij}^{3\phi} \quad \forall (i, j) \in \mathcal{E}. \quad (5.16)$$

Since v_0^{est} , i.e. head node voltage is known, the voltage of other nodes of a radial grid can be found using (5.16).

6. *Per-phase voltage difference* : Using (5.16), the difference in per-phase voltage can be found as,

$$\Delta V_i = |V_i^{\text{est}}| - |V_i^{\text{per}}| \quad \forall i \in \mathcal{V}. \quad (5.17)$$

7. *Updating voltage bounds*: the voltage bounds are updated for $\mathbf{P}_{\text{CIA}}^{\phi,+}$ to reflect the cumulative path voltage difference that arises due to per-phase optimization neglecting mutual impedances. The update is as follows:

$$\begin{aligned} \bar{V} &\leftarrow \bar{V} + \alpha \Delta V_i \\ \underline{V} &\leftarrow \underline{V} - \alpha \Delta V_i. \end{aligned} \quad (5.18)$$

where α is a design parameter that can be set less than 1 to allow smaller steps in each iteration.

8. *Iterate*: Go to **Step 1**.

The next section outlines a simplistic simulation-based approach to find the HC, called the Random Search method.

5.4 RANDOM SEARCH METHOD

In the Random Search method, the DER power in different nodes is increased incrementally until grid constraints are violated. The primary purpose of this naive approach is to serve as a baseline for comparison with more sophisticated methods proposed in this dissertation.

- Start with the feeder's nominal loading.
- Randomly choose a set of nodes in the feeder and add 1 kW DERs.
- The voltages and currents are evaluated using the Backward/Forward sweep method.
- The method continues its random adjustments to the loads in each iteration until a configuration is found where at least one of the grid constraints is violated.

Next section, numerical results are presented to validate the proposed methodology.

5.5 NUMERICAL RESULTS

In this section, simulation results on the IEEE 37-node test system are presented together with a realistic 534-node radial distribution system from Vermont. IEEE

37-node test system is a three-phase, unbalanced medium voltage (4.8 kV) network with a total load of 2.45 MW. The realistic feeder is a 7.2 kV radial network including 534 nodes, 533 lines, and 160 loads with a total load of 2.47 MW. The MATLAB code provided by [82] is used for three-phase simulations. Using the proposed approach enables an increase in the amount of HC without causing any additional violations. Fig. 5.17 shows the voltage bounds upon the termination of the proposed iterative method. It can be seen that all of the three-phase voltages are within \underline{V}, \bar{V} . It can also be seen that the actual voltages, i.e., the green markers, get very close to the voltage bounds. This shows that, the voltage margin in Method 2ii, comes from neglecting mutual impedances.

For the IEEE 37-node system, the results of p_i^- and p_i^+ obtained from three different methods—Method 2ii, Mod-Z(0.001), and the iterative HC approach—are displayed in Fig. 5.18. Table 5.3 compares the simulation time and total HC for Method 2ii, Mod-Z(0.001), the iterative method, and random search method across two networks. For the random search method, run Time is the sum of simulation time for 100 runs, while HC is the worst HC obtained across 100 runs. It is worth noting that in the iterative method, \underline{HC} and \overline{HC} consistently show improvements when utilizing the iterative method. This enhancement is achieved by leveraging information regarding the mutual impedance of the grid. This increase in hosting capacity does not lead to any voltage violations, therefore no line modification is required in $\mathbf{P}_{CIA}^{\phi,+}$. That is, Mod-Z is not used with the iterative method. The Random Search method generally yields a lower HC across various scenarios, with the notable exception of the \overline{HC} for the 534-node feeder. This deviation can be attributed to the fact that in this particular case, HC is limited by the transformer’s rating rather than voltage

limits. Given that the power drawn from the incoming transformer does not depend on the location of the DERs, the Random Search method surpasses the performance of other techniques in this scenario.

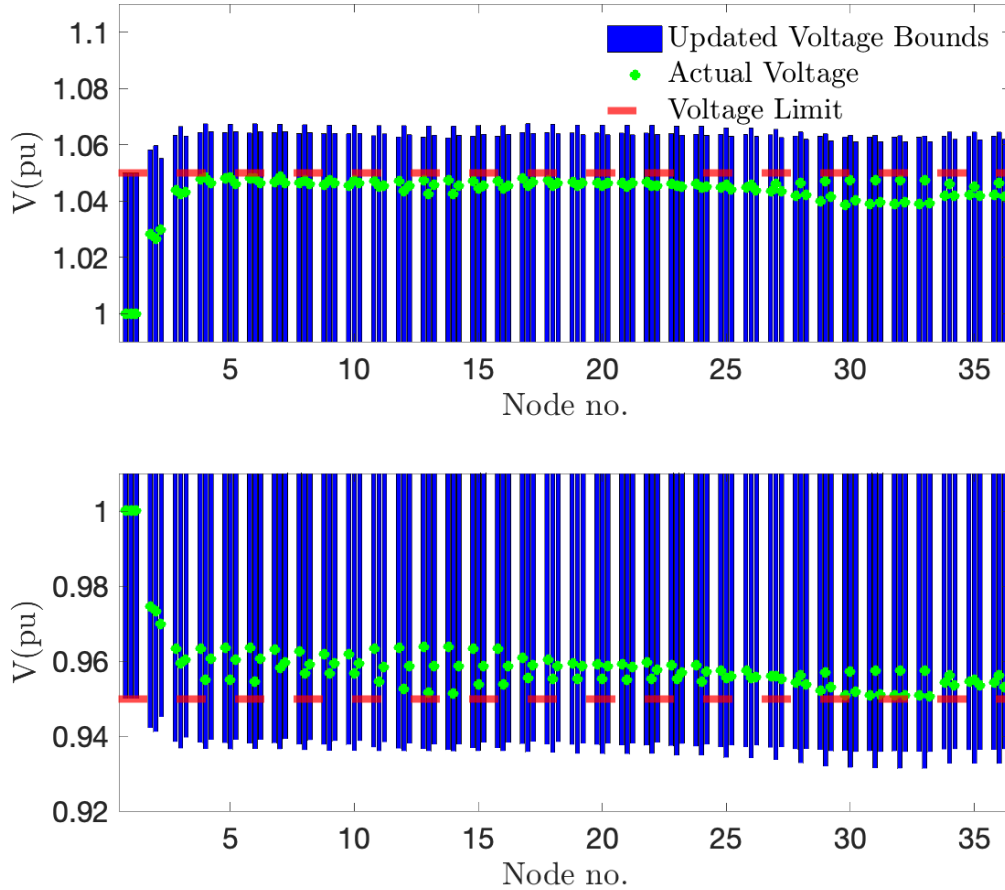


Figure 5.17: Voltage bounds upon termination of the iterative method.

Figs. 5.19 and 5.20 present $|V^{3\phi}|$ for different methods applied to the 534-node network for $\mathbf{P}_{CIA}^{\phi,-}$ and $\mathbf{P}_{CIA}^{\phi,+}$. It can be seen that using the proposed iterative and Mod-Z methods, the voltage margin is smaller, which allows for higher HC as evident in Table 5.3. In Figure 5.20, the voltages cannot approach the limits due to transformer

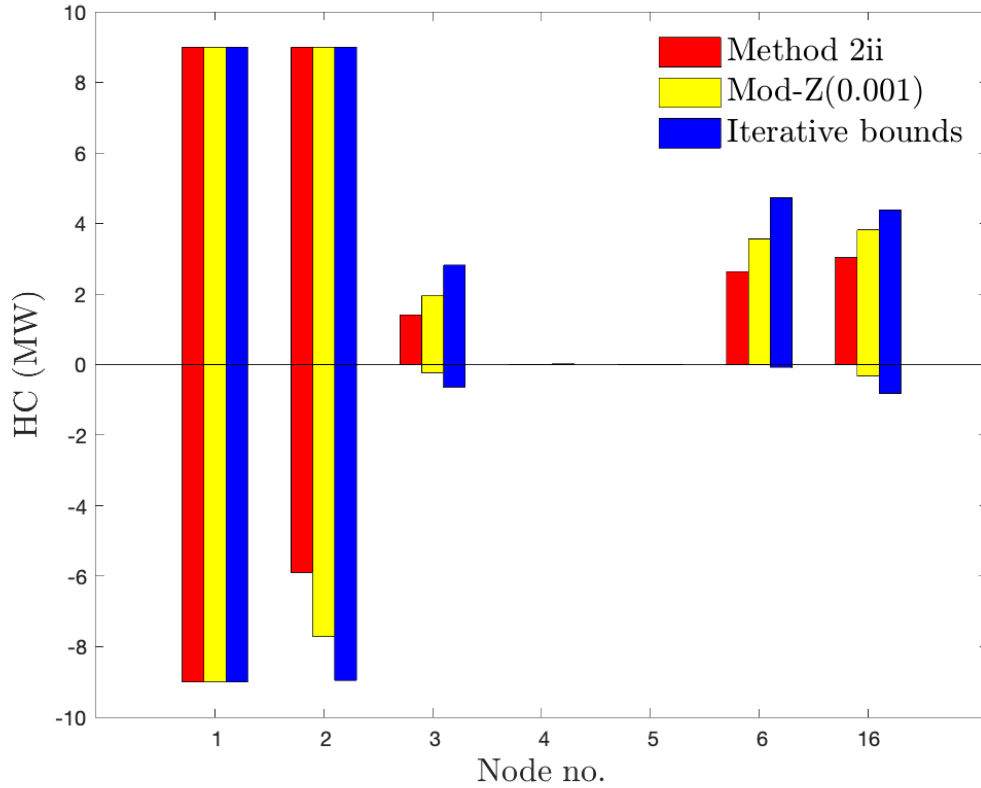


Figure 5.18: Comparing the hosting capacity from the iterative approach to that of Method 2ii and Mod-Z.

Table 5.3: Comparing the different methods across two networks.

Method	IEEE 37 Node			534-node Feeder		
	HC (MW)	HC (MW)	Run Time (sec)	HC (MW)	HC (MW)	Run Time (sec)
Method 2ii	-14.9	25.1	62	-26.4	46.5	380
Iterative HC	-19.5	30.4	314	-59.4	73.0	2973
Mod-Z(0.001)	-17.3	27.4	60	-74.3	71.8	439
Random Search	-5.9	12.2	343	-32.9	76.5	2346

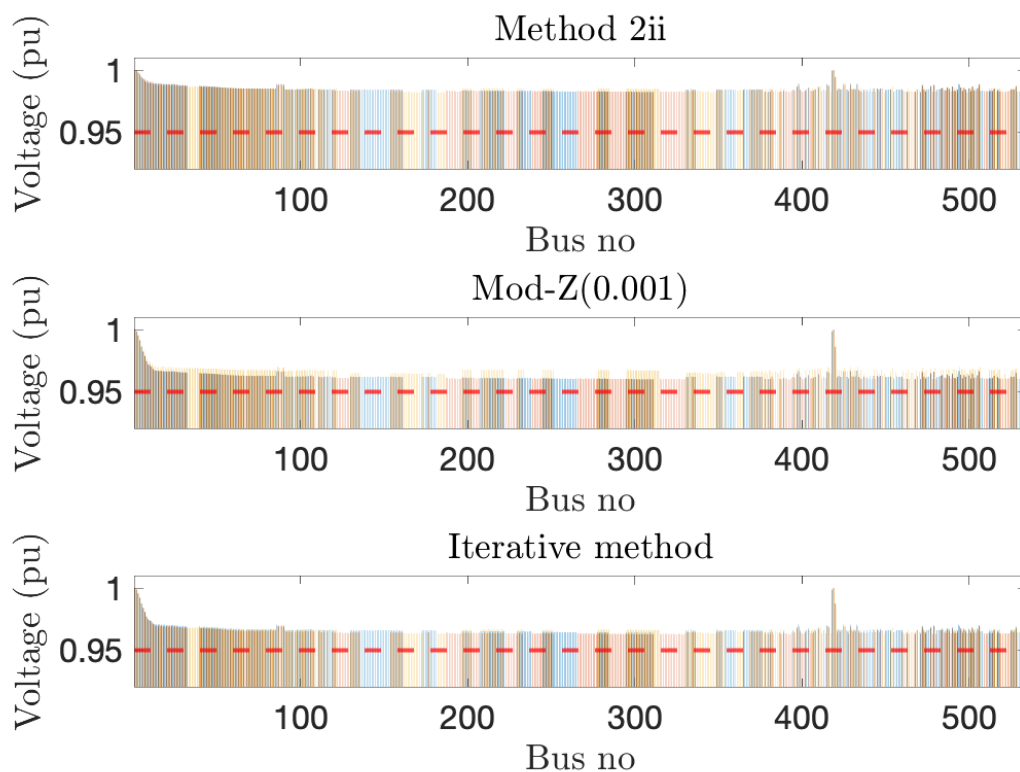


Figure 5.19: Voltage profiles for a 534-node feeder are depicted in the figures below for $\mathbf{P}_{CIA}^{\phi,-}$. In these figures, blue, red, and yellow correspond to phases *a*, *b*, and *c*, respectively.

rating constraints.

It is important to note that the optimization problem may result in very small HC values in some nodes while leading to significantly higher HC values in a few nodes within the system. This discrepancy can raise concerns regarding fairness since only certain consumers will be permitted to install DERs. We consider two sets of w_i , in the objective function and evaluate the HC for a realistic 534-node network under two scenarios: 1) Weight values (w_i) are equal for all nodes. 2) Weight values for leaf nodes are doubled compared to other nodes. Modifying the w_i coefficients enables

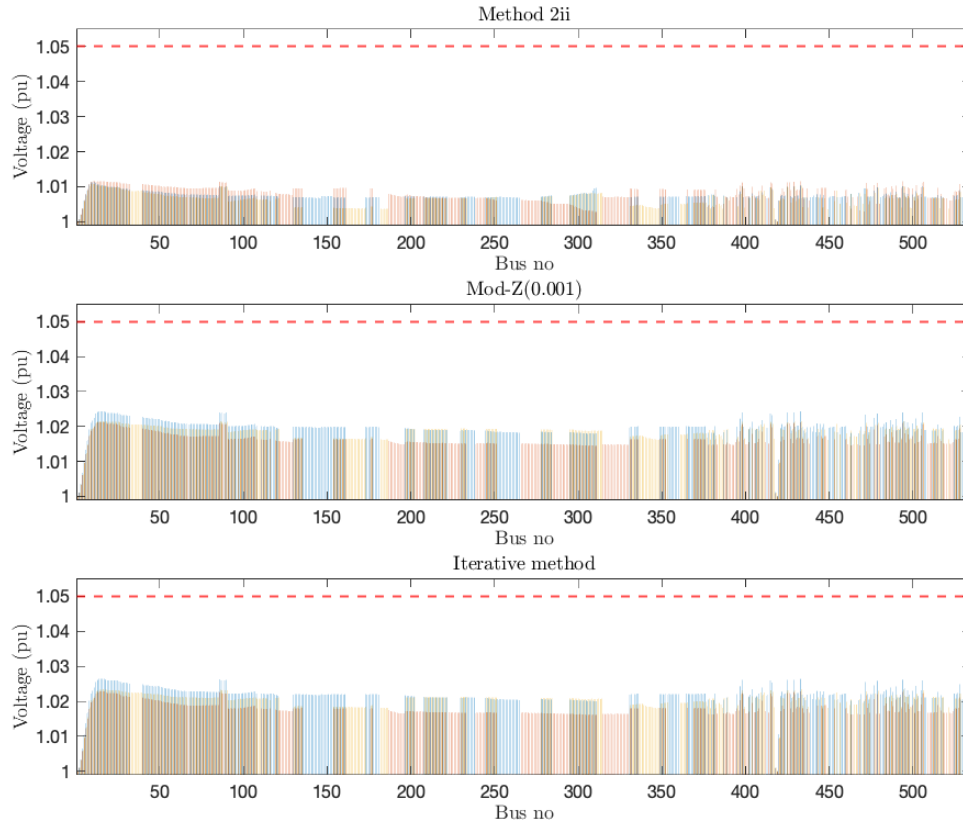


Figure 5.20: Voltage profiles for a 534-node feeder are depicted in the figures below for $\mathbf{P}_{CIA}^{\phi,+}$. In these figures, blue, red, and yellow correspond to phases *a*, *b*, and *c*, respectively.

us to expand the locations where DERs can be installed. Specifically, the locations with HC larger than 0.5 MW have increased from 8 to 16. However, this adjustment comes at the cost of reduced $\overline{\text{HC}}$, which decreases from 73.0 MW to 71.0 MW and reduced $\underline{\text{HC}}$, which decreases from 59.4 MW to 53.0 MW.

Future research efforts could delve into exploring the trade-off between fairness in DER allocation and its impact on the overall HC of the grid.

5.6 CONCLUSION

This section has introduced a comprehensive approach to obtaining the DER HC in a three-phase distribution feeder. Leveraging CIA of the AC power flow, our methodology establishes bounds on positive and negative DER injections at each node. A rigorous analysis is developed to ascertain the conditions under which this per-phase approach can guarantee compliance with three-phase constraints. Furthermore, we have presented an iterative approach to enhance HC by adjusting per-phase voltage bounds. A simulation-based analysis using both the IEEE 37-node test feeder and a real 534-node unbalanced radial distribution feeder is performed and results demonstrate that the proposed iterative method increases the feeder HC. Potential future research encompasses the extension of the proposed method to analyze comprehensive 3-phase networks, as well as comparing its conservativeness to the method presented in this section. Additionally, extending the HC analysis methods to meshed distribution and sub-transmission networks will be explored in future work.

BIBLIOGRAPHY

- [1] Junjie HU, Guangya YANG, Koen KOK, Yusheng XUE, and Henrik W. BINDNER. Transactive control: a framework for operating power systems characterized by high penetration of distributed energy resources. *Journal of Modern Power Systems and Clean Energy*, 5:451–464, 2017.
- [2] Sarnaduti Brahma, Adil Khurram, Hamid Ossareh, and Mads Almassalkhi. Optimal frequency regulation using packetized energy management. *IEEE Transactions on Smart Grid*, pages 1–1, 2022.
- [3] Hani Mavalizadeh, Luis A. Duffaut Espinosa, and Mads R. Almassalkhi. Decentralized frequency control using packet-based energy coordination. In *2020 IEEE International Conference on Communications, Control, and Computing Technologies for Smart Grids (SmartGridComm)*, pages 1–7, 2020.
- [4] Fabio Moret and Pierre Pinson. Energy collectives: A community and fairness based approach to future electricity markets. *IEEE Transactions on Power Systems*, 34(5):3994–4004, 2019.
- [5] Madi Zholbaryssov, Christoforos N. Hadjicostis, and Alejandro D. Dominguez-Garcia. Privacy-preserving distributed coordination of distributed energy resources. In *2020 59th IEEE Conference on Decision and Control (CDC)*, pages 4689–4696, 2020.
- [6] Junjian Qi, Youngjin Kim, Chen Chen, Xiaonan Lu, and Jianhui Wang. Demand response and smart buildings: A survey of control, communication, and cyber-physical security. *ACM Trans. Cyber-Phys. Syst.*, 1(4), oct 2017.
- [7] Daniel Sloot, Nico Lehmann, and Armin Ardone. Explaining and promoting participation in demand response programs: The role of rational and moral motivations among german energy consumers. *Energy Research & Social Science*, 84:102431, 2022.

- [8] Mushfiqur R. Sarker, Miguel A. Ortega-Vazquez, and Daniel S. Kirschen. Optimal coordination and scheduling of demand response via monetary incentives. *IEEE Transactions on Smart Grid*, 6(3):1341–1352, 2015.
- [9] Flora Charbonnier, Thomas Morstyn, and Malcolm D. McCulloch. Coordination of resources at the edge of the electricity grid: Systematic review and taxonomy. *Applied Energy*, 318:119188, 2022.
- [10] Austin R. Coffman, Neil Cammardella, Prabir Barooah, and Sean Meyn. Aggregate flexibility capacity of tcls with cycling constraints. *IEEE Transactions on Power Systems*, 38(1):52–62, 2023.
- [11] Justin T. Hughes, Alejandro D. Domínguez-García, and Kameshwar Poolla. Identification of virtual battery models for flexible loads. *IEEE Transactions on Power Systems*, 31(6):4660–4669, 2016.
- [12] Johanna L. Mathieu, Maryam Kamgarpour, John Lygeros, Göran Andersson, and Duncan S. Callaway. Arbitraging intraday wholesale energy market prices with aggregations of thermostatic loads. *IEEE Transactions on Power Systems*, 30(2):763–772, 2015.
- [13] Johanna L Mathieu, Maryam Kamgarpour, John Lygeros, and Duncan S Callaway. Energy arbitrage with thermostatically controlled loads. In *European Conference on Circuit Theory and Design*, pages 2519–2526. IEEE, Jul 2013.
- [14] He Hao, Borhan M. Sanandaji, Kameshwar Poolla, and Tyrone L. Vincent. Aggregate flexibility of thermostatically controlled loads. *IEEE Transactions on Power Systems*, 30(1):189–198, 2015.
- [15] Sai Pushpak Nandanoori, Indrasis Chakraborty, Thiagarajan Ramachandran, and Soumya Kundu. Identification and validation of virtual battery model for heterogeneous devices, 2019.
- [16] Luis A. Duffaut Espinosa, Adil Khurram, and Mads R. Almassalkhi. A virtual battery model for packetized energy management. In *2020 59th IEEE Conference on Decision and Control (CDC)*, pages 42–48, 2020.
- [17] Francois Chollet. *Deep learning with Python*. Simon and Schuster, 2021.
- [18] Indrasis Chakraborty, Sai Pushpak Nandanoori, and Soumya Kundu. Virtual battery parameter identification using transfer learning based stacked autoencoder, 2018.

- [19] Indrasis Chakraborty, Sai Pushpak Nandanoori, Soumya Kundu, and Karanjit Kalsi. Stochastic virtual battery modeling of uncertain electrical loads using variational autoencoder. In *2020 American Control Conference (ACC)*, pages 1305–1310, 2020.
- [20] Inertia: Basic concepts and impacts on the ERCOT grid. Technical report, Electric Reliability Council of Texas, 2018.
- [21] Joshua W. Busby, Kyri Baker, Morgan D. Bazilian, Alex Q. Gilbert, Emily Grubert, Varun Rai, Joshua D. Rhodes, Sarang Shidore, Caitlin A. Smith, and Michael E. Webber. Cascading risks: Understanding the 2021 winter blackout in Texas. *Energy Research & Social Science*, 77:102106, 2021.
- [22] Shengqi Zhang, Heyu Liu, Fei Wang, Tao Yan, and Kaifeng Wang. Secondary frequency control strategy for BESS considering their degree of participation. *Energy Reports*, 6:594–602, 2020. 2020 The 7th International Conference on Power and Energy Systems Engineering.
- [23] Linqi Guo, Changhong Zhao, and Steven H. Low. Graph laplacian spectrum and primary frequency regulation. In *2018 IEEE Conference on Decision and Control (CDC)*, pages 158–165, 2018.
- [24] Bala Kameshwar Poolla, Dominic Groß, and Florian Dörfler. Placement and implementation of grid-forming and grid-following virtual inertia and fast frequency response. *IEEE Transactions on Power Systems*, 34(4):3035–3046, 2019.
- [25] F. C. Schweppe, R. D. Tabors, J. L. Kirtley, H. R. Outhred, F. H. Pickel, and A. J. Cox. Homeostatic utility control. *IEEE Transactions on Power Apparatus and Systems*, PAS-99(3):1151–1163, 1980.
- [26] Martin Brokish. Adaptive load control of microgrids with non-dispatchable generation. Master’s thesis, Massachusetts Institute of Technology, <https://dspace.mit.edu/handle/1721.1/53205>, 2009.
- [27] H. Zhao, Q. Wu, S. Huang, H. Zhang, Y. Liu, and Y. Xue. Hierarchical control of thermostatically controlled loads for primary frequency support. *IEEE Transactions on Smart Grid*, 9(4):2986–2998, 2018.
- [28] W. Mendieta and C. A. Cañizares. Primary frequency control in isolated microgrids using thermostatically controllable loads. *IEEE Transactions on Smart Grid*, 12(1):93–105, 2021.

- [29] T. Clarke, T. Slay, C. Eustis, and R. B. Bass. Aggregation of residential water heaters for peak shifting and frequency response services. *IEEE Open Access Journal of Power and Energy*, 7:22–30, 2020.
- [30] Austin R. Coffman, Neil Cammardella, Prabir Barooah, and Sean Meyn. Flexibility capacity of thermostatically controlled loads with cycling/lock-out constraints. In *2020 American Control Conference (ACC)*, pages 527–532, 2020.
- [31] M. H. Syed, E. Guillo-Sansano, S. M. Blair, A. J. Roscoe, and G. M. Burt. A novel decentralized responsabilizing primary frequency control. *IEEE Transactions on Power Systems*, 33(3):3199–3201, 2018.
- [32] E. Weitenberg, Y. Jiang, C. Zhao, E. Mallada, C. De Persis, and F. Dörfler. Robust decentralized secondary frequency control in power systems: Merits and tradeoffs. *IEEE Transactions on Automatic Control*, 64(10):3967–3982, 2019.
- [33] C. Jin, W. Li, J. Shen, P. Li, L. Liu, and K. Wen. Active frequency response based on model predictive control for bulk power system. *IEEE Transactions on Power Systems*, 34(4):3002–3013, 2019.
- [34] Mads Almassalkhi, Sarnaduti Brahma, Nawaf Nazir, Hamid Ossareh, Pavan Racherla, Soumya Kundu, Sai Pushpak Nandanoori, Thiagarajan Ramachandran, Ankit Singhal, Dennice Gayme, Chengda Ji, Enrique Mallada, Yue Shen, Pengcheng You, and Dhananjay Anand. Hierarchical, grid-aware, and economically optimal coordination of distributed energy resources in realistic distribution systems. *Energies*, 13(23), 2020.
- [35] Konrad Schmitt, Rabindra Bhatta, Manohar Chamana, Mahtab Murshed, Ilham Osman, Stephen Bayne, and Luciane Canha. A review on active customers participation in smart grids. *Journal of Modern Power Systems and Clean Energy*, 11(1):3–16, 2023.
- [36] AusNet Services. . export limits for embedded generators up to 200 kva connected at low voltage, 2017.
- [37] Michael Z. Liu, Luis F. Ochoa, Peter K. C. Wong, and John Theunissen. Using opf-based operating envelopes to facilitate residential der services. *IEEE Transactions on Smart Grid*, 13(6):4494–4504, 2022.
- [38] Xin Chen, Emiliano Dall’Anese, Changhong Zhao, and Na Li. Aggregate power flexibility in unbalanced distribution systems. *IEEE Transactions on Smart Grid*, 11(1):258–269, 2020.

- [39] Emiliano Dall’Anese, Swaroop S. Guggilam, Andrea Simonetto, Yu Christine Chen, and Sairaj V. Dhople. Optimal regulation of virtual power plants. *IEEE Transactions on Power Systems*, 33(2):1868–1881, 2018.
- [40] Zhao Yuan and Mohammad Reza Hesamzadeh. A distributed economic dispatch mechanism to implement distribution locational marginal pricing. In *2018 Power Systems Computation Conference (PSCC)*, pages 1–7, 2018.
- [41] Stephanie Ross and Johanna Mathieu. Strategies for network-safe load control with a third-party aggregator and a distribution operator. *IEEE Transactions on Power Systems*, 36(4):3329–3339, 2021.
- [42] Nawaf Nazir and Mads Almassalkhi. Voltage positioning using co-optimization of controllable grid assets in radial networks. *IEEE Transactions on Power Systems*, 36(4):2761–2770, 2021.
- [43] Nawaf Nzir and Mads Almassalkhi. Grid-aware aggregation and realtime disaggregation of distributed energy resources in radial networks. *IEEE Transactions on Power Systems*, 37(3):1706–1717, 2022.
- [44] Dongchan Lee, Konstantin Turitsyn, Daniel K. Molzahn, and Line A. Roald. Feasible path identification in optimal power flow with sequential convex restriction. *IEEE Transactions on Power Systems*, 35(5):3648–3659, 2020.
- [45] Dongchan Lee, Konstantin Turitsyn, Daniel K. Molzahn, and Line Roald. Robust AC optimal power flow with robust convex restriction. *IEEE Transactions on Power Systems*, 36(6):4953–4966, 2021.
- [46] V. Bassi, D. Jaglal, L. Ochoa, T. Alpcan, and C. Leckie. Deliverables 1-2-3a model-free voltage calculations and operating envelopes. Technical report, University of Melbourne, 7 2022.
- [47] Kyriacos Petrou, Andreas T. Procopiou, Luis Gutierrez-Lagos, Michael Z. Liu, Luis F. Ochoa, Tom Langstaff, and John M. Theunissen. Ensuring distribution network integrity using dynamic operating limits for prosumers. *IEEE Transactions on Smart Grid*, 12(5):3877–3888, 2021.
- [48] Valentín Rigoni, Damian Flynn, and Andrew Keane. Coordinating demand response aggregation with lv network operational constraints. *IEEE Transactions on Power Systems*, 36(2):979–990, 2021.
- [49] P. Kundur. *Power Systems Stability and Control*. CRC Press New York, NY, USA, 1994.

- [50] B J Kirby. Frequency control concerns in the north american electric power system. Technical report, U.S. Department of Energy, Office of Scientific and Technical Information, 2003.
- [51] Mads Almassalkhi, Luis Duffaut Espinosa, Paul D. H. Hines, Jeff Frolik, Sumit Paudyal, and Mahraz Amini. *Asynchronous Coordination of Distributed Energy Resources with Packetized Energy Management*, pages 333–361. Springer New York, New York, NY, 2018.
- [52] L. A. Duffaut Espinosa and M. Almassalkhi. A packetized energy management macromodel with quality of service guarantees for demand-side resources. *IEEE Transactions on Power Systems*, pages 1–1, 2020.
- [53] Mads Almassalkhi, Jeff Frolik, and Paul Hines. Packetizing the power grid: The rules of the internet can also balance electricity supply and demand. *IEEE Spectrum*, 59(2):42–47, 2022.
- [54] H. Mavalizadeh, L. A. Duffaut Espinosa, and M. R. Almassalkhi. Decentralized frequency control using packet-based energy coordination. In *2020 IEEE International Conference on Communications, Control, and Computing Technologies for Smart Grids (SmartGridComm)*, pages 1–7, 2020.
- [55] Sai Pushpak Nandanoori, Soumya Kundu, Draguna Vrabić, Karan Kalsi, and Jianming Lian. Prioritized threshold allocation for distributed frequency response. In *2018 IEEE Conference on Control Technology and Applications (CCTA)*, pages 237–244, 2018.
- [56] M.E. Baran and F.F. Wu. Optimal capacitor placement on radial distribution systems. *IEEE Transactions on Power Delivery*, 4(1):725–734, January 1989.
- [57] Rahmat Heidari, Maria M. Seron, and Julio H. Braslavsky. Non-local approximation of power flow equations with guaranteed error bounds. In *2017 Australian and New Zealand Control Conference (ANZCC)*, pages 83–88, 2017.
- [58] Luis A. Duffaut Espinosa, Mads Almassalkhi, Paul Hines, and Jeff Frolik. System properties of packetized energy management for aggregated diverse resources. *Power Systems Computation Conference*, June 2018.
- [59] Luis A. Duffaut Espinosa, Adil Khurram, and Mads Almassalkhi. A virtual battery model for packetized energy management. In *59th IEEE Conference on Decision and Control (CDC)*, pages 42–48, December 2020.

- [60] L. A. Duffaut Espinosa, Adil Khurram, and Mads Almassalkhi. Reference-tracking control policies for packetized coordination of heterogeneous DER populations. *IEEE Transactions on Control Systems Technology*, 29(6):2427–2443, 2021.
- [61] M. Mirosevic and Z. Maljkovic. Effect of sudden change load on isolated electrical grid. In *2015 International Conference on Electrical Systems for Aircraft, Railway, Ship Propulsion and Road Vehicles (ESARS)*, pages 1–4, 2015.
- [62] Fast frequency response in the nem. Technical report, Austrian Energy Market Operator, <https://www.aemo.com.au>, 03 2017.
- [63] L. A. Duffaut Espinosa, M. Almassalkhi, P. Hines, and J. Frolik. System properties of packetized energy management for aggregated diverse resources. In *2018 Power Systems Computation Conference (PSCC)*, pages 1–7, 2018.
- [64] Goran Andersson. Dynamics and control of electric power systems. Technical report, ETH Zurich, 2012.
- [65] S. P. Nandanoori, S. Kundu, D. Vrabie, K. Kalsi, and J. Lian. Prioritized threshold allocation for distributed frequency response. In *2018 IEEE Conference on Control Technology and Applications (CCTA)*, pages 237–244, 2018.
- [66] North American Reliability Control Corporation. Essential reliability services task force measures framework report, 2015.
- [67] L. A. Duffaut Espinosa, Adil Khurram, and Mads Almassalkhi. Reference-tracking control policies for packetized coordination of heterogeneous DER populations. *IEEE Transactions on Control Systems Technology*, 29(6):2427–2443, 2020.
- [68] S. Brahma, H. Ossareh, and M. Almassalkhi. Statistical modeling and forecasting of automatic generation control signals. In *IREP Bulk Power System Dynamics and Control Symposium*, 2022.
- [69] R Haffen, K Subbaro, V Viswanathan, and M Kintner-Meyer. Requirements for defining utility drive cycles: An exploratory analysis of grid frequency regulation data for establishing battery performance testing standards. Technical report, University of Melbourne, 2011.
- [70] Stellato Bartolomeo. Data-driven chance constrained optimization. Master’s thesis, ETH-Zürich, <https://www.research-collection.ethz.ch/handle/20.500.11850/154768>, 2017.

- [71] B Stellato. Data-driven chance constrained optimization. Master’s thesis, Autom. Control Lab., ETH-Zurich, 2014.
- [72] Adil Khurram, Luis A. Duffaut Espinosa, and Mads R. Almassalkhi. A methodology for quantifying flexibility in a fleet of diverse DERs. In *2021 IEEE Madrid PowerTech*, pages 1–6, 2021.
- [73] A. Moeini, I. Kamwa, P. Brunelle, and G. Sybille. Open data IEEE test systems implemented in simpowersystems for education and research in power grid dynamics and control. In *2015 50th International Universities Power Engineering Conference (UPEC)*, pages 1–6, 2015.
- [74] Arnab Bhattacharya, Jacob Hansen, Karan Kalsi, Jianming Lian, Sai Pushpak Nandanoori, Hayden Reeve, Veronica Adetola, F Lin, T Leichtman, Sri Nikhil Gourisetti, William Hofer, Soumya Kundu, Laurentiu Marinovici, Shwetha Niddodi, Draguna Vrabie, M Chiodo, S Yuan, and D Wright. Incentive-based control and coordination of distributed energy resources. Technical Report DOE-PNNL-28724, PNNL, 05 2019.
- [75] Sai Pushpak Nandanoori, Indrasis Chakraborty, Thiagarajan Ramachandran, and Soumya Kundu. Identification and validation of virtual battery model for heterogeneous devices. In *2019 IEEE Power & Energy Society General Meeting (PESGM)*, pages 1–5, 2019.
- [76] Adil Khurram, Mahraz Amini, Luis A. Duffaut Espinosa, Paul D. H. Hines, and Mads R. Almassalkhi. Real-time grid and der co-simulation platform for testing large-scale der coordination schemes. *IEEE Transactions on Smart Grid*, 13(6):4367–4378, 2022.
- [77] Oluwagbemileke Oyefeso, Gregory Ledva, Mads Almassalkhi, Ian Hiskens, and Johanna Mathieu. Control of aggregate air-conditioning load using packetized energy concepts. In *2022 IEEE Conference on Control Technology and Applications (CCTA)*, 2022.
- [78] S. Lloyd. Least squares quantization in pcm. *IEEE Transactions on Information Theory*, 28(2):129–137, 1982.
- [79] C.L. Hwang and K. Yoon. *Multiple Attribute Decision Making: Methods and Applications*. Springer-Verlag, 1981.
- [80] Nawaf Nazir and Mads Almassalkhi. Convex inner approximation of the feeder hosting capacity limits on dispatchable demand. In *2019 IEEE 58th Conference on Decision and Control (CDC)*, pages 4858–4864, 2019.

- [81] K. P. Schneider, B. A. Mather, B. C. Pal, C.-W. Ten, G. J. Shirek, H. Zhu, J. C. Fuller, J. L. R. Pereira, L. F. Ochoa, L. R. de Araujo, R. C. Dugan, S. Matthias, S. Paudyal, T. E. McDermott, and W. Kersting. Analytic Considerations and Design Basis for the IEEE Distribution Test Feeders. *IEEE Transactions on Power Systems*, 33(3):3181–3188, 2018.
- [82] Alejandro Garces. Linear load flow in power distribution systems: Unbalanced case. Online, 2023. Retrieved September 23, 2023.

APPENDIX

A. DERIVATION OF CURRENT PROXY BOUNDS l^- AND l^+

The goal of this appendix is to clarify the structure of the affine $f_{\text{aff}}(\cdot)$ and quadratic $f_{\text{quad}}(\cdot)$ functions that underpin bounds l^-, l^+ used in (2.18). To derive the lower and upper bounds of l , we consider the second-order Taylor-series approximation of (2.17) about an appropriate nominal operating point, $x_{ij}^0 := \text{col}\{P_{ij}^0, Q_{ij}^0, v_j^0\} \in \mathbb{R}^3$. This yields an approximation that is accurate across a range of operating conditions [43]:

$$l_{ij}(P_{ij}, Q_{ij}, V_i) \approx l_{ij}^0(x_{ij}^0) + J_{ij}^\top \delta_{ij} + \frac{1}{2} \delta_{ij}^\top H_{e,ij} \delta_{ij}, \quad (6.1)$$

where $\delta_{ij} := [P_{ij} - P_{ij}^0, Q_{ij} - Q_{ij}^0, v_j - v_j^0]$, the Jacobian, J_{ij} , and Hessian, $H_{e,ij}$, are defined as

$$J_{ij} := \begin{bmatrix} \frac{2P_{ij}^0}{v_i^0} & \frac{2Q_{ij}^0}{v_i^0} & -\frac{(P_{ij}^0)^2 + (Q_{ij}^0)^2}{(v_i^0)^2} \end{bmatrix}, \quad (6.2)$$

$$H_{e,ij} := \begin{bmatrix} \frac{2}{v_i^0} & 0 & \frac{-2P_{ij}^0}{(v_i^0)^2} \\ 0 & \frac{2}{v_i^0} & \frac{-2Q_{ij}^0}{(v_i^0)^2} \\ \frac{-2P_{ij}^0}{(v_i^0)^2} & \frac{-2Q_{ij}^0}{(v_i^0)^2} & 2\frac{(P_{ij}^0)^2 + (Q_{ij}^0)^2}{(v_i^0)^3} \end{bmatrix}. \quad (6.3)$$

From (6.1), the square of current magnitude is always positive, so:

$$l_{ij} = |l_{ij}| \approx \left| l_{ij}^0 + J_{ij}^\top \delta_{ij} + \frac{1}{2} \delta_{ij}^\top H_{e,ij} \delta_{ij} \right|. \quad (6.4)$$

Applying the triangle inequality and the fact that Hessian in (6.3) is positive

semi-definite (PSD) [42], we have

$$l_{ij} \leq l_{ij}^0 + \left| J_{ij}^\top \delta_{ij} \right| + \frac{1}{2} \delta_{ij}^\top H_{e,ij} \delta_{ij}. \quad (6.5)$$

Applying the properties of the maximum operator, we get the quadratic function:

$$l_{ij} \leq l_{ij}^0 + \max \left\{ 2 \left| J_{ij}^\top \delta_{ij} \right|, \delta_{ij}^\top H_{e,ij} \delta_{ij} \right\}. \quad (6.6)$$

Note that the RHS of (6.6) is quadratic in terms of the three physical variables (P_{ij}, Q_{ij}, V_i) that embody δ_{ij} . To characterize the upper bound in terms of the proxy variables requires considering worst-case combinations of upper (+) and lower (-) proxy variables, i.e., over all eight combinations: $\delta_{ij}^+ := \delta_{ij}(P_{ij}^+, Q_{ij}^+, V_i^+)$, $\delta_{ij}^-(P_{ij}^+, Q_{ij}^+, V_i^-)$, \dots , $\delta_{ij}^-(P_{ij}^-, Q_{ij}^-, V_i^+)$, and $\delta_{ij}^- := \delta_{ij}(P_{ij}^-, Q_{ij}^-, V_i^-)$. Thus, we get:

$$f_{\text{quad}}(\cdot) := l_{ij}^0 + \max \left\{ 2 \left| J_{ij,+}^\top \delta_{ij}^+ + J_{ij,-}^\top \delta_{ij}^- \right|, \psi_{ij} \right\}, \quad (6.7)$$

where $J_{ij,+}$ and $J_{ij,-}$ are composed of the positive and negative entries of J_{ij} , respectively, and $J_{ij} = J_{ij,+} + J_{ij,-}$. Further, $\psi_{ij} := \max\{\delta_{ij}^{+/-} H_{e,ij} \delta_{ij}^{+/-}\}$ is the largest product among the eight proxy pairs. Clearly, relaxing $f_{\text{quad}}(\cdot)$ provides a convex upper bound on l_{ij} as utilized in (2.18).

For the lower bound, consider (6.1) and drop the term with PSD $H_{e,ij}$, which gives

$$l_{ij} \geq l_{ij}^0 + J_{ij}^\top \delta_{ij} := L_{ij}. \quad (6.8)$$

Thus, in terms of proxy variables, we get

$$f_{\text{aff}}(\cdot) := l_{ij}^0 + J_{ij,+}^\top \delta_{ij}^- + J_{ij,-}^\top \delta_{ij}^+. \quad (6.9)$$

This completes the derivations. For full details on these bounds and the CIA-based methods and results (for balanced feeders), please see [42, 43].

B. PROOF OF THEOREM 4

From Assumption 5, the impedance matrix has identical mutual impedances z_{ij}^m , which together with (2.6), means that $\Delta V_{ij}^{3\phi}$ can be expressed as,

$$\Delta V_{ij}^{3\phi} = \begin{bmatrix} z_{ij}^a I_{ij}^a + z_{ij}^m (I_{ij}^b + I_{ij}^c) \\ z_{ij}^b I_{ij}^b + z_{ij}^m (I_{ij}^a + I_{ij}^c) \\ z_{ij}^c I_{ij}^c + z_{ij}^m (I_{ij}^a + I_{ij}^b) \end{bmatrix}. \quad (6.10)$$

Now, under Assumption 4, $I_{ij}^a + I_{ij}^b + I_{ij}^c = 0$, which decouples the phases as

$$\Delta V_{ij}^{3\phi} = \begin{bmatrix} z_{ij}^a - z_{ij}^m & 0 & 0 \\ 0 & z_{ij}^b - z_{ij}^m & 0 \\ 0 & 0 & z_{ij}^c - z_{ij}^m \end{bmatrix} I_{ij}^{3\phi}. \quad (6.11)$$

The diagonal structure clearly extends per-phase analyses to the corresponding full 3-phase (unbalanced) feeder. Thus, HC analysis via $\mathbf{P}_{\text{CIA}}^{\phi,+}$ meets 3-phase voltage requirements. This concludes the proof.

VITAE

Hani Mavalizadeh,

Department of Electrical and Biomedical Engineering,
University of Vermont, Vermont, USA, 05405.

EDUCATION

- M.Sc. Electrical Engineering 2013, Iran University of Science and Technology, Tehran, Iran.
- B.Sc. Electrical Engineering 2011, University of Tehran, Tehran, Iran.

PUBLICATIONS

JOURNAL PUBLICATIONS

- **H. Mavalizadeh**, Duffaut Espinosa, L., Almassalkhi, M., “Decentralized Frequency Control using Packet-based Energy Coordination,” *Proceedings of the smart grid conference*, 2020.
- M. Almassalkhi, **H. Mavalizadeh**, L. A. Espinosa, “Decentralized Frequency Control with Packet-Based Energy Management,” *US patent (under review)*.
- M. Matar, **H. Mavalizadeh**, S. Brahma, M. Almassalkhi, S. Wshah, “Learning the state-of-charge of heterogeneous fleets of distributed energy resources with temporal residual networks,” *Journal of Energy Storage*, vol. 70, October 2023.
- **H. Mavalizadeh**, L. A. D. Espinosa and M. R. Almassalkhi, "Improving frequency response with synthetic damping available from fleets of distributed energy resources," in *IEEE Transactions on Power Systems*, Early Access, August 2023.
- **H. Mavalizadeh** and M. R. Almassalkhi, "Methodology for comparing the performance of DER coordination schemes in providing frequency regulation," 2023 IEEE Power & Energy Society General Meeting (PESGM), Orlando, FL, USA, 2023, pp. 1-5.
- **H. Mavalizadeh**, M. Almassalkhi, “Decomposed Phase Analysis using Convex Inner Approximations: a Methodology for DER Hosting Capacity in Distribution Systems,” *Submitted to PSCC2024 conference*.